



universität  
wien

# MASTERARBEIT

Titel der Masterarbeit

Study of Strangeness Production in p-p Collisions at FOPI

Verfasserin

Isepp Katharina, BSc

angestrebter akademischer Grad

Master of Science (MSc)

Wien, 2012

Studienkennzahl lt. Studienblatt:

A 066 876

Studienrichtung lt. Studienblatt:

Masterstudium Physik UG2002

Betreuerin / Betreuer:

Priv.-Doz. Dr. Johann Zmeskal



# Zusammenfassung

Theoretische Berechnungen sowie experimentelle Beobachtungen eines attraktiven Potentials zwischen  $K^-$  Mesonen und Nukleonen haben in den letzten Jahrzehnten zur Vorhersage tiefgebundener kaonischer Zustände geführt, sogenannten kaonischen nuklearen Clustern. Basierend auf der  $\bar{K}N^{I=0}$  Wechselwirkung wird eine starke Komprimierung des Kerns abgeleitet, welche die Bildung von tiefgebundenen Zuständen ermöglichen soll. Die Eigenschaften dieser Zustände stehen unmittelbar in Zusammenhang mit der Stärke des attraktiven Potentials, sodass ihre Untersuchung eine Möglichkeit bieten könnte, um die  $\bar{K}N$  Wechselwirkung zu untersuchen.

Über eine mögliche Entdeckung solcher Cluster wurde in den letzten Jahren von mehreren Kollaborationen berichtet. Vor allem aufgrund zu geringer Statistik war es aber bislang nicht möglich, ihre Existenz zu bestätigen oder zu verneinen. Die FOPI Kollaboration beteiligt sich an dieser Suche mit einem Fixed-Target Experiment, das an der GSI in Darmstadt ausgeführt wurde. Dazu wird die Reaktion  $p + p \rightarrow K^+ + ppK^-$  untersucht, bei welcher gemäß theoretischen Vorhersagen der fundamentale kaonische Cluster  $ppK^-$  gebildet werden soll. Dabei spielt die  $\Lambda(1405)$  Resonanz eine wesentliche Rolle, die gemäß dieser Vorhersagen als gebundener Zustand von  $pK^-$  interpretiert werden kann und so eine Art Basiszustand bildet, welcher durch Bindung eines weiteren Protons in den tiefgebundenen Zustand  $ppK^-$  propagieren kann. Dieser wiederum zerfällt möglicherweise mit einer hohen Wahrscheinlichkeit in ein  $\Lambda$ -Hyperon und ein Proton. Zu diesem Zweck liefert der SIS-18 Beschleuniger an der GSI einen Protonenstrahl mit einer kinetischen Strahlenergie von 3.1 GeV, der auf ein Target, welches aus flüssigem Wasserstoff besteht, gelenkt wird. Die Zerfallsprodukte werden mit dem FOPI Spektrometer gemessen, welches mit einigen Erweiterungen an die Anforderungen des Experimentes angepasst wurde.

Diese Arbeit präsentiert die Rekonstruktion des  $\Lambda$ -Hyperons, welches im Endzustand der Reaktion  $p + p \rightarrow K^+ + [\Lambda + p]$  gebildet werden soll, anhand seines Zerfallskanals in ein  $\pi^-$  Meson und ein Proton. Für die Rekonstruktion des sekundären Vertizes wird die Invariant-Mass-Methode verwendet und es werden verschiedene Modelle diskutiert, um die Form des kombinatorischen Untergrundes zu beschreiben. Darüber hinaus wird eine Studie über in Frage kommender Vertex Cuts durchgeführt, die das rekonstruierte invariante Massenspektrum modifizieren, bevor der verbleibende modellierte Untergrund abgezogen werden kann.



# Abstract

In recent years, theoretical and experimental indications and studies of an attractive potential between  $K^-$  mesons and nucleons have led to the prediction of deeply bound kaonic states, so-called kaonic nuclear clusters. The strong  $\overline{K}N^{I=0}$  interaction has the effect that nuclei are largely compressed such that the formation of deeply bound states seems possible. The characteristics of these states are directly connected to the strength of the attractive potential, therefore the investigation of deeply bound states could offer a possibility to investigate the  $\overline{K}N$  interaction.

So far, there have been several experimental hints that indicate the existence of such bound states, but in particular limited statistics have not allowed to draw clear conclusions on their formation yet. The FOPI collaboration contributes to this search with a fixed target experiment at GSI in Darmstadt, investigating the reaction  $p+p \rightarrow K^+ + ppK^-$  that involves the most fundamental and lightest possible kaonic nuclear cluster  $ppK^-$ . In this reaction the  $\Lambda(1405)$  resonance plays a special role as it can be interpreted as  $pK^-$  bound state that serves as a doorway state to produce deeply bound  $ppK^-$  clusters, which eventually decay with a large branching ratio into a  $\Lambda$ -Hyperon and a proton. For this purpose, the SIS-18 accelerator at GSI delivers a proton beam of 3.1 GeV and the decay products are tracked with the FOPI spectrometer, which has been adjusted to this measurement by applying some modifications to its set-up.

This thesis presents the reconstruction of the  $\Lambda$ -Hyperon, which is involved in the  $p+p \rightarrow K^+ + [\Lambda + p]$  final state, from its decay channel into a  $\pi^-$  meson and a proton. For the secondary vertex reconstruction the invariant mass technique is applied and several methods to model the combinatorial background are discussed. Furthermore a detailed study on possible vertex cut quantities is presented, which reduce the reconstructed invariant mass spectrum before the remaining combinatorial background can be subtracted.



# Contents

<b>1</b>	<b>Introduction</b>	<b>1</b>
1.1	In-Medium Modification of Hadrons . . . . .	3
1.2	Kaonic Nuclear Clusters . . . . .	6
1.2.1	Structure of the $ppK^-$ State . . . . .	8
1.2.2	Kaonic Nuclear Clusters in pp Reactions . . . . .	11
1.2.3	Reaction Kinematics of the pp Collisions . . . . .	13
1.2.4	Experimental Results . . . . .	15
1.2.5	Experimental Approach at GSI . . . . .	18
<b>2</b>	<b>The FOPI Experiment S349 at GSI</b>	<b>21</b>
2.1	Accelerator Facility at GSI . . . . .	23
<b>3</b>	<b>Detector Set-up</b>	<b>25</b>
3.1	Superconducting Solenoid Magnet . . . . .	25
3.2	Drift Chambers . . . . .	25
3.2.1	Central Drift Chamber . . . . .	27
3.2.2	Helitron . . . . .	28
3.3	Time of Flight Detectors . . . . .	29
3.3.1	Plastic Barrel . . . . .	31
3.3.2	Multi-gap Multi-strip Resistive Plate Chambers . . . . .	31
3.3.3	Plastic Wall . . . . .	33
3.3.4	Zero Degree Counter . . . . .	34
3.4	Beam Detectors . . . . .	34
3.4.1	Start Counter . . . . .	35
3.4.2	Beam Profile Monitor . . . . .	36
3.4.3	Veto Detector . . . . .	36
3.5	Target . . . . .	37
3.6	Online Hardware $\Lambda$ Trigger SiAViO . . . . .	37
3.7	FOPI Trigger System . . . . .	38
<b>4</b>	<b>Direct Particle Identification with FOPI</b>	<b>41</b>
4.1	Energy Loss . . . . .	42
4.2	Time of Flight . . . . .	45
<b>5</b>	<b>Data Analysis</b>	<b>48</b>
5.1	Invariant Mass and Missing Mass Technique . . . . .	48
5.2	Tracking and Vertex Reconstruction . . . . .	50
5.2.1	Secondary Vertex Reconstruction of the $\Lambda$ Decay . . . . .	52
5.3	Vertex Cuts . . . . .	56
5.4	Background Models . . . . .	65
5.4.1	Mixed Event Background . . . . .	65

5.4.2	Polynomial Background . . . . .	69
5.5	Inclusive Event Analysis . . . . .	73
<b>6</b>	<b>Outlook</b>	<b>87</b>
6.1	$K^+$ identification and $K^+$ missing mass . . . . .	87
6.2	$\Lambda p$ correlation . . . . .	90
	<b>Bibliography</b>	<b>92</b>
<b>A</b>	<b>Abbreviations</b>	<b>102</b>
A.1	Physical Constants . . . . .	102
A.2	Text Abbreviations . . . . .	102
<b>B</b>	<b>Curriculum Vitae</b>	<b>104</b>
<b>C</b>	<b>Acknowledgements</b>	<b>106</b>



# 1 Introduction

During the past century, scientific research has provided increasingly comprehensive insight into the structure of matter and the development of the universe, thus achieving remarkable progress in the understanding of the fundamental laws and interactions<sup>1</sup> of nature. Modern physics is based upon the concept that these interactions are governed by fundamental symmetries (or invariances), implying the fundamental conservation laws for energy, momentum and angular momentum, respectively, as described by the Noether's theorem.

The progress in technology has enabled the development of sophisticated accelerator facilities, which allow to explore the complex structure of the world at tiny scales, in particular the femtometer<sup>2</sup> scales of atomic nuclei and their constituents. The investigation of the sub-nanometer world of atoms has unfolded the existence of elementary particles and permitted to study their interactions.

The existence of quarks<sup>3</sup> as elementary entities in strong-interaction physics was postulated upon symmetry considerations in 1963 by *M. Gell-Mann* and *G. Zweig* in order to explain the observed spectrum of strongly interacting particles (hadrons) in high-energy collision experiments. The subsequent discovery of quarks as their constituent particles, which are held together by the strong force thus forming bound states, provided a systematisation of hadrons into two families: mesons and baryons. Mesons<sup>4</sup> consist of a quark and an anti-quark, respectively, whereas baryons<sup>5</sup> contain three quarks each. In order to reconcile the baryon spectrum with the spin-statistics theorem, *O.W. Greenberg* introduced in 1964 the concept that quarks carry an additional quantum number (color).

The mass of a hadron, especially those that contain only light quarks<sup>6</sup>, is not derived from its valence quarks, but rather dynamically created by strong interaction, which is described by a fundamental gauge theory called Quantum Chromodynamics (QCD). The elementary color-charged particles of this theory, quarks and anti-quarks, interact in analogy to Quantum Electrodynamics (QED) via bosonic gauge fields, whose quanta form an octet and are called gluons as they “glue” the quarks together into bound states.

The lightness of the u and d quarks, which form protons (uud) and neutrons (udd) and therefore the ordinary nuclear matter that constitutes our world,

---

<sup>1</sup> gravitational, electromagnetic, strong and weak interaction

<sup>2</sup>  $10^{-15}$  m

<sup>3</sup> The name “quark” was taken from the novel *Finnegans Wake* by *James Joyce* - “Three quarks for Muster Mark!” book 2, episode 4.

<sup>4</sup> deduced from the Greek word for medium

<sup>5</sup> deduced from the Greek word for heavy

<sup>6</sup> i.e. u (up), d (down) and s (strange) quarks

gives rise to a special symmetry<sup>7</sup>. This so-called chiral symmetry<sup>8</sup> causes that the left-handed and right-handed terms of quark fields in the corresponding Lagrangian transform approximately<sup>9</sup> independent under it.

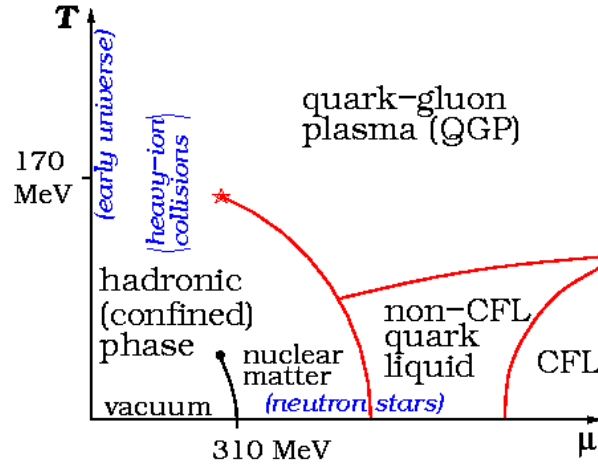


Figure 1: Phase diagram of strongly interacting matter [ASRS08], explanation is given in the text.

Depending on the temperature  $T$  and the baryon density  $\rho$ , which is equivalent to the chemical potential  $\mu$ , nuclear matter can appear in different phases, what is depicted in figure 1. Nevertheless, the phase diagram of QCD is neither theoretically nor experimentally well known and requires further investigation.

At very low temperatures and/or densities (QCD vacuum), chiral symmetry is spontaneously broken by the quark condensate, which represents a super-fluid phase, causing that the effective quark masses are non-zero and thus producing the spectrum of the very light hadrons. However, calculations predict a decreasing value of the quark condensate in hadronic matter, i.e. when temperature and/or density are raised and therefore a partial restoration of chiral symmetry. The confined gaseous phase (hadron gas) at low temperatures and densities consists mostly of individual nucleons. With increasing density, nuclear matter favours a liquid state. Ordinary matter exists at the phase boundary between QCD vacuum and nuclear matter (black curve in figure 1) in a mixed phase, which consists of nuclear droplets (nuclei) surrounded by vacuum and is assumed to behave like a liquid. At densities that are significantly higher than those in ordinary nuclei, a solid phase could exist if simultaneously the temperature is low enough (e.g. in the interior of a neutron star). At the highest

<sup>7</sup>  $SU(2)_L \otimes SU(2)_R$

<sup>8</sup> Chirality characterizes the orientation of the internal particle spin with respect to the direction of motion.

<sup>9</sup> The corresponding (pseudo-)Goldstone bosons are the three pions -  $\pi^\pm$  and  $\pi^0$  - which are in reality not massless as the  $SU(2)_L \otimes SU(2)_R$  chiral symmetry is explicitly broken due to the small and finite masses of the u and d quarks.

densities, matter is expected to be found in a degenerated liquid of quarks (color superconductor) in a color-flavour locked phase (CFL). The nature of the region beyond this phase (non-CFL) at intermediate densities is unknown, one expects some other phases that might be color-superconducting or not. When the temperature and/or the density is increased to very high values, hadrons are proposed to dissolve into a quark-gluon plasma, which represents a de-confined phase. This expectation gives rise to the assumption that there exists a critical point in the QCD phase diagram, beyond which a continuous phase transition from confined to de-confined states might occur. In [BR96] it is discussed whether such a phase transition into a de-confined state goes along with the restoration of chiral symmetry and in consequence with a vanishing quark condensate or not.

Based on the non-Abelian character of QCD, interesting effects such as gluon-gluon interaction<sup>10</sup>, color confinement<sup>11</sup> and asymptotic freedom<sup>12</sup> are observed. They are the result of the running QCD coupling constant  $\alpha_S$  and exacerbate a unitary description<sup>13</sup> of the strong interaction.

For this reason, the phase diagram of nuclear matter has been studied intensively over the past decades with the attempt to achieve a fundamental understanding of QCD and its effects. The proposed existence of new phases, the description of dense nuclear matter by an equation of state (EOS) and the observation of in-medium effects, which manifest themselves in changing hadronic properties, are topics that attract large interest.

[PS95] [Cha01] [ASRS08] [Fri11]

## 1.1 In-Medium Modification of Hadrons

Over the past decades, the study of hadron properties has attracted intensive investigation in experiments and theory, respectively. The hadron size, mass and other properties are expected to change in nuclei since hadrons consist of

<sup>10</sup> As gluons themselves carry color charge, they can interact among each other.

<sup>11</sup> The force between quarks does not diminish on separation; hence quarks do not appear in isolation but are always bound in hadrons. Moreover, the confinement property requires the total strong (color) charge between quarks to vanish, thus forming color-neutral or “white” hadrons.

<sup>12</sup> With increasing energy scale, the coupling constant  $\alpha_S$  runs towards a smaller value. From this behaviour it is expected that hadrons dissolve into individual quarks at very high temperatures and/or densities, causing quarks and gluons to become free and to form a quark-gluon plasma. The transition into a de-confined phase has been proven by lattice QCD calculations in [FH11].

<sup>13</sup> Chiral perturbation theory (ChPT) and lattice QCD have been successfully applied to describe low energy effects, whereas perturbative methods are limited to the high-energy regime.

constituent particles (quarks). In particular, the modification of hadron masses in hot and/or dense nuclear matter has been studied in connection with QCD and the equation of state of nuclear matter, e.g. [BR91] [SMB97] [PGSG99].

In this field, several theories have been developed, i.e. [NJL61], [HK94] and [BR96], but so far there is no clear experimental information available. In order to study the behaviour of hadron masses in medium, the investigation of the scalar mass is of particular importance. But medium-modified effective masses can not be directly deduced from experimental observables, since invariant mass spectroscopy of hadrons in nuclear matter rather provides the respective energy state, which is suffering from collisional shifts and broadening due to the hadron-nucleus potential, than the scalar hadron mass itself [AY99].

A possible method to overcome this problem involves the search for deeply bound states that contain the respective hadron (in-medium hadron mass spectroscopy). This method has already been successfully applied to deeply bound pionic states, where the narrow 1s and 2p states of the  $\pi^-$  meson had been investigated in  $^{205}\text{Pb}$  and  $^{207}\text{Pb}$  as theoretically predicted by [TY88]. The production of such “pionic atoms” enabled the measurement of the  $\pi^-$  mass shift in the nucleus (lead), which is deduced from the strength of the pion-nucleus interaction, thus delivering the effective mass of the  $\pi^-$  meson in the nuclear medium [Yam+96] [WBW97] [Yam+98] [IG+00] [Gei+02]. From this mass shift, a partial restoration of the chiral symmetry breaking was indicated in [Wei01].

Since most of the experimental observations of in-medium hadron (i.e. meson) mass modification have been performed in the environment of nuclear matter, a discussion on the possibility of bound strange matter has been launched. It focuses on strange hadronic matter that is composed of nucleons and hyperons and speculated to be stable with respect to weak hadronic decays [SDG+94]. Hence, the exploration of meson masses in the environment of stable strange hadronic matter, which could in turn serve as signal for the possible formation of strange hadronic matter in heavy-ion collisions, has become an interesting topic [PGSG99].

In hot and dense matter the chiral symmetry is expected to be partially restored, leading to so-called in-medium effects. Indeed, theoretical investigations predicted an in-medium mass modification of charged kaons ( $K^+$ ) and anti-kaons ( $K^-$ ) due to a possible partial restoration of the chiral symmetry in the medium in an effective chiral model, which is based on the symmetries of QCD.

In particular, studies within chiral perturbation theory (ChPT) have shown that the  $K^+$  meson sees a slightly repulsive potential in the medium, whereas the  $K^-$  meson feels a strong attraction. The strength of these effects and therefore the  $KN(\bar{K}N)$  potential depends, as depicted in figure 2, on the density  $\rho$

of nuclear matter. It has been already considered in [KN86] that the anti-kaons may condense due to the attractive interactions with a dense baryonic environment, whereas the kaons will not. Additionally, the mean free path (see table 6) of the  $K^+$  meson is long enough to escape the collision zone without further interaction with the nuclear environment. Thus, in [LK95] the  $K^+$  flow was predicted to be sensitive to a change of kaon masses in dense matter, what should be reflected in modified production probabilities of kaons and anti-kaons. For this reasons, the study of the  $K^+$  meson production was proposed to be a promising tool to probe the dense interior of the collision zone of heavy-ion reactions, thus allowing to investigate the change of hadronic properties in dense media.

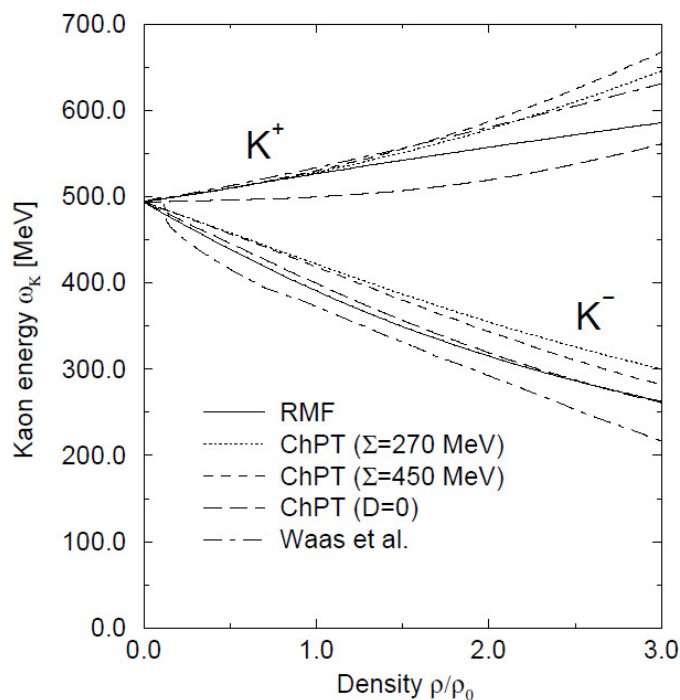


Figure 2: Energy (effective mass) of  $K^+$  and  $K^-$  mesons at rest in nuclear matter as function of the baryon density  $\rho$ . The different curves summarize the results of several theoretical calculations [SMB97]. The  $K^+$  mass is slowly growing with increasing density, whereas the  $K^-$  mass decreases.

Indeed, several heavy-ion experiments<sup>14</sup>, which studied the production of  $K^\pm$  below threshold and measured the flow of the  $K^+$  mesons, have supported these theoretical works by demonstrating sizeable medium effects [SMB97] [Cha01].

<sup>14</sup> In particular at SIS energies where kaons,  $\Phi$  mesons,  $\Lambda^0$ - and  $\Sigma$ -Hyperons can be produced: KaoS and FOPI collaboration [Cro98] [Sen04] [Foe+07] and HADES collaboration [Aga+09].

Nevertheless, after two decades of experimental study in this field, further investigations are needed in order to achieve a better understanding of the in-medium interaction potentials between kaons (that contain s quarks) and nucleons (protons or neutrons that contain only u and d quarks), which are responsible for the observed kaon mass modification [Aga+09].

On the basis of the strength of the attractive potential between  $K^-$  mesons and nucleons ( $NK^-$  potential), the possible formation of “cold” and dense bound states, which consist of an anti-kaon and two or more nucleons<sup>15</sup>, has been predicted and described by several theoretical approaches. These so-called kaonic nuclear clusters (KNC) are currently under investigation in stopped  $K^-$  beam experiments and in pp reactions. Their formation could provide information on the modification of the kaon mass and the  $\bar{K}N$  interaction in nuclear medium.

## 1.2 Kaonic Nuclear Clusters

As already outlined, is the question how hadron masses and hadron interactions change in nuclear medium, one of the important, yet unsolved, problems in hadron physics. So far, a sufficient experimental method for the derivation of in-medium scalar hadron masses has not been established, although the topic is considered to be of major importance. Invariant mass spectroscopy, which is applied to hadrons that are embedded in nuclei, rather gives information on the respective energy state than about the scalar mass itself, thus suffering from collisional shifts and broadening in the nucleus due to the hadron-nucleus potential [AY99].

The possibility of a dropping  $K^-$  mass (see figure 2 in section 1.1) has been theoretically and experimentally studied, revealing that the  $K^-$  feels an attractive potential in the nuclear environment. In this field, several experiments engaging kaon beams have been carried out with the intent to study the existence of deeply bound kaonic states, which offer a new type of “in-medium hadron mass spectroscopy”. It involves the search for a deeply bound hadronic state, which probably allows to deduce the hadron-nucleus potential and subsequently the in-medium hadron mass, once the binding energy has been measured.

The possibility of such exotic states has been predicted by *S. Wycech* and *R. Staronski* [Wyc86] [SW86] in 1986 and by *Y. Akaishi* and *T. Yamazaki* [AY02] in 2002 based on a semi-empirical model.

They predict nuclear  $\bar{K}$  ( $K^-$  or  $\bar{K}^0$  meson) bound states, so-called kaonic nuclear clusters (KNCs), which consist of nucleons that are strongly bound to a  $\bar{K}$  meson. Due to the strength of the  $\bar{K}N$  attractive interaction, the system

---

<sup>15</sup> e.g. pp $K^-$ , ppp $K^-$ , pnn $K^-$  ...

is suggested to be stable and compact and the binding energies are considered to be rather large such that these states fall below the  $\bar{K}N \rightarrow \Sigma\pi$  threshold. Hence, KNCs should be characterized by narrow widths. Such deeply bound states are studied mostly in light nuclei, where the core nuclei are largely compressed due to the strong attraction of a phenomenologically constructed  $\bar{K}N$  interaction in the  $I=0$  channel.

Such a highly attractive potential results from the assumption that the well-known  $\Lambda(1405)$  resonance is not an ordinary elementary particle or an excited three-quark state, but the bound state of  $K^- + p$  in the  $I=0$  channel. From such a potential deeply bound nuclear states in heavier nuclei are expected. In this process, the attractive  $K^-$  meson plays a unique role in binding additional nucleons more tightly, what results in a nucleus of much higher density. Hence, the  $pK^-$  ( $\equiv \Lambda(1405)$ ) state could serve as a doorway for the formation of KNCs by catching more nucleons.

Table 1 shows the main properties - mass  $m$ , width  $\Gamma$ , binding energy  $B_K$  and decay channels with their branching ratios<sup>16</sup> (BR) - of the  $\Lambda(1405)$  resonance. It is located slightly below the  $\bar{K}N$  but above the  $\Sigma\pi$  threshold. It was observed in the invariant mass spectrum of  $(\Sigma + \pi)^0$ , which represents the only channel that provides information below the  $\bar{K}N$  threshold. The nature of the  $\Lambda(1405)$  resonance [HJ12], however, is still not completely understood.

$\Lambda(1405)$	$m$ [MeV]	$\Gamma$ [MeV]	$B_K$ [MeV]	decay channel	BR [%]
$I(J^P) = 0(\frac{1}{2}^-)$	1405.1	50	27	$\Sigma^0 + \pi^0$ $\Sigma^+ + \pi^-$ $\Sigma^- + \pi^+$	$\left. \begin{array}{l} \\ \\ \end{array} \right\} 100$

Table 1: The  $\Lambda(1405)$  resonance, which is located below the  $\bar{K}N$  threshold [PDG] [AY107].

The lightest and simplest representative KNC of this nature, the  $ppK^-$  state, was predicted by *Y. Akaishi* and *T. Yamazaki* in 2002 with a binding energy of 48 MeV and a width of 61 MeV and serves as an important prototype for considerations in this field. It is also known as *nuclear kaonic hydrogen molecule* or *kaonic dibaryon* and has been investigated with variational approaches<sup>17</sup> and three-body (Faddeev) calculations<sup>18</sup> [AY02] [AY06].

<sup>16</sup> Fraction of a particle species, which decays into a specific decay mode with respect to the total number of decaying particles of this species.

<sup>17</sup> Variational calculations on the  $ppK^-$  state have been carried out by *Y. Akaishi* and *T. Yamazaki* [AY107], *S. Wycech* and *A.M. Green* [WG09], *A. Dote*, *T. Hyodo* and *W. Weise* [DHW09] and others.

<sup>18</sup> Besides the phenomenological ansatz of the semi-empirical model used by *Y. Akaishi* and *T.*

Besides the phenomenological construction of the attractive  $\bar{K}N$  potential by fitting the free  $\bar{K}N$  scattering data [Mar81], strong-interaction  $1s$  level shifts of kaonic hydrogen [Iwa+97] and the binding energy and width of the  $\Lambda(1405)$  resonance, which is seen as  $pK^-$  bound state, another attempt, which also reproduces the experimental data on the  $\Lambda(1405)$ , involves an effective chiral meson-baryon SU(3) Lagrangian. The results differ strongly from the purely phenomenological approach<sup>19</sup>, as the resulting effective potential is significantly less attractive in the energy range that is relevant for the discussion of deeply bound KNCs [WKW96] [HW08]. The phenomenological model is also criticized in [OT06] for the various approximations it has to deal with. In particular it is stated that making these approximations leads to the prediction of an extraordinarily deep potential of the  $\bar{K}N$  interaction, which constitutes the basis of the KNC formation in these semi-empirical models. It is further claimed that without these approximations the strength of the attractive potential would be shallower by approximately a factor of ten.

### 1.2.1 Structure of the $ppK^-$ State

According to *Y. Akaishi* and *T. Yamazaki* [AY02], the structure of the  $ppK^-$  state originates from a  $K^- + p$  interaction, which is derived in a phenomenological model that aims at reproducing the binding energy  $B_{K,\Lambda(1405)} = 27$  MeV and the width  $\Gamma_{\Lambda(1405)} = 50$  MeV of the  $\Lambda(1405)$  resonance, whose properties are listed in table 1.

In their model [AY107], they solved the three-body system  $ppK^-$  exactly in a variational method<sup>20</sup> making the ansatz that the known  $\Lambda(1405)$  resonance in the  $\Sigma\pi$  channel - in the following also denominated as  $\Lambda^*$  - represents the  $I = 0$   $1s$   $pK^-$  bound state.

Figure 3 depicts the predicted structures of the  $pK^-$ , which represents the  $\Lambda(1405)$  resonance (or  $\Lambda^*$ ), and the  $ppK^-$  states with their corresponding rms<sup>21</sup> distances. Table 2 lists the predicted properties - mass  $m$ , width  $\Gamma$ , binding energy  $B_K$  and the non-pionic decay channels with their branching ratios - of the  $ppK^-$  state.

The  $ppK^-$  is predicted to be the lightest system that follows this ansatz. It is

---

*Yamazaki*, Faddeev calculations have been performed by *N. V. Shevchenko et al.* [SGM07], *Y. Ikeda* and *T. Sato* [IS07], *E. Oset et al.* [Ose+12] and others, yielding similar properties for the light nuclear systems under investigation, which involve a  $\bar{K}$  meson as constituent.

<sup>19</sup> The semi-empirical model is neglecting the direct coupling of  $\Sigma\pi \rightarrow \Sigma\pi$  in contradiction to the coupled channel approach of chiral theory, which describes the  $\Lambda(1405)$  as  $I=0$   $pK^-$  quasi-bound state embedded in the strongly interacting  $\Sigma\pi$  continuum [HW08]

<sup>20</sup> The method is called amalgamation of two-body correlations into multiple scattering process (ATMS) and constructs, on the basis of a multiple scattering theory, a realistic wave function of a few-body system that includes correlation functions of each constituent pair,



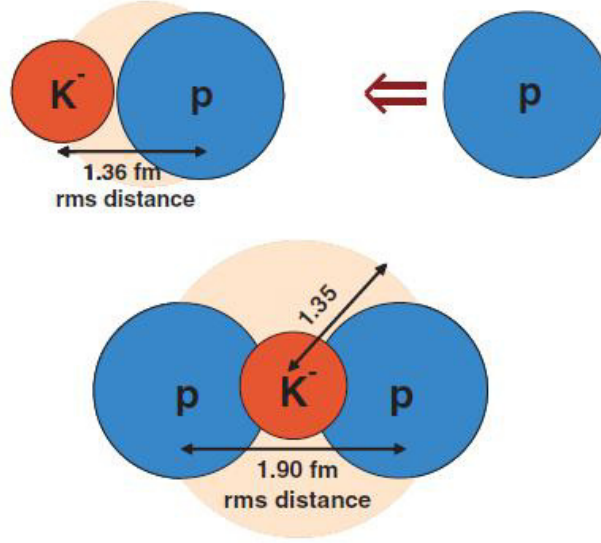


Figure 3: Predicted structure of  $pK^-$  (upper left picture) and  $ppK^-$  (lower picture) [AY107]. The  $pK^-$  could act as a doorway state for the formation of the  $ppK^-$  cluster by catching an additional proton (upper right picture).

$ppK^-$	m [MeV]	$\Gamma$ [MeV]	$B_K$ [MeV]	decay channel	BR [%]
	2322	61	48	$\Lambda + p$	50
				$\Sigma^0 + p$	} 50
				$\Sigma^+ + n$	

Table 2: The  $ppK^-$  state [AY107].

the result of a fusion of the  $\Lambda^*$  resonance and a proton. In particular the  $\Lambda^*$  dissolves into a  $ppK^-$  bound state, where the  $\Lambda^*$  may keep its original structure in the nuclear system or not. Moreover, the  $K^-$  meson is considered to play a special part in the three-body dynamics of this system through the strong attractive interaction in the  $pK^-$  state.

The result of this calculation predicts the  $ppK^-$  cluster as a compact nuclear system with binding energy of  $B_{K,ppK^-} = 48$  MeV, rms p-p distance of 1.9 fm and rms p-( $pK^-$ ) distance of 1.35 fm. As a justification it can be shown that the  $pK^-$  potential has very little energy dependence and that the results remain unchanged when the  $pK^-$  and  $pp$  interactions are varied widely, as long as they reproduce the energy and the width of  $\Lambda(1405)$ .

Moreover, it is discussed in [AY207] that the  $pK^-$  substructure, although mod-

---

which are variationally determined from a given Hamiltonian.

<sup>21</sup> root-mean square: statistical measure of the magnitude of a varying quantity

ified, persists in the nuclear bound system and might behave comparably to the Heitler-London mechanism<sup>22</sup> for the hydrogen molecule as an atomic unit in a  $ppK^-$  diatomic molecule. Similar to the molecular type binding in a hydrogen molecule, the  $K^-$  is not distributed around the centre of the two protons but rather around each of the them. Therefore it can be interpreted as migrating (or traversing) between them, producing “strong covalency” through the strongly attractive  $pK^-$  interaction<sup>23</sup>. For this reason, the  $ppK^-$  is also denominated as *kaonic hydrogen molecular ion* as its structure can be interpreted as covalent state of  $p - K^- - p$ . Figure 4 illustrates the molecular structure of the  $ppK^-$  state, namely the  $K^-$  as an “atomic center” in the  $\Lambda^*$ , which plays a unique role in producing strong covalent bonding with the other proton.

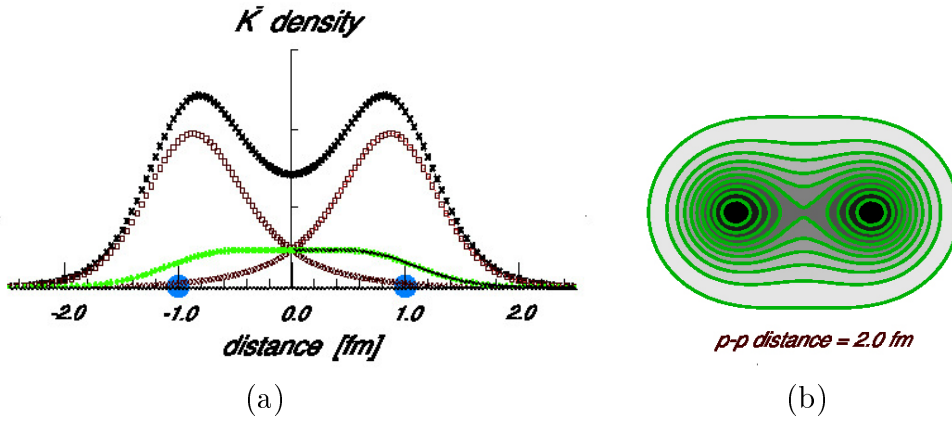


Figure 4: (a) Projected density distributions of the  $K^-$  meson in the  $ppK^-$  molecule for the fixed p-p distance of 2 fm. The distribution of the  $K^-$  (black curve) is centred around the two protons (blue dots) and consists of an “atomic” part (brown curve) and an “exchange” part (green curve) in analogy to the Heitler-London mechanism of molecular binding although the nature of the interaction is different and the migrating particle ( $K^-$ ) is heavier and bosonic [AY207]. (b) Corresponding contour distribution of the  $K^-$  meson [AY207].

In this picture, the strong  $pK^-$  attraction produces a very strong molecular type bonding of the two protons. The resulting adiabatic potential is considered to be called “Super Strong Nuclear Force” and is displayed in panel (a) of figure 5 together with the Tamagaki potential of ordinary nuclear force. The long-range attractive part together with the relatively short-range repulsive part of

<sup>22</sup> Valence bond theory of 1927 that tries to explain chemical bonding with the methods of quantum mechanics. It introduces the idea of “Platzwechsel” of a migrating real particle in order to explain the covalency in the hydrogen molecule. This molecule-type bonding mechanism was later found to be unsuccessful; instead *H. Yukawa* introduced a mediating virtual bosonic particle to describe the nuclear force. His idea led to the understanding of all fundamental forces including the electroweak interaction.

<sup>23</sup> In contrast, normal nuclear force is mediated by virtual  $\pi$  mesons according to the idea of *H. Yukawa* (see figure 5).

the potential as well as its depth is supposed to produce an enormous binding in  $K^-$ -migrating nuclear systems. The depth of the potential also signalizes that a proton, which approaches an isolated  $\Lambda^*$ , gets quickly trapped and dissolved into a  $ppK^-$  bound state. Panel (b) of figure 5 illustrates the different interaction schemes of nuclear forces, which have been developed.

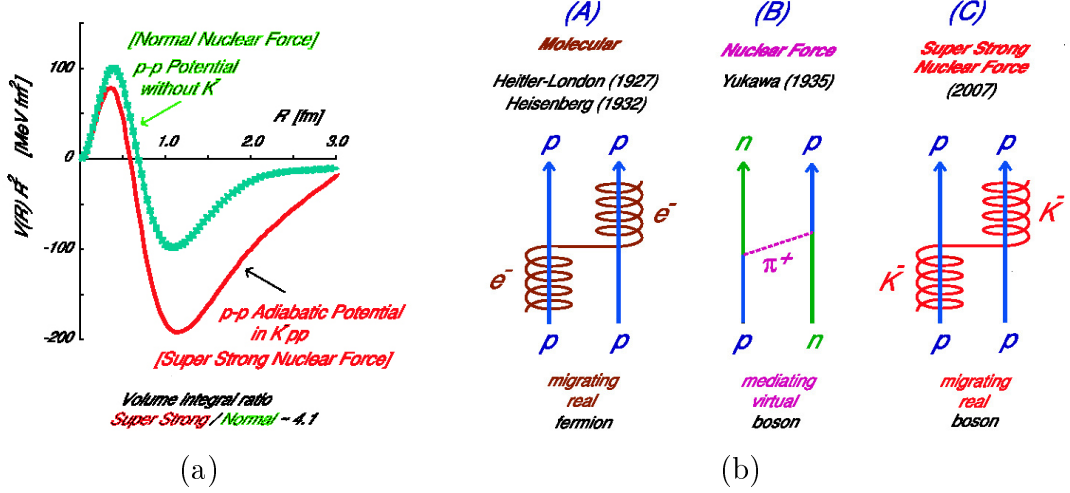


Figure 5: (a) Adiabatic potential (red curve) that results from the approach of a proton to a bound  $pK^-$  “atom” ( $\Lambda^*$ ) displayed as a function of the distance between the two protons. For comparison, the Tamagaki potential (green curve) for ordinary nuclear interaction is illustrated [AY207]. (b) Different interaction schemes for nuclear forces: (A) Heitler-London-Heisenberg model with the idea of Platzwechsel of a migrating real particle (electron) in an atomic bonding (B) Yukawa interaction where a mediating virtual particle ( $\pi$  meson) is established instead of a migrating real one (C) Super Strong Nuclear Force produced by  $K^-$  covalency as predicted by Akaishi and Yamazaki [AY207].

### 1.2.2 Kaonic Nuclear Clusters in $pp$ Reactions

Several experimental approaches have been suggested to put evidence on the existence or denial of KNCs.

In [AY02] the possible existence of nuclear  $\bar{K}$  bound states is predicted in experiments where  $K^-$  mesons are captured at rest in target nuclei such as  $^3\text{He}$ ,  $^4\text{He}$  and  $^8\text{Be}$ . The production mechanism is explained in [AY06] via a strangeness transfer reaction<sup>24</sup> involving a  $\Lambda(1405) \equiv \Lambda^*$  resonance produced in elementary processes<sup>25</sup>, which acts as doorway state for the formation of KNCs as it subsequently merges with a nucleon or nucleus in the target. But

<sup>24</sup> typically  $d(K^-, \pi^-)ppK^-$  or  $d(\pi^+, K^+)ppK^-$  with target  $d$ .

<sup>25</sup> typically  $K^- + n \rightarrow \Lambda^* + \pi^-$  or  $\pi^+ + n \rightarrow \Lambda^* + K^+$

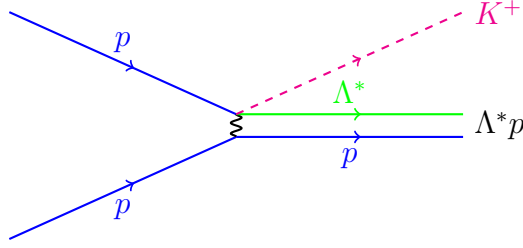


Figure 6: Reaction diagram of the formation of a  $ppK^-$  cluster in pp collisions with  $\Lambda^*p$  as doorway state.

due to the small momentum transfer of this reaction, the produced particles ( $\Lambda^*$  and nucleon) are emitted in different directions and the formation of bound states is suppressed compared to the quasi-free production process of the  $\Lambda^*$  together with a nucleon, where the  $\Lambda^*$  escapes.

In [AY06] and [AY107], however, it is considered to produce KNCs in pp collisions via the two-body final state reaction given in equation 1.1 with a dibaryonic object  $X^+$  that is associated with the  $ppK^-$  cluster.

$$p + p \rightarrow K^+ + X^+(S = 1) \quad (1.1)$$

Similarly, the  $\Lambda^*p$  system exists as a compact doorway state that either propagates to the bound state  $ppK^-$  with two-body final states or undergoes free  $\Lambda^*$  emission via the quasi-free process. Both possibilities are displayed in equation 1.2. Figure 6 illustrates the reaction diagram with the  $\Lambda^*p$  state proceeding to  $ppK^-$ .

$$p + p \rightarrow \left\{ \begin{array}{l} K^+ + ppK^- \\ K^+ + \Lambda^* + p \end{array} \right\} \quad (1.2)$$

The elementary process involving the KNC formation is considered to occur with short impact parameter and a rather large momentum transfer of about 1.6 GeV/c. In contrast to the strangeness transfer reaction, in this case the  $\Lambda^*p$  sticking probability turns out to be surprisingly high, what should result in a higher formation probability of the  $ppK^-$  cluster in comparison to the free  $\Lambda^*$  emission process. The dominance of the sticking is explained by the unusual matching of the short collision range and the small radius of the formed  $ppK^-$  bound state accompanied by a large momentum transfer.

Figure 7 depicts the calculated cross sections for the strangeness transfer and the pp reactions. The enhancement of the  $ppK^-$  formation in the case of pp collisions is clearly visible.

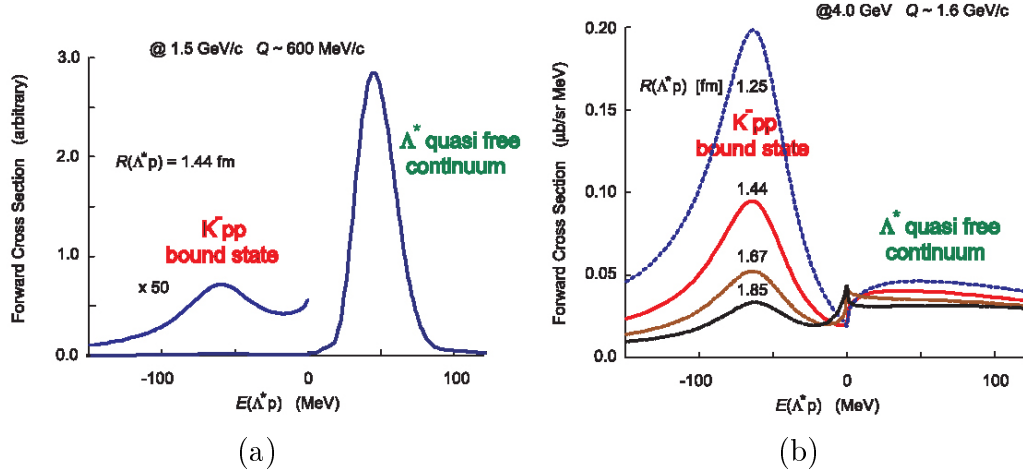
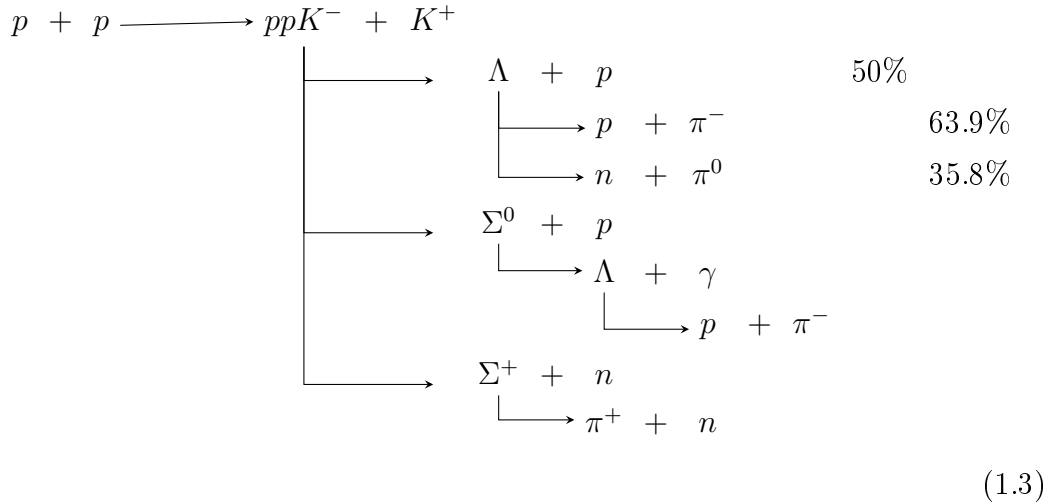


Figure 7: Cross sections for the formation of the  $ppK^-$  cluster. The strangeness transfer reactions (a) are dominated by the quasi-free process where the  $\Lambda^*$  escapes, whereas in pp collisions (b) the formation of the  $ppK^-$  dominates. The various curves in (b) show the cross section for different rms distances of the  $(\Lambda^*p)$  system (originally predicted  $K^-(pp)$  distance: 1.67 fm). With hypothetically denser systems (1.44 fm or 1.25 fm) the peak height significantly rises, what is interpreted as a proof that the sticking dominance of  $\Lambda^*p$  is the result of the dense KNC that is to be formed [AY107].

### 1.2.3 Reaction Kinematics of the pp Collisions



For the experimental observation of the  $ppK^-$  cluster in pp collisions, a study of its decay products has to be performed. The main decay channel is pionic:  $ppK^- \rightarrow \Sigma + \pi + p$  [AY107]. According to [IKMW08], from the interaction of a  $K^-$  meson with two protons one also expects hyperon-nucleon pairs (non-pionic channels) as displayed in equation 1.3.

The elementary reaction shown in equation 1.1 with the object  $X^+$  is a reaction of two-body final states. Therefore, the mass of the object can be searched for in a missing mass distribution of the  $K^+$  meson and simultaneously in the invariant mass spectrum of the respective decay daughters shown in equation 1.3.

In [AY107] kinematical relations, based on the reaction given in equation 1.1, have been calculated with an incident beam energy<sup>26</sup> of 3 GeV. Figure 8 illustrates the simulated kinematical distributions of the  $K^+$  mesons and the  $ppK^-$  cluster for the respective energy. For a given  $ppK^-$  mass of 2322 MeV according to the prediction, the laboratory momenta are unique functions of the center-of-mass and the laboratory angle, respectively. It is expected that the laboratory angle of the  $K^+$  meson ranges from 0 to a maximum of about  $50^\circ$ , whereas the  $ppK^-$  is predicted to fly out at a forward angle such that its decay products should also be forward boosted.

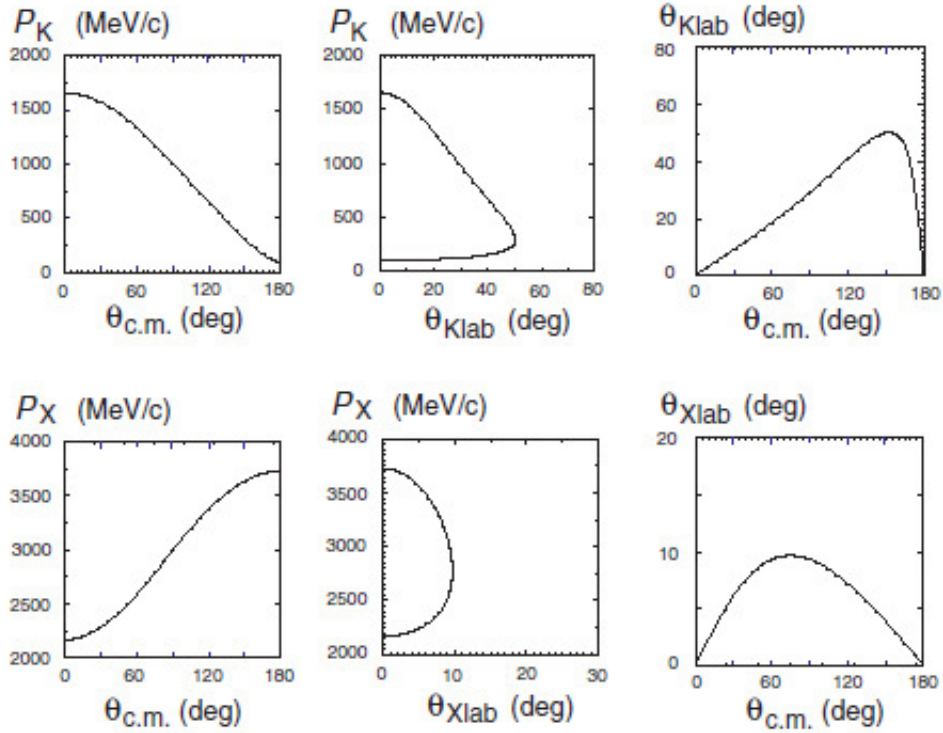


Figure 8: Simulated reaction kinematics for equation 1.1 at a proton beam energy of 3 GeV. The object  $X$  represents the  $ppK^-$  cluster [AY107].

<sup>26</sup> For this beam energy, the total production cross section of  $ppK^-$  is expected to be at its maximum value.

### 1.2.4 Experimental Results

The first experimental indications on the possible existence of KNCs were found in 2003 at KEK laboratory, where the eventual formation of the tribaryonic states  $ppnK^-$  and  $pnnK^-$  was observed. The experiment used  $K^-$  mesons, which were stopped in a liquid  $^4\text{He}$  target, and exploited the missing mass method (see section 5.1) [Suz+04].

In 2005 the FINUDA Collaboration announced that they can identify the formation of dibaryonic kaonic bound states through their decay into  $\Lambda + X$  in a stopped  $K^-$  experiment at the DAΦNE double ring  $e^+e^-$  collider at LNF. The anti-kaons were produced via the decay of  $\Phi(1020)$  mesons and stopped in various thin solid targets, e.g.  $^6\text{Li}$ ,  $^7\text{Li}$ ,  $^{12}\text{C}$  and  $^{27}\text{Al}$ . The  $\Lambda$ -Hyperons were reconstructed via their decay products,  $\pi^-$  mesons and protons, exploiting the invariant mass method (see section 5.1). Figure 9 depicts the invariant mass distribution of the  $\Lambda p$  pairs that are produced in the stopping reactions. The peak at approximately 2250 MeV was associated with the  $ppK^-$  state [Agn+05] [Agn+06].

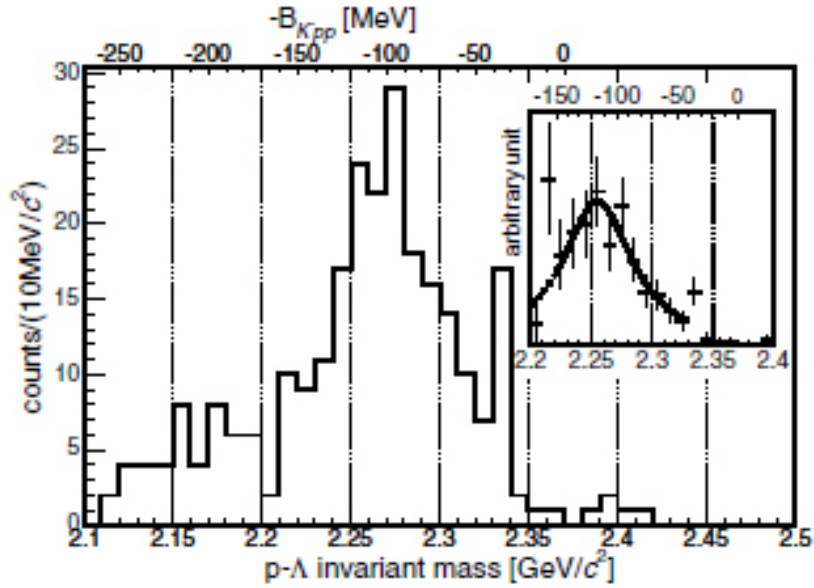


Figure 9: Background corrected invariant mass distribution  $M_{inv}(\Lambda p)$  of the FINUDA data. The binding energy  $B_K = 115$  MeV and the width  $\Gamma = 67$  MeV of the  $ppK^-$  system are obtained from fitting the spectrum with a Lorentzian function in the region between 2.22 GeV and 2.33 GeV, what is associated with the mass distribution of the  $ppK^-$ . The inset in the right upper corner shows the acceptance corrected spectrum for events that contain two protons with well-defined tracks [Agn+05].

This interpretation of the mass peak was criticized subsequently in [Mag+06].

Based on Monte Carlo simulations of the  $\Lambda p$  invariant mass distribution, it is shown that the claimed deep  $ppK^-$  bound state signal corresponds to the two-nucleon  $K^-pN \rightarrow \Lambda N$  absorption reaction, which is followed by further final-state interactions of the  $N$  or the  $\Lambda$  with the target nucleons ( ${}^7\text{Li}$ ,  ${}^{12}\text{C}$ , ...) as they leave the nucleus without forming a  $ppK^-$  bound state. For this reason they predict that no peak structure should be observed in elementary reactions, i.e.  $pp$  collisions.

The DISTO collaboration reported in 2010 on the possible discovery of the  $ppK^-$  state. The experiment was carried out at LNS, using a proton beam of 2.85 GeV from the SATURNE accelerator and focuses on the exclusive  $pp \rightarrow p\Lambda K^+$  reaction channel. The  $\Lambda$ -Hyperons were identified via the invariant mass spectrum of  $p\pi^-$  (decay daughters) and from the missing mass distribution of  $K^+$ , respectively. Figure 10 depicts the  $\Lambda p$  invariant and  $K^+$  missing mass spectra, which reveal a broad peak at 2265 MeV for the  $ppK^-$  candidate. With this result, the observed mass is close to the one that FINUDA published [Yam+10] [Yam+11].

With the OBELIX spectrometer at the LEAR complex at CERN, narrow  $\Lambda p$  peaks in the  $p\pi^-p$  invariant mass distribution in anti-proton- ${}^4\text{He}$  annihilations at rest were published in 2007. The experiment used the 200 MeV anti-proton beam from LEAR, which was slowed down and stopped in the helium target. The peak in the observed spectrum is considered as signature of the two-body decay of  $ppK^-$ , yielding a mass of 2212 MeV [Ben+07].

Overall it has to be admitted that the limited statistics of any observed signature does not allow to draw any final conclusions on the existence of KNCs so far. Table 3 summarizes the few experimental results and compares them to the predicted properties of the  $ppK^-$  cluster. It should be noticed that all of the recent experiments have suggested a bound state, which is deeper than the original prediction of *Y. Akaishi* and *T. Yamazaki* [AY107]. Clearly, more experiments in this field are needed to confirm or deny the existence of KNCs.

Experiment	m [MeV]	$B_K$ [MeV]	$\Gamma$ [MeV]
predicted [AY107]	2322	48	60
FINUDA@DAΦNE [Agn+06] stopped $K^-$ ( ${}^6\text{Li}$ , ${}^7\text{Li}$ , ${}^{12}\text{C}$ )	2255	115	67
DISTO@SATURNE [Yam+10] p+p	2265	105	118
OBELIX@LEAR [Ben+07] $\bar{p}+{}^4\text{He}$	2212	161	24

Table 3: Experimental results on the existence of kaonic bound states.

The AMADEUS project is planned as continuation experiment searching for



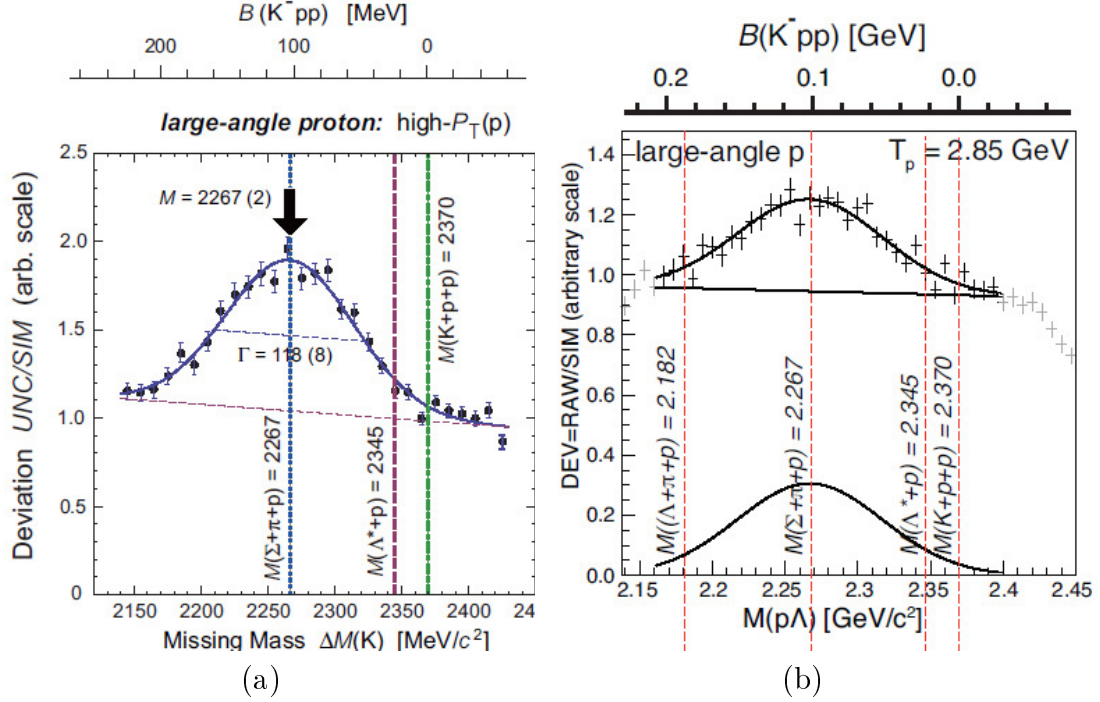


Figure 10: Missing mass distribution  $M_{\text{miss}}(K^+)$  [Yam+10] (a) and invariant mass distribution  $M_{\text{inv}}(\Lambda p)$  [Yam+11] (b) of the DISTO data for large angle protons and 2.85 GeV incident energy. The vertical lines display the thresholds of relevant decay channels. Faint points in the invariant mass spectrum were discarded from the fitting region. The binding energy  $B_K = 105$  MeV and the width  $\Gamma = 118$  MeV of the  $ppK^-$  are obtained from fitting the spectra with a Gaussian, which accounts for the peak, plus a linear background.

KNCs at LNF. Again, the DAΦNE collider will produce high rates of low energy  $K^-$  mesons through the decay of  $\Phi$  mesons. In a first step, the formation of kaonic dibaryon bound states will be investigated by stopping the  $K^-$  mesons in a  $^3\text{He}$  target. Later on a study of the kaonic tribaryon bound states, which have probably been observed at KEK, is planned by using a  $^4\text{He}$  target. The experiment will be performed with the KLOE detector, which has  $4\pi$  acceptance in measuring charged and neutral particles, respectively. KLOE will be upgraded with a special AMADEUS set-up, which enables a missing mass and an invariant mass study (see section 5.1) on the possible formation of KNCs, measuring them for the first time in the formation and the decay process, respectively [Pis11].

With an extension of the E15 spectrometer at J-Park it is planned to search for double anti-kaon nuclear bound states in  $\bar{p}$  annihilation reactions in  $^3\text{He}$  nuclei at rest:  $\bar{p} + ^3\text{He} \rightarrow K^+ + K^0 + ppK^-K^-$ . The existence of nuclear clusters, which contain more than one  $K^-$ , has been theoretically predicted in

[YDA04]. It is planned to perform a missing mass spectroscopy of  $K^+K^0$  and an invariant mass analysis of the decay daughters of the double anti-kaon nuclear cluster. The experiment also aims at studying double-strangeness production in anti-proton-nuclei annihilation. Since double anti-kaon production in the elementary anti-proton annihilation  $p + \bar{p}$  at rest is energetically forbidden, it could be produced in the nuclei due to the large binding energy of a possibly formed double anti-kaon nuclear bound state [Sak+11].

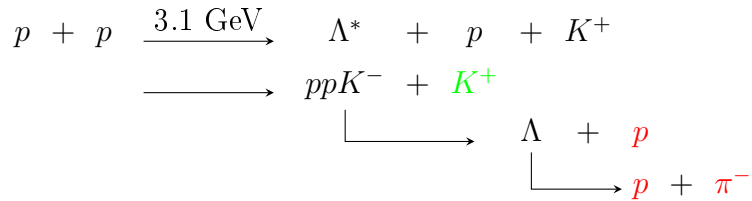
### 1.2.5 Experimental Approach at GSI

*Y. Akaishi* and *T. Yamazaki* have shown in [AY107] (see section 1.2.2) that the basic  $\bar{K}$  cluster, the  $ppK^-$ , can be formed in pp collisions since the produced  $\Lambda^*$  resonances act as doorway states forming  $\Lambda^*p$  states, which are characterized by a large sticking probability due to the short-range collisions. Hence, in pp collisions the propagation into dense  $ppK^-$  systems should dominate the quasi-free production process (see figure 7).

The analysis, which is performed in a 3.1 GeV pp fixed target experiment with the almost full solid angle covering FOPI spectrometer at GSI-SIS18, focuses on the investigation of the  $ppK^-$  cluster via its decay channel into a  $\Lambda$ -Hyperon and a proton (BR = 50%) (see equation 1.3). The  $\Lambda$ -Hyperon subsequently decays with a mean free path of about 7 cm into protons and  $\pi^-$  mesons (BR = 63.8%) [PDG]. Thus, the final state contains four charged particles - 2 protons, a  $\pi^-$  and a  $K^+$  meson, respectively, which are identified (see section 4) by combining the available information on the reconstructed particle trajectories with the energy loss information provided by the tracking detectors (see section 3.2).

In a first step, the decaying  $\Lambda$ -Hyperon can be reconstructed via its decay products with the secondary vertex reconstruction method, which involves the invariant mass technique (see sections 5.1 and 5.2.1). As shown in figure 8, the  $ppK^-$  is supposed to have rather high laboratory momenta ( $p_{ppK^-} \approx 3$  GeV/c) and is therefore emitted in a narrow forward cone with corresponding polar angles of about  $10^\circ$ . Hence, the direction of its daughters -  $\Lambda$ -Hyperon and proton - is expected to be also forward with polar angles up to  $30^\circ$ , thus requiring sufficient momentum and vertex resolution in the forward detector components of the FOPI spectrometer. For this reason, the spectrometer was updated with the new detector component SiAViO (see section 3.6), which improves the signal-to-background ratio (S/B) in the forward region and is used for the secondary vertex reconstruction by providing additional position information and as trigger to enhance the number of events containing  $\Lambda$ -Hyperons, respectively.

Secondly, the  $K^+$  meson has to be identified either directly or indirectly. Direct



$K^+$  identification is done with the time-of-flight (TOF) information (see section 4.2) provided by the FOPI TOF detectors (see section 3.3). Indirect identification is possible for events that contain four particles in the final state, having three of them identified as 2 protons and a  $\pi^-$  meson, respectively, where a proton out of the two and the  $\pi^-$  can be correlated to reconstruct the  $\Lambda$ -Hyperon. The fourth particle is assumed to be the  $K^+$  meson. Figure 8 suggests that the kaons are characterized by rather low laboratory momenta ( $p_{K^+} < 1.5$  GeV/c) and are emitted at polar angles up to  $50^\circ$  in the laboratory frame. The FOPI spectrometer enables in the respective polar angle region suitable direct kaon identification with its MMRPC sub-detectors (see section 3.3.2).

The proton beam energy of 3.1 GeV has been chosen such that the ratio of the  $ppK^-$  production probability to the main background component, i.e. strangeness production in pp collisions, is optimized. For this calculation, the production probability of the  $\Lambda(1405)$  measured by the DISTO collaboration at 2.85 GeV was taken as reference, although it includes large uncertainty. Above 2.5 GeV many strangeness production channels are open, what leads to a significant increase of the cross section. For energies above 3 GeV the relative momenta of the  $\Lambda^*$  and the proton increase, thus the sticking probability is expected to decrease. Figure 12 illustrates the expected total cross section of the  $ppK^-$  production as a function of the proton beam energy. Table 4 lists various simulated cross sections for the proton beam energy of 3 GeV. The channels, which include strangeness production, are expected to account only for approximately 5% of all possible reaction channels.

The relevant reaction channels including strangeness production (in particular a  $K^+$ ) are given in the subsequent equations. Equation 1.4 and equation 1.5 represent the two main background channels, which can show the same event topology as the signal channel (2 protons, 1  $\pi^-$ , 1  $K^+$  in the final state).

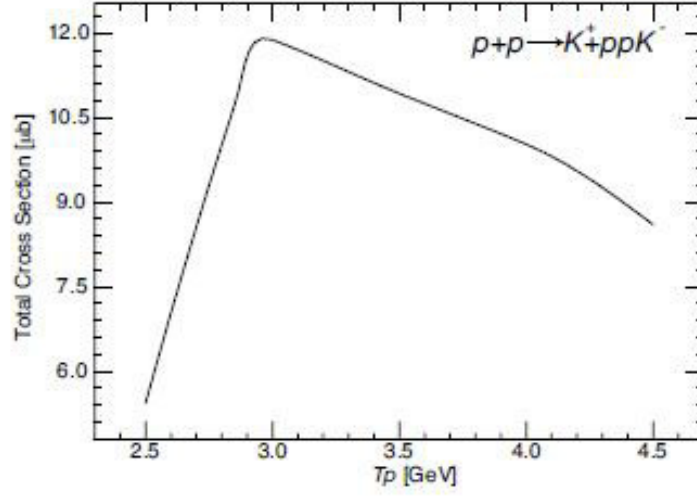


Figure 12: Total cross section for  $ppK^-$  production as function of the proton beam energy  $T_p$ . The  $\Lambda(1405)$  production probability measured by the DISTO collaboration at  $T_p = 2.85$  GeV was taken as a reference, although including large uncertainty [FCo07].

proton beam energy	3.0 GeV
$\sigma(\text{total})$ [mb]	44
$\sigma(\text{inelastic})$ [mb]	26
$\sigma(\text{strangeness})$ [mb]	0.208
$\sigma(K^+ + \text{anything})$ [mb]	0.146
$\sigma(\Lambda + \text{anything})$ [mb]	0.089

Table 4: Summary of total, inelastic, strangeness producing,  $K^+$  and  $\Lambda$  inclusive expected cross sections [FCo07].

Equation 1.6 shows the signal channel, whose branching ratio is given with approximately 1% out of the 5% strangeness producing channels.

$$p + p \rightarrow K^+ + \Lambda + p \quad (1.4)$$

$$p + p \rightarrow K^+ + \Sigma^0 + p \quad (1.5)$$

$$p + p \rightarrow K^+ + ppK^- \quad (1.6)$$

[FCo07]

## 2 The FOPI Experiment S349 at GSI

Hosted at the heavy-ion synchrotron SIS18 at research centre GSI Darmstadt near Frankfurt (Germany), the FOPI spectrometer shown in figure 13 is a fixed target experiment. The name of the spectrometer is an acronym for *FOur PI* and in this sense a synonym for the almost full solid angle coverage of  $4\pi$ . It allows to detect and determine the properties of charged particles (i.e. light mesons and protons) emitted in heavy-ion and other reactions. Neutral particles are recognized and reconstructed from their decay products. With its modular design, each detector component has been optimized for the detection of certain types of particles [FOP].

From the early nineties on, the detector set-up has been continuously modified and extended for several times. Originally designed to study nuclear fragmentation<sup>27</sup>, it has become capable of investigating pion and strangeness production [Mer04] as well as kaonic nuclear clusters with the assembly of a TOF detector consisting of multi-gap multi-strip resistive plate chambers (MMRPC; details given in section 3.3.2) and an online hardware trigger named SiAViO, which is described in section 3.6.

In the first phase of the FOPI experiment, the spectrometer consisted of a single component, namely the forward Plastic Wall (PLAWA), which is shown in blue in figure 13. It measures the energy loss, which is described by the Bethe-Bloch formula (see section 4.1), and the velocity of charged particles that are emitted from the reaction zone in the forward direction. In the next step (phase 2), the system was upgraded with a superconducting solenoid, which is shown in red and which produces a homogeneous magnetic field. Inside the magnet, a jet type drift chamber, the Central Drift Chamber (CDC) shown in yellow, was installed. It identifies particles by combining specific energy loss with the momentum of particles that are passing through its gas filled volume (see section 4). The CDC is characterized by a rather low transverse momentum acceptance, therefore it is surrounded by the Plastic Barrel (shown in blue), which consists of several plastic scintillators aligned parallel to the beam axis. With this assembly, charged kaon identification was possible up to momenta of 0.5 GeV/c. Finally, the addition of a forward drift chamber at the tail of the magnet, the Helitron, which is also shown in yellow, allows isotope separation to the particles that are identified with the PLAWA. During phase 3 of the set-up, which was completed in 2007, the Plastic Barrel was shortened and instead MMRPCs, which are shown in green, were installed to achieve an even better time resolution that allows kaon separation up to momenta of about 1 GeV/c [CBM11]. The various detector components are described in section 3.

<sup>27</sup> Several experiments have been completed over the last 20 years with different ion beams provided by SIS18 like Ni+Ni, Al+Al, Ni+Pb, Ru+Ru etc.

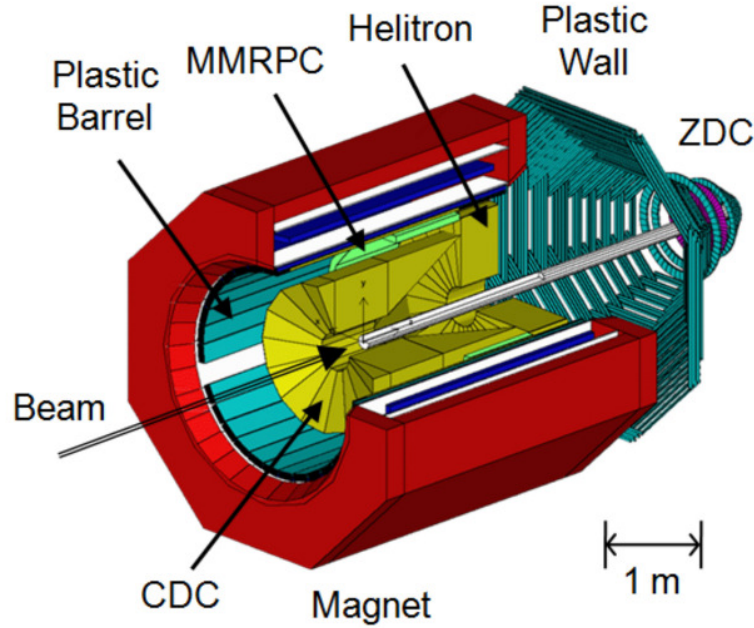


Figure 13: The FOPI spectrometer with its sub-detector systems [RHK11]: drift chambers CDC and Helitron (yellow) inside the superconducting coil (red) surrounded by the time-of-flight detectors Plastic Barrel, Plastic Wall (PLAWA), Zero Degree Counter (ZDC) (blue) and MMRPC (green).

In order to determine fundamental properties<sup>28</sup> of hadronic systems with experiments at finite temperatures and densities, measurements of in-medium cross sections and effective masses of the constituents are required. From the beginning on, the FOPI experiments concentrated on the measurement of complete phase space distributions of nucleons and heavy fragments in central heavy-ion collisions, their radial and direct flow and the analysis of produced particles as for example  $\pi$  mesons, kaons and short lived resonances and finally even strange clusters like the  $ppK^-$ , which are reconstructed via the measurement of their charged decay particles (see section 5.2) [CBM11].

Depending on the temperature  $T$  and the baryon density  $\rho$ , nuclear matter appears in different phases. As shown in the QCD phase diagram in figure 14, the SIS18 ring accelerator at GSI operates in the high density but low temperature region. Therefore physics topics at SIS energies are the phase transition from normal to chirally symmetric matter, which provide an understanding of QCD in the compressed phase.

<sup>28</sup> E.g. equation of state (EOS), which describes the properties of bulk nuclear matter

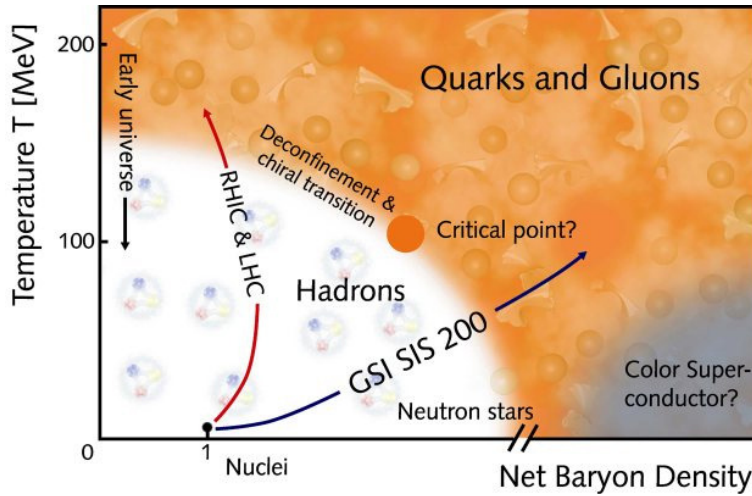


Figure 14: Phase diagram of strongly interacting matter [HIM]. In analogy to the phase diagram of water the existence of a critical point is expected at the end of the phase boundary between hadronic matter (chiral symmetry broken) and the quark-gluon plasma (chiral symmetry restored). In contrast to the sharp boundary on the right, beyond this specific point a continuous phase transition occurs. The black dot at baryon density 1 indicates ordinary nuclear matter.

## 2.1 Accelerator Facility at GSI

The acceleration of the ions, or protons in the case of the S349 ( $p + \text{LH}_2$ ) experiment, starts at UNILAC, the linear accelerator at GSI, which is shown in figure 15. Within 120 meters ions of all kinds and protons are accelerated up to 20% of the speed of light  $c$ . Further on, the accelerated particles are either used for experiments (in experimental hall I) or injected into the ring accelerator SIS18 for further acceleration, which has a circumference of 216 meters. It consists of two acceleration cavities and a range of deflecting and focussing magnets, which keep the charged particles on a circular path. The acceleration level that can be reached with SIS18 is up to 90% of  $c$ . Leaving the synchrotron, the particles are either guided to the experimental hall II, which contains the experimental sites including the FOPI spectrometer, or they are injected into the Experimental Storage Ring (ESR) where they are stored for further analysis [GSI].

The facility is able to deliver heavy-ion beams with energies from 0.1 AGeV up to 2 AGeV [Mer04]<sup>29</sup> and proton beams with maximum energy of 4.5 GeV, what corresponds to a momentum of 5.4 GeV/ $c$  [Mue08].

The accelerated protons in the case of S349 are directed to the FOPI target cell, where they collide with the target material  $\text{LH}_2$ , which is placed inside a superconducting coil (shown in red in figure 13) that produces a magnetic field

<sup>29</sup> A: mass number

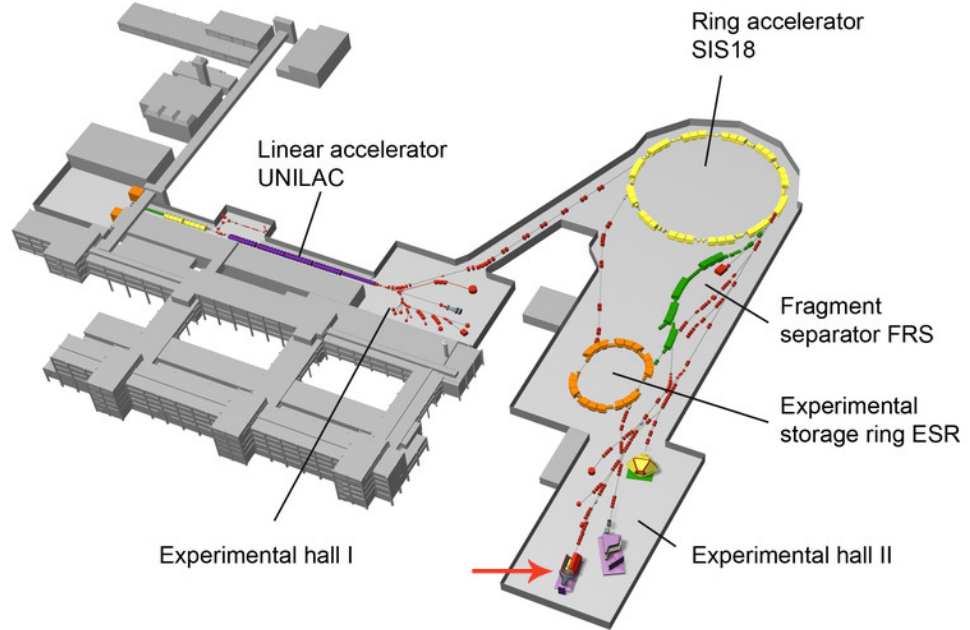


Figure 15: The accelerator facility with the heavy-ion synchrotron SIS18 at GSI [GSI]. The red arrow points to the location of the FOPI spectrometer in experimental hall II.

of 0.6 Tesla parallel to the beam axis. The nuclear matter, which is created as a result of this proton-proton collisions, is detected in the sub-detectors of the FOPI spectrometer either directly, as for example in the case of protons and pions, or via its decay products as in the case of short-lived particles like the  $\Lambda$ -Hyperon. For the event analysis it is important to identify all produced particles, what can be done by measuring their characteristic properties [Mue08].



### 3 Detector Set-up

The FOPI spectrometer comprises several sub-detectors which are schematically depicted in figure 13. Resulting from pp collisions in the target cell, charged particles travel along curved paths within the solenoidal magnetic field before they pass through the drift chambers CDC and Helitron (shown in yellow in figure 13), which are placed inside the magnet [FOP]. With the information they provide, track reconstruction can be done. For this purpose one requires the momentum and the charge polarity of the particles, which are determined by the curvature of the track in the magnetic field [Mue08].

Further on their passage through the sub-detectors, the majority of the particles goes through the scintillation counters (shown in blue and green in figure 13). The Plastic Barrel and the MMRPC are placed inside the magnet, PLAWA and ZDC are located downstream in forward direction. They allow to determine the flight time of the particles from the start detector, which is placed in front of the target [FOP]. Moreover, they allow to extract the particle momentum and to calculate the velocity of the particle from the particle trajectory and the measured flight time [Mue08].

By combining the various measured information, an unambiguous identification of the particles is achieved [FOP]. Further details of this procedure are given in section 4. The following sections give an overview of the FOPI spectrometer.

#### 3.1 Superconducting Solenoid Magnet

The FOPI magnet surrounds the drift chambers CDC and Helitron and the TOF detectors PLAWA and MMRPC as shown in figure 13. It produces a homogeneous solenoidal<sup>30</sup> field of 0.6 T parallel to the beam axis  $z$ , which is reached at a current of 720 A, and it has a diameter of 2.4 m and a length of 3.3 m. The total and transverse momenta of charged particles travelling along helical trajectories through the magnetic field can be determined from the curvature of their paths in the  $x$ - $y$  plane and the polar angle  $\vartheta$  [Mer04] [Ryu09].

#### 3.2 Drift Chambers

For the purpose of tracking the FOPI spectrometer uses drift chambers (or multi-wire chambers) as tracking detectors. They basically consist of planes

---

<sup>30</sup> A solenoidal field is aligned parallel to the beam axis  $z$ :  $\vec{B} = (0, 0, B_z)^T$

of parallel aligned field cage and signal wires (anode plane), which are placed inside a gas filled volume between two cathodes.

Electron-ion pairs, which are created through ionization of the atoms or molecules of the detector gas, are separated by an electric drift field that accelerates the electrons towards the signal wires and the ions towards the field cage in the anode plane. While drifting through the field, the charges interact with the atoms or molecules of the gas through collisions, but do not initialize an avalanche multiplication as the kinetic energy gain between two collisions far from the anode plane is too low. Instead, they acquire an average drift velocity  $v_D$ , which is described by the Maxwell-Boltzmann distribution for the mean velocity of particles at thermal energies given in equation 3.1. Electrons reach drift velocities of the order of a few  $cm/\mu s$  at room temperature, whereas the one for ions is about a factor of 100 lower [Mer04].

$$\langle v \rangle = v_D = \int_0^\infty v f(v) dv = \sqrt{\frac{8kT}{\pi m}} \quad (3.1)$$

When the drifting electrons reach the vicinity of the sense wires in the anode plane where the drift field gets inhomogeneous due to the large field gradient, they are strongly accelerated and evoke a localized cascade of ionization as they have gained enough kinetic energy now. The charge  $Q$  of this avalanche formation is proportional to the multiplication factor<sup>31</sup>  $M$  and to the primary charge  $n_0 \cdot e$  of the electrons created by the primary ionization process as given in equation 3.2. Finally, a signal is induced on the signal wires and recorded as a hit(-point) [Mer04].

$$Q = n_0 \cdot e \cdot M \quad (3.2)$$

The particle track is reconstructed by extrapolating back the recorded hitpoints from the wire position to their origin (primary vertex) in the target in the x-y plane (see section 5.2). As the drift direction of a charge carrier to the signal wires is not a priori known, the plane is characterized by a left-right ambiguity. Therefore, each real track that is distinctly marked by originating from the primary vertex in the target, is accompanied by a corresponding mirror track on the opposite side of the sense plane that does not point to the target. The problems, that occur in connection with mirror tracking can be reduced by certain techniques, which are described in section 3.2.1. The z coordinate along the wire can be determined with the charge division method, which uses the ratio of the charges that are collected on both ends of a signal wire.

---

<sup>31</sup> depending on the gas mixture in use and the field configuration around the sense wires

The drift chambers of the FOPI spectrometer - CDC and Helitron - therefore allow to determine the particle track, i.e. its curvature  $r_c$ , its charge and transverse momentum  $p_t$  (see equation 4.2), and the energy loss sustained by a charged particle while passaging through the detector gas, loosing energy by ionizing its atoms or molecules. The mean energy loss is characterized by the particle species and its momentum as described by the Bethe-Bloch formula, which is given in equation 4.4 [Mer04] [FOP].

The procedure of particle identification with drift chambers is described in more detail in section 4.1.

### 3.2.1 Central Drift Chamber

The CDC is a cylindrically shaped jet chamber with conical end caps and the main tracking detector of FOPI spectrometer. Its active volume has a length of 2 m, a diameter of 1.8 m and is filled with a gas mixture of 88% Ar, 2% C<sub>4</sub>H<sub>10</sub> (isobutane) and 10% CH<sub>4</sub> (methane) [Ryu09] [Ben07].

Originally designed for heavy-ion physics, its resolution is not limited by diffusion and allows therefore to measure events with high local track density, what is characteristic for heavy-ion reactions. Moreover, it can be operated at high event rates due to short drift paths of the order of a few cm, what corresponds to electron drift times of the order of a few  $\mu s$  [Mer04]. This feature is important for the event analysis of pp collisions, where the detector has to deal with only a few tracks per event but a rather high event rate.

The chamber is placed inside the magnet such that the magnetic field in the drift chamber is homogeneous to a precision of better than 1%. Besides full azimuthal angle coverage ( $\phi$ ), the polar angle ( $\vartheta$ ) acceptance of this geometry ranges from 23° to 113° for a target position that is located 40 cm upstream of the nominal position as depicted in figure 16 [Ber09].

Azimuthally, the CDC is divided into 16 sectors what can be seen in figure 16. Each active sector volume is encapsulated by a field cage consisting of 252 cathode wires<sup>32</sup> parallel to the beam axis. It separates each sector from its neighbours and produces the homogeneous electric drift field of about 800 V/cm by applying a voltage of -15 kV to its wires. The anode plane placed in the middle of each sector consists of 61 potential wires<sup>33</sup> and 60 sense wires<sup>34</sup> and is aligned parallel to the beam axis, but radially tilted<sup>35</sup> by 8° to reduce mirror

---

<sup>32</sup> diameter: 125  $\mu m$

<sup>33</sup> or field cage wires; diameter: 125  $\mu m$

<sup>34</sup> or signal wires; diameter: 20  $\mu m$

<sup>35</sup> The tilting of the sense plane has the effect that mirror tracks never originate from the primary vertex and helps therefore to clearly distinguish them from the real ones.

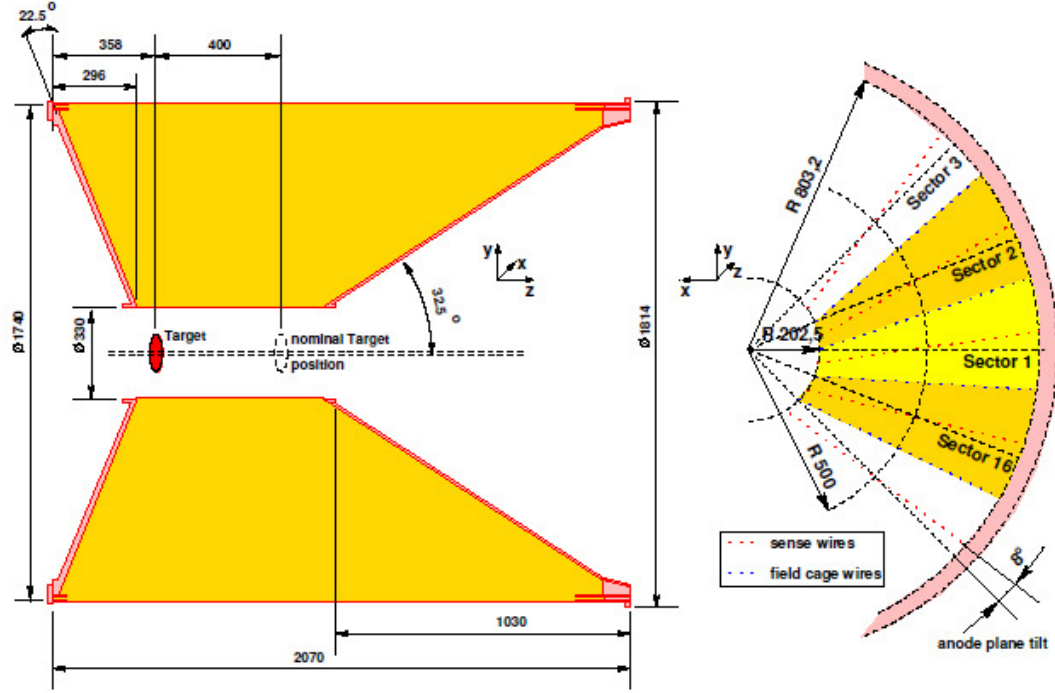


Figure 16: Cross sections of the CDC: longitudinal on the left hand side of the picture and transversal on the right hand side [Mer04].

tracking problems in addition with an alternately displacement (staggering) of the sense wires by  $\pm 200 \mu\text{m}$  with respect to the anode plane. This results in a better fit quality for the real track in comparison to the mirror track. The sense wires are grounded, while a voltage of  $-1275 \text{ V}$  is applied to the potential wires in order to produce the electric field for electron multiplication. The radial positions of the wires range from 20 cm to 80 cm, corresponding to the inner and outer radius of the chamber. The CDC achieves a position resolution in the x-y plane that is better than  $500 \mu\text{m}$  and the z position can be calculated with a precision of a few cm [Mer04].

### 3.2.2 Helitron

In the forward region, tracking of charged particles is achieved by a radial drift chamber named Helitron, which contains the same gas mixture as the CDC. The polar angle acceptance for the target position 40 cm upstream (to the nominal target position) lies between  $10^\circ$  and  $22^\circ$  and it also covers full azimuthal angle [Mer04] [Ber09]. Its geometry is cylindrical with inner and outer diameter of 42 cm and 198 cm, respectively, and a length of 60 cm [Ple12].

The Helitron is located directly behind the CDC, downstream the beam axis

at the very end of the magnetic yoke and falls therefore already in the inhomogeneous region of the magnetic field. Charged particles traversing through the detector gas form trajectories in the shape of helices, what is the origin of the name Helitron [Ber09].

Due to its position in the FOPI spectrometer far from target, the Helitron cannot be reasonably used for secondary vertex reconstruction as it has a lower momentum resolution than the CDC. Nevertheless, for the S349 experiment it is essential to have sufficient tracking in the forward region, because the  $ppK^-$  is assumed to be emitted with relatively small polar angles, what means that its decay products mainly fall into the Helitron acceptance. To overcome the low signal-to-background ratio, an additional hitpoint is delivered by a newly installed component located close to the target - the online hardware  $\Lambda$  trigger SiAViO described in section 3.6 - that enhances the secondary vertex reconstruction capability of the Helitron [FCo07] [Ber09].

The electric drift field is generated by cathode wires that separate the active volume of the chamber azimuthally into 24 sectors. Each sector contains in its middle the anode plane, which consists of 54 potential wires<sup>36</sup> producing the electric field for the electron avalanche by applying a voltage of -1.6 kV and 53 sense wires<sup>37</sup> that collect the charge [Mer04]. As a consequence of the helix trajectories, the wires are spanned radially and are therefore perpendicular to the beam axis. To determine between mirror hits and hitpoints originating from the target, the sense wires are staggered similarly to the ones in the CDC. By applying a voltage of -12.3 kV to the cathode wires a homogeneous drift field of 750 V/cm is generated [Ple12].

### 3.3 Time of Flight Detectors

The FOPI spectrometer contains several detectors for time-of-flight (TOF) measurement of particles that traverse through the drift chambers.

In order to discriminate between different types of particles, the particle's velocity  $v$  has to be determined from its flight time  $\Delta t$  between two scintillation counters and its reconstructed flight path length<sup>38</sup>  $L$  as displayed in equation 3.4. For this purpose, one uses a start and a stop signal. They are generated by a start detector in front of the target (see section 3.4.1) and several TOF detectors arranged around the drift chambers, respectively [Mue08]. These detectors are described in the following subsections. Together they deliver the

---

<sup>36</sup> diameter: 125  $\mu m$  [Ber09]

<sup>37</sup> diameter: 50  $\mu m$  [Ber09]

<sup>38</sup> The flight path length  $L$  can be calculated from the curvature radius  $r_c$  of the particle trajectory, the polar emission angle  $\vartheta$  and the distance from the beam axis to the scintillators,  $r_B$  [Ryu09].

arrival times of the signal at both ends of the scintillator bars of the TOF detectors,  $t_R$  and  $t_L$ , from which the flight time can be calculated as shown in equation 3.3 [Ryu09].

$$\Delta t \propto \frac{t_R + t_L}{2} \quad (3.3)$$

$$v = \frac{L}{\Delta t} \quad (3.4)$$

In addition to the time-of-flight information, the scintillator bars are able to provide an extra hitpoint if the signal is read out on both sides of the bar,  $t_L$  and  $t_R$ . In this case, the  $z$  coordinate of the hit position along the scintillator bar can be extracted from the time difference between the two signals at both ends of the scintillator bar [Ryu09].

$$z \propto \frac{t_R - t_L}{2} \quad (3.5)$$

When charged particles fly through a scintillating material<sup>39</sup> that is characterized by exhibiting scintillation on ionization, luminescent light of a characteristic spectrum is emitted as the result of the de-excitation process. These photons are guided by total reflection through the material, which is transparent for its own emitted radiation. If this is not the case, wavelength shifters<sup>40</sup> are added to the material in order to absorb higher frequent photons and emit lower frequent ones. This can also be useful if the photo-detectors are only sensitive to a certain wavelength spectrum. Scintillator bars are usually coupled to photomultiplier tubes (PMTs) that absorb the emitted light and reemit it via the photoelectric effect as electrons, which are multiplied by dynodes into a detectable electric current that is finally read out.

The TOF detectors Plastic Wall and the ZDC in the forward direction of the FOPI spectrometer are also suitable to serve as an online trigger device (LVL1, which is described in section 3.7), as they quickly provide information on charged particle multiplicity in a collision event [RHK11].

The procedure of particle identification by using time-of-flight detectors is described in section 4.2.

<sup>39</sup> i.e. organic and inorganic crystals, certain gases, bases, glass or plastic

<sup>40</sup> e.g. POPOP ( $C_{24}H_{16}N_2O$ )

### 3.3.1 Plastic Barrel

180 scintillator strips placed parallel to the beam axis with dimensions of  $240 \times 4 \times 3$  cm<sup>2</sup> that are grouped in 30 modules with 6 bars each, build the Plastic Barrel that covers the inner wall of the magnet and surrounds therefore the CDC. Each scintillator strip is read out by photomultiplier tubes on both sides, the time difference between the two signals yields the hit position on the strip in z direction.

The Plastic Barrel covers almost<sup>41</sup> full azimuthal angle and the polar angle range between  $39^\circ$  and  $140^\circ$ . It is characterized by a timing resolution of about 300 ps to 400 ps depending on the hit position on the strip and the luminous efficiency. This corresponds to a position resolution of about 8 cm. For a sufficient particle identification, geometrical matching between the CDC and the Barrel hits is required [Ber09] [Ryu09].

### 3.3.2 Multi-gap Multi-strip Resistive Plate Chambers

The Plastic Barrel enables sufficient proton and pion identification via time-of-flight information. In the case of kaons, identification is limited to momenta up to about 0.5 GeV/c due to the limited timing resolution of the Barrel detectors.

In order to improve the separation of protons and pions from kaons for higher momenta, a TOF detector with better time resolution was needed. With the newly installed spectrometer component MMRPC, kaons can be distinguished up to momenta of about 1.0 GeV/c, what is absolutely essential in the case of the pp experiment where the  $K^+$  mesons have to be identified in relatively small polar angle emittance [FCo07] [Mue08].

To clearly separate kaons from protons and pions, a time resolution of less than 100 ps for the full system is required. Previously the FOPI scintillation counters Plastic Barrel and PLAWA, which are characterized by a resolution of about 300 ps, have been used for the task of particle identification. Considering a time resolution of about 50 ps for the FOPI in-beam start detector as reference, the resolution that is required for the MMRPCs amounts to 85 ps in order to meet the value of the full system. In addition, the particle tracks that are detected with the CDC have to match with the hits in the MMRPC, therefore its azimuthal position resolution has to be comparable to the one of the CDC. Tests of the detector have shown that it has an intrinsic time resolution of less than 70 ps, what amounts to a total resolution of less than 90 ps, taking the time reference of the start detector into account [Kis+11]. In the case of the

---

<sup>41</sup> there are two holes of  $11^\circ$  each where the CDC is mounted; refer to figure 17 where the CDC rails are shown.

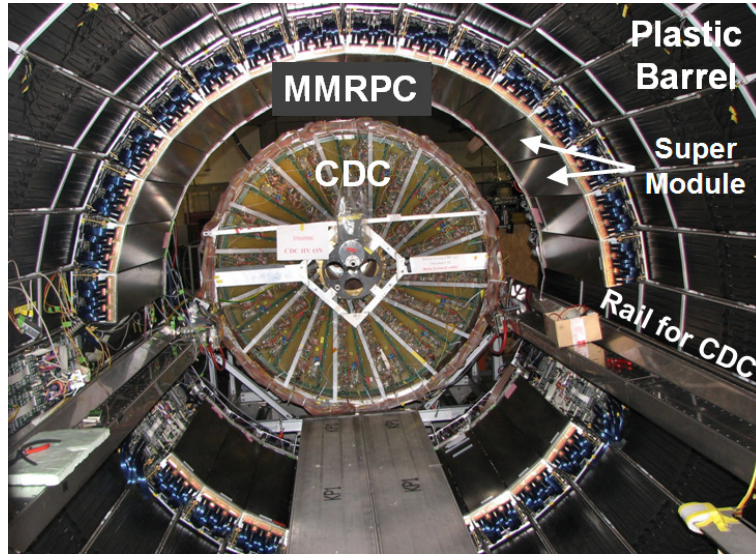


Figure 17: Picture of the Super Modules in the FOPI spectrometer, which build the MMRPC [RHK11].

pp experiment, an overall resolution of about only 180 ps is achieved due to the limiting factor of the newly installed start counter (see 3.4.1) [Ple12].

The MMRPC TOF detector was built and installed in 2007 and consists of so-called multi-gap multi-strip resistive plate chambers for precision time-of-flight measurements within polar angles of  $27^\circ$  and  $50^\circ$  for the  $\text{LH}_2$  target position (40 cm upstream the nominal one) [Ber09].

The detector consists of 30 Super Modules (SM), which are built out of a carbon fibre box with aluminium end-flanges and which is filled with a  $\text{SF}_6$  enriched gas<sup>42</sup> mixture. It is mounted between the CDC and the Plastic Barrel, what can be seen in figure 17. Each SM houses 5 individual MMRPC detectors, which are arranged in two partially overlapping layers to enhance acceptance, containing 3 and 2 counters, respectively, and high-voltage supply [Sch+06].

The MMRPC counter are improvements of ordinary RPCs, which are gaseous TOF detectors. Multi-gap RPCs are realized by inserting charge neutralizing resistive plates made out of high-ohmic material (i.e. common float window glass) into the gas volume. The outermost two plates are used as cathodes, as their outer surface is coated with copper foil. The distance between the glass plates is chosen such that primary ionization can only occur in short distances to the plates. The rest of the distance is used for the avalanche formation, which finally induces a detectable signal on the anode. Therefore, the drift time of the charge carriers that are, similarly to the process taking place in a drift chamber, created by a passing ionizing particle, is significantly shorter

<sup>42</sup> 80% R134a ( $\text{C}_2\text{F}_4\text{H}_2$ ), 15%  $\text{SF}_6$  and 5% isobutane [Kis+11].



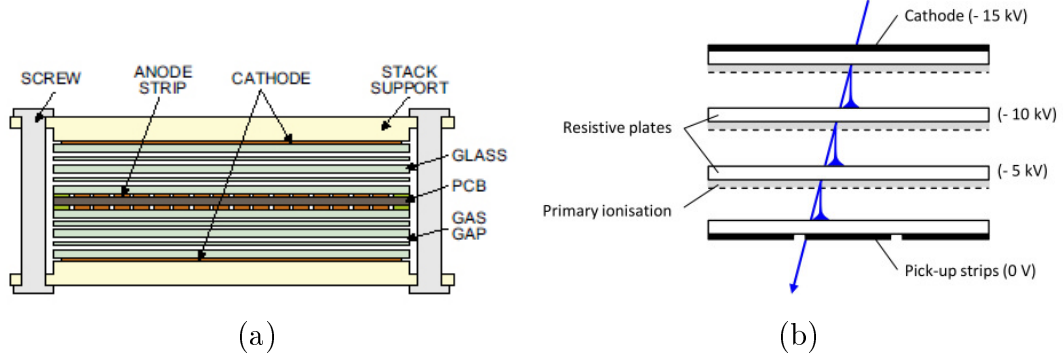


Figure 18: (a) Common double-stack configuration of a MMRPC counter with  $2 \times 4$  gas filled gaps between the glass plates, which are defined by spacers made out of fishing line. The anode strips are placed in the center of the counter and the stack is held together on both sides by nylon screws, which are also used as supports to span the spacer lines. The segmentation of the anode enhances the position resolution [Kis+11]. 5 of these counters are placed in a container to build one of the 30 Super Modules of the MMRPC TOF detector that surround the CDC. (b) Cross section of a multi-gap multi-strip RPC, which shows the evolution of an avalanche formation in the counter. In a single gap of the configuration only the primary ionization that takes place close to the resistive glass plates (region shown in grey) gives a detectable signal, which is depicted in blue. The avalanches finally induce signals on the anode strips. By dividing the gas volume into gaps, the timing resolution is improved as the primary ionization and avalanche growth area are shortened [Ple12].

before electron multiplication takes place. This behaviour leads to the better time resolution that is required to separate the kaons adequately. The design of a multi-gap multi-strip RPC is therefore an enhancement of multi-gap RPCs. The anode gets segmented into strips, what leads to an improvement of the position resolution. The outermost two strips are grounded in order to improve the uniformity of the field across the configuration [Kis+11] [Ber09].

With this configuration, the MMRPC can be operated at a voltage of about 10 kV producing an electric field of about 100 kV/cm that accelerates the charges. The active surface of a counter totals to  $4.6 \times 90 \text{ cm}^2$  [Sch+06]. A schematic view of the counters is given in figure 18.

### 3.3.3 Plastic Wall

In the forward direction, a TOF detector named Plastic Wall covers polar angles between  $7^\circ$  and  $30^\circ$  and full azimuthal angle. It consists of 8 radial sectors containing 64 scintillator strips each, what sums up to 512 strips in total. Depending on the polar angle, the length of the scintillators vary between 45 cm for angles on the lower acceptance boundary ( $7^\circ$ ) and 165 cm for the ones

on the upper boundary ( $30^\circ$ ). This corresponds to a time resolution of 80 ps to 120 ps and a position resolution of 1.2 cm to 2 cm, respectively. Due to the fast multiplicity information delivered for an event, the PLAWA fits perfectly for the purpose of serving as an online trigger (LVL1 described in section 3.7) [Ryu09]. Together with the start detector, a time resolution of about 400 ps is achieved [Ple12]. Figure 19 depicts the scheme of the TOF detector.

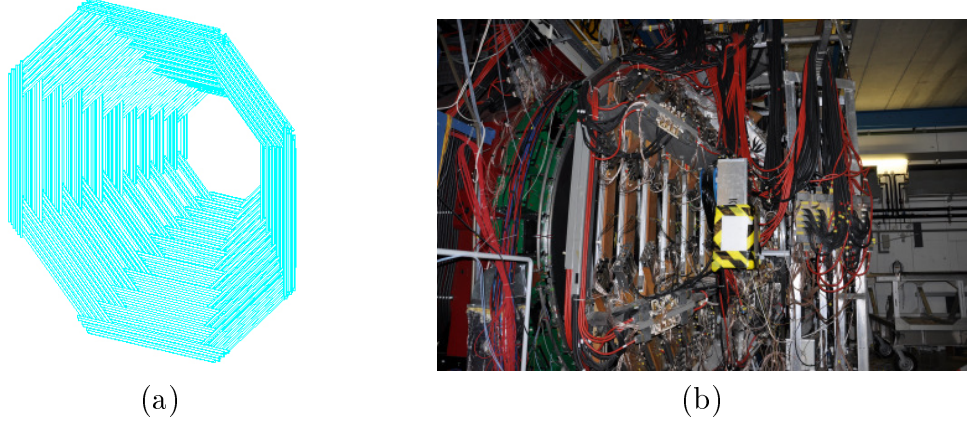


Figure 19: (a) Schematic view of the PLAWA TOF detector [Har03]. (b) Picture of the PLAWA in the experimental hall II of the acceleration facility at GSI, which was taken on the right side of the FOPI spectrometer with respect to the forward direction.

### 3.3.4 Zero Degree Counter

For particles that are emitted in small polar angles of  $1^\circ$  to  $7^\circ$ , the time-of-flight is measured with the ZDC, which is placed in the very forward direction of the FOPI spectrometer. It consists of 7 concentric rings arranged around the beam axis, which are build out of 36 trapezoidal scintillator strips each. They are only read out by photomultiplier tubes on the side that points away from the beam axis [Mer04] [Ryu09]. The time resolution of the ZDC varies between 230 ps and 340 ps. The ZDC also delivers a veto signal for the LVL1 trigger (for this purpose see section 3.7) [Ber09]. Figure 20 illustrates the scheme of the detector.

## 3.4 Beam Detectors

The S349 experiment with the proton beam required new hardware components that had not been integrated in the FOPI spectrometer so far. Therefore, the assembly of a suitable start counter, beam profile monitor (BPM), veto detector system and  $\Lambda$  trigger (described in section 3.6) was needed. These components

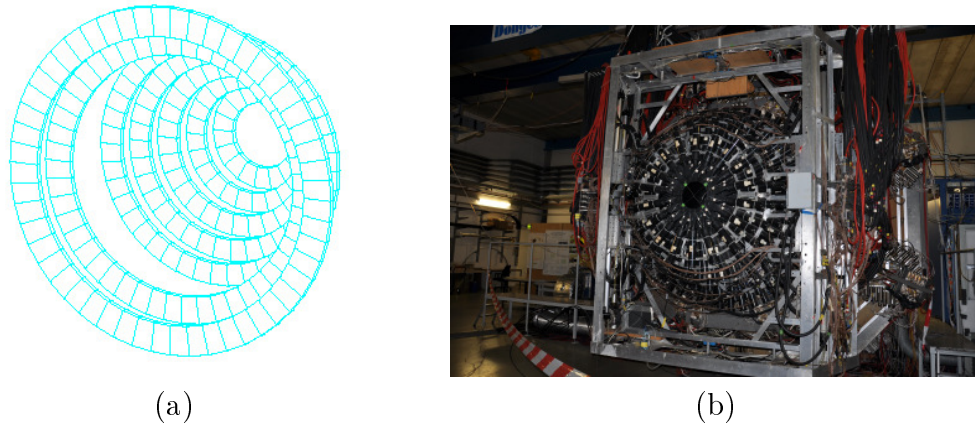


Figure 20: (a) Schematic picture of the ZDC TOF detector [Har03]. (b) Front view of the ZDC and the PLAWA readout photomultiplier tubes. The picture was taken in the experimental hall II of the acceleration facility at GSI, where the FOPI spectrometer is hosted.

were mounted such that the center of the target is located 40 cm upstream the nominal target position (which is shown in figure 16). Figure 21 shows the layout of the beam line that was achieved with these modifications to the FOPI set-up [BHS+09].

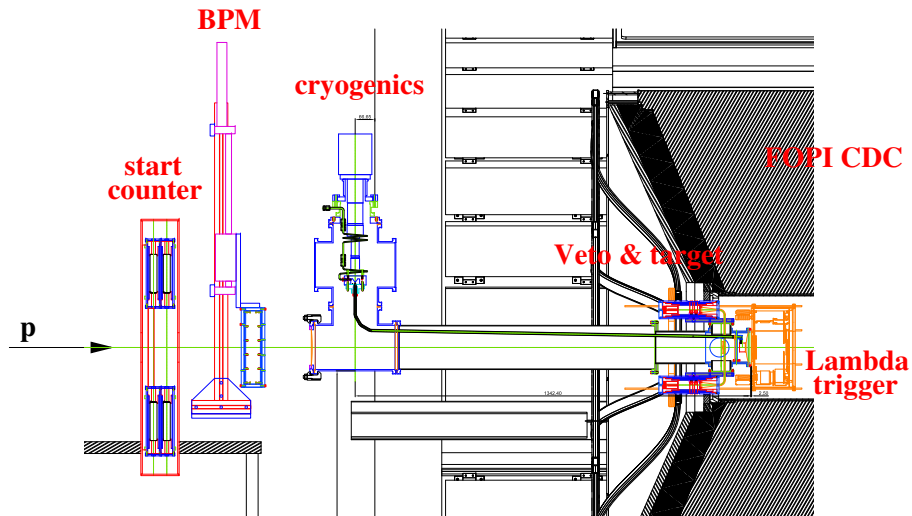


Figure 21: Schematic view of the beam line showing the positions of the beam detectors, the target system and the  $\Lambda$  trigger [BHS+09].

### 3.4.1 Start Counter

The start signal for time-of-flight measurement is delivered by a detector component in front of the target - the start counter, which is presented in figure

21 - whereas the stop signal is generated by the TOF detectors described in section 3.3 [Ber09].

In order to exploit the good timing resolution of the MMRPC for the time-of-flight measurement, a start detector with an equally good resolution was required. The ordinary FOPI equipment had become incapable of dealing with the high counting rates of approximately a few  $10^6$  counts per second, which are expected in a pp experiment [Ber09].

Consequently, a new start detector component was needed that provides sufficient timing resolution of about 100 ps. It consists of 5 vertically arranged scintillating segments, which are 1 cm thick and 2 mm wide. Each segment is read out on both sides with photomultiplier tubes, which are magnetically shielded to save their working efficiency as the field strength of the solenoidal field is about 60 mT at this position. The whole set-up achieves an intrinsic time resolution of  $\approx 130$  ps at a rate of up to  $2 \cdot 10^6$  counts per second [BHS+09].

### 3.4.2 Beam Profile Monitor

In addition to the start detector, the beam profile and position is monitored by another detector component - the beam profile monitor (BPM) presented in figure 21 - which is located directly behind the start detector and right in front of the veto detector and the target [Ber09].

The BPM is needed in order to deliver the proton beam with high precision onto the target. It consists of a grid of  $16 \times 16$  scintillating fibres, which are read out by silicon photomultiplier. The grid allows to determine the beam position in the x-y plane [BHS+09].

### 3.4.3 Veto Detector

To avoid that particles from interactions within the beam reach the detector systems of the FOPI spectrometer, a veto system is required between the start counter and the target. It delivers a veto signal for the data acquisition whenever charged particles pass off beam-axis [Ber09].

The veto detector consists of 2 segments of 5 mm thick scintillating layers, which are arranged cross-shaped with a hole in the center, where the beam passes through before it hits the target [Ber09]. This geometry limits the cross section of the target volume to a circle of 1 cm in diameter in the x-y plane. The layers are read out by fine-mesh photomultiplier tubes, which can be operated at the magnetic field strength of 0.6 T in this area. The veto efficiency achieved with this system is about 98% [BHS+09].

### 3.5 Target

A liquid hydrogen target ( $\text{LH}_2$ ) was placed right behind the veto detector. The system consists of a cryogenic cooler and a cylindrical target volume with 1.5 cm radius and width, respectively. The cooler was mounted outside the magnetic yoke for space reasons and the liquid hydrogen flows, driven by gravity, via a thin tube to the target volume. After 8 hours of cooling the target volume was completely filled [BHS+09].

### 3.6 Online Hardware $\Lambda$ Trigger SiAViO

In order to select events containing a  $\Lambda$ -Hyperon<sup>43</sup> on the hardware level, a new trigger was needed for the FOPI spectrometer. It basically enhances the number of events that are of interest in the acquired data and enables reconstruction of the secondary vertex, which results from the decay of the  $\Lambda$ -Hyperon [BHS+09].

For this reason, FOPI was upgraded with a silicon-based  $\Lambda$  trigger system called SiAViO (acronym for Silicon for  $\Lambda$ -Vertexing and Identification Online), which is presented in figure 22. As the name suggests, it is designed to enrich events containing  $\Lambda$ -Hyperon candidates. Furthermore, it provides additional position information, i.e. an additional hitpoint close to the target, for particles that are emitted in small polar angles. This is helpful and necessary for the task of secondary vertex reconstruction in the forward region, because of the low momentum resolution of the Helitron drift chamber [Fab09] [FCo07]. The problem of the limited tracking capability of the Helitron due to the large distance to the target area has already been discussed in section 3.2.2.

SiAViO is located inside the CDC and consists of two layers, A and B as indicated in figure 22, which are build of 1 mm thick silicon detectors. The layers are placed downstream the target at a distance of 3 cm (SiAViO A) and 15.5 cm (SiAViO B), respectively, such that about 60% of the  $\Lambda$ -Hyperons produced in the target decay between the two layers, as they are characterized by a mean decay length of about 7.9 cm [Mue+09].

SiAViO A is an annular single-sided silicon detector built of 32 slices, whereas SiAViO B consists of 8 rectangular double-sided silicon-strip detectors containing  $16 \times 60$  strips each such that it delivers position information by combining the signals of both sides, thus improving tracking [Fab09]. For this purpose, the p-side of the strips of layer B is read out by multiplexer chips, which are able to store the signal for about 4  $\mu\text{s}$  [Mue+09].

<sup>43</sup> The branching ratio of the  $\Lambda$ -channel of the  $ppK^-$  decay amounts to 50% (see equation 1.3), therefore it is helpful to have an additional trigger signal.

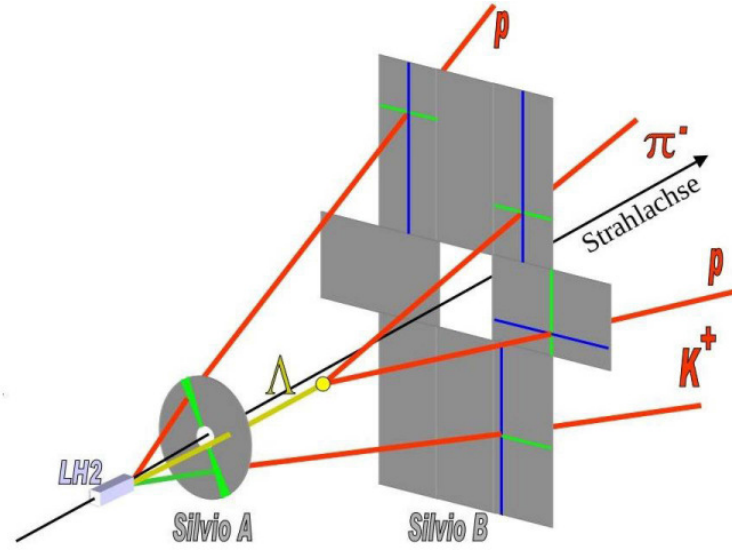


Figure 22: Schematic view of the silicon-based  $\Lambda$  trigger. A typical event  $\Lambda \rightarrow p + \pi^-$  is shown in between the two layers of the trigger system, where the blue and green lines indicate fired strips. The proton and kaon from the primary vertex of a decaying  $ppK^-$  are detected in layer A whereas the neutral  $\Lambda$ -Hyperon passes undetected and is reconstructed via its decay products that are recognized in layer B [Mue+09].

For the triggering task, the 32 sectors of layer A and the n-side of the strips of layer B are read out by analog readout modules, which are able to generate a trigger signal with a timing resolution of 150 ns [Mue+09]. About 64% of the  $\Lambda$ -Hyperons decay into  $p$  and  $\pi^-$ , therefore SiAViO B records a higher hit multiplicity than SiAViO A, what is set as the online event selection criteria. The hardware  $\Lambda$  trigger requires a hit multiplicity of 1 or more particles in SiAViO A in coincidence with 2 to 4 particles in SiAViO B (details given in the subsequent section 3.7) [Fab09].

### 3.7 FOPI Trigger System

Together with the start and veto detector, the time-of-flight detectors of the FOPI spectrometer are also used to generate a trigger signal (LVL1) in order to reduce the data acquisition (DAQ) rate and to filter out the events that are of interest. For this purpose, the fast signals of the TOF scintillators are discriminated and logically combined to a trigger condition named LVL1, which is listed in table 5 [Mer04].

Since the FOPI spectrometer has been developed for heavy-ion reactions, it is not capable of sufficiently reducing the amount of data that is taken in the pp experiment S349. As its DAQ rate amounts to only 600 Hz, mainly limited by dead times in the drift chambers CDC and Helitron, it was necessary to reduce

the DAQ rate by adequate trigger conditions. For that reason, the spectrometer was upgraded with the online hardware trigger SiAViO [Mue08].

As described in section 3.6, SiAViO delivers a trigger signal for events that contain a  $\Lambda$ -Hyperon, which is based on the multiplicity difference in the two detector layers A and B. This signal is combined with the ordinary FOPI trigger LVL1 to account for the trigger condition LVL2 [Ple12]. The three FOPI trigger conditions are listed in detail in table 5.

Trigger Name	Number of Hits	Detector
LVL1	$\geq 1$ $\geq 1$ $\geq 1$ $\leq 1$ 0	in Start Detector in PLAWA in MMRPC or Plastic Barrel in ZDC (as veto) in Veto Detector
SiAViO	$\geq 1$ $\geq 2$	in SiAViO A in SiAViO B
LVL2 = LVL1 AND SiAViO	$\geq 1$ $\geq 1$ $\geq 1$ $\leq 1$ 0 $\geq 1$ $\geq 2$	in Start Detector in PLAWA in MMRPC or Plastic Barrel in ZDC (as veto) in Veto Detector in SiAViO A in SiAViO B

Table 5: The FOPI Trigger Conditions.

In order to calculate the necessary reduction factor, which has to be applied to the interaction rate  $R_{pp}$  to fit the recording rate of the FOPI DAQ system of 600 Hz, the luminosity  $\mathcal{L}$  of the pp experiment has to be considered. It is defined as the proportionality factor between the cross section  $\sigma_{pp}$  and the number of interactions per second  $R_{pp}$  (interaction rate).

$$R_{pp} = \frac{dR}{dt} = \mathcal{L} \cdot \sigma_{pp} \quad (3.6)$$

The luminosity for a fixed target experiment is given by the equation

$$\mathcal{L} = \Phi \cdot n_{LH_2} \cdot l \quad (3.7)$$

with flux<sup>44</sup>  $\Phi$ , target density  $n_{LH_2}$  and target size  $l$ .

The  $LH_2$  target has a length  $l$  of 0.01 m and the flux  $\Phi$  amounts to  $5 \cdot 10^7$  protons per spill with a spill length of 10 s [Mue08]. The target density  $n_{LH_2}$  can be calculated with equation 3.8, where  $N_A$  denotes the Avogadro constant,  $\rho_{LH_2}$  the density and  $M_{mol,LH_2}$  the molar mass of hydrogen, respectively. To achieve the number of protons, the equation has to be multiplied by 2 as the  $H_2$  molecule consists of two atoms.

$$n_{LH_2} = \rho_{LH_2} \cdot \frac{N_A}{M_{mol,LH_2}} \cdot 2 = 70.8 \text{ [kg/m}^3] \cdot \frac{6.022 \cdot 10^{23} \text{ [1/mol]}}{2 \cdot 1.008 \cdot 10^{-3} \text{ [kg/mol]}} \cdot 2 = 4.26 \cdot 10^{28} \text{ [1/m}^3] \quad (3.8)$$

The total cross section  $\sigma_{pp}$  for pp reactions at a beam energy of 3.1 GeV is given with  $\sigma_{pp} = 44$  mb as listed in table 4. These numbers can finally be put into equation 3.7.

$$\mathcal{L} = \Phi \cdot n_{LH_2} \cdot l = 5 \cdot 10^6 \text{ [1/s]} \cdot 4.26 \cdot 10^{28} \text{ [1/m}^3] \cdot 0.01 \text{ [m]} = 2.13 \cdot 10^{33} \text{ [1/s} \cdot \text{m}^2] = 0.213 \text{ [1/s} \cdot \mu\text{b}]$$

After calculating the luminosity  $\mathcal{L}$  of  $0.213 \text{ s}^{-1} \mu\text{b}^{-1}$ , the reaction rate can be worked out by using equation 3.6.

$$R_{pp} = \mathcal{L} \cdot \sigma_{pp} = 0.213 \text{ [1/s} \cdot \mu\text{b}] \cdot 44 \cdot 10^3 \text{ [\mu b]} = 9.37 \text{ [kHz]}$$

Considering the FOPI DAQ rate of 600 Hz, the interaction rate has to be reduced by a factor of at least 15. This was planned to be achieved with the FOPI trigger system described earlier in this section.

---

<sup>44</sup> particles per second hitting the target:  $N/t$



## 4 Direct Particle Identification with FOPI

In order to identify the particles that are created in the pp collisions, the momentum and charge polarity of a detected particle are determined from the deviation of the particle trajectory in the magnetic field of the FOPI solenoid. Once the momentum has been derived, the particle mass, which is not directly measurable, can be figured out from other observables with two different methods that either involve the mean energy loss or the time of flight of a particle. They are described in the following sections. With these observables - momentum, charge and mass - charged particles can be identified [Mue08].

The momentum  $\vec{p}$  of a charged particle, which flies with velocity  $\vec{v}$  through the FOPI spectrometer, is determined with the drift chambers CDC and Helitron. Due to its charge  $q$ , it is deflected from its original flight path inside the magnetic field  $\vec{B}$  by the Lorentz force  $\vec{F}$ , which is given in equation 4.1. The induced electric field  $\vec{E}$  inside the drift chambers is aligned parallel to the magnetic field  $\vec{B}$ , whereas it vanishes outside the chambers [Ber09].

$$\vec{F} = m \cdot \vec{a} = q \cdot (\vec{E} + \vec{v} \times \vec{B}) \quad (4.1)$$

Equation 4.1 shows that the Lorentz force only acts on the particle if it has velocity components that are not parallel to the magnetic field because of  $\vec{v} \times \vec{B} = |\vec{v}||\vec{B}|\sin\vartheta$ . As described earlier in section 3.1, the FOPI magnet produces a homogeneous magnetic field, which is parallel to the beam axis  $z$  such that  $\vec{B} = (0, 0, B_z)^T$ . Hence, the particle track is bent circularly in the  $x$ - $y$  plane and therefore  $F = mv^2/r_c = pv/r_c$  for circular motion is fulfilled. The measured curvature radius of the trajectory,  $r_c$ , finally allows to determine the transverse momentum  $p_t$  of the particle and its charge  $q$ , respectively. The total momentum  $p$  of the particle can be derived from the polar angle  $\vartheta$ , which is also measured with the drift chambers, and the transverse momentum  $p_t$  as shown in the following equations [Ber09] [Mer04].

$$p_t = |q| \cdot |r_c| \cdot B_z \quad (4.2)$$

$$p = \frac{p_t}{\sin\vartheta} \quad (4.3)$$

As the Helitron drift chamber already falls into the inhomogeneous region of the magnetic field (see section 3.2.2), the previously described method is not appropriate for momentum reconstruction in this case. Instead, one applies an interpolation method that uses quintic B-splines in an iterative way [Ple12].

In addition to the momentum of the particle, other observables are needed to clearly identify particles within the FOPI spectrometer. Important in this context is to determine the particle mass and for this purpose FOPI offers two different possibilities provided that the momentum has already been extracted from the curvature of the particle trajectory. These methods are described hereafter.

Table 6 displays some of the relevant properties - mass  $m$ , mean life time  $\tau$ , mean decay length  $c \cdot \tau$  and the main decay channels with their branching ratios - of the particles that are involved in the FOPI pp experiment, namely the  $K^+$  meson, the  $\pi^-$  meson and the proton. The  $K^+$  and  $\pi^-$  mesons live long enough to travel through the sub-detectors of the FOPI spectrometer before they decay as their mean decay lengths are given with approximately 3.7 m and 7.8 m, respectively. Therefore, they can be directly identified with the methods of particle identification that are described below.

	m [MeV]	$\tau$ [s]	$c \cdot \tau$ [m]	main decay channels	BR [%]
$K^+$					
$u\bar{s}$	493.7	$1.2 \cdot 10^{-8}$	3.7	$\mu^+ + \nu_\mu$	63.6
				$\pi^+ + \pi^0$	20.7
				$\pi^+ + \pi^+ + \pi^-$	5.6
				$\pi^0 + e^+ + \nu_e$	5.1
				$\pi^0 + \mu^+ + \nu_\mu$	3.4
				$\pi^+ + \pi^0 + \pi^0$	1.8
$\pi^-$					
$d\bar{u}$	139.6	$2.6 \cdot 10^{-8}$	7.8	$\mu^- + \bar{\nu}_\mu$	99.9
p					
uud	938.3	$> 10^{39} - 10^{41}$	-	stable	

Table 6: Properties of particles that are of interest for the performed analysis [PDG].

## 4.1 Energy Loss

The first possible method to determine the rest mass of a charged particle is to measure the mean energy loss  $\langle dE/dx \rangle$ , which is sustained while the particle traverses through the drift chambers and ionizes the atoms or molecules of the detector gas, thus producing electrons that drift towards the sense wires of the chamber, where the field is strong enough to launch an avalanche. The mean energy loss of a particle trajectory is proportional to the charge that is collected

from all the hitpoints it consists of. It is, based on a quantum mechanical calculation, described by the Bethe-Bloch formula that links the mean energy loss and the momentum of the particle and is given in its relativistic form in equation 4.4. In this form the formula is only valid for “heavy”<sup>45</sup> particles and it stipulates a relation between the mean energy loss in the detector and the particle momentum  $p$  [Ben07] [Ber09] [Mue08].

$$-\left\langle \frac{dE}{dx} \right\rangle = 4\pi N_A r_e^2 m_e c^2 \rho \frac{Z}{A} \frac{z^2}{\beta^2} \left[ \frac{1}{2} \ln \left( \frac{2m_e c^2 \beta^2 \gamma^2 \Delta T_{max}}{I^2} \right) - \beta^2 - \frac{\delta}{2} - \frac{C}{Z} \right] \quad (4.4)$$

$N_A$  - Avogadro constant  
 $r_e$  - class. electron radius

$$r_e = \frac{e^2}{4\pi\epsilon_0 m_e c^2} \quad (4.5)$$

$m_e$  - electron mass  
 $c$  - speed of light  
 $\rho$  - density of absorber  
 $Z$  - atomic number of traversed medium  
 $A$  - mass number of traversed medium  
 $z$  - charge of incident particle  
 $\beta$  - velocity of incident particle:  $v/c$   
 $\gamma$  - Lorentz factor:  $1/(\sqrt{1-\beta^2})$   
 $\Delta T_{max}$  - maximum kinetic energy transfer to electron in single collision

$$\Delta T_{max} = \frac{2m_e c^2 \beta^2 \gamma^2}{1 + 2\gamma m_e/m_0 + (m_e/m_0)^2} \quad (4.6)$$

$I$  - mean ionization potential  $\approx 16 \cdot Z^{0.9}$  eV  
 $\delta$  - density correction factor for high energies  
 $C$  - shell correction factor for low energies  
 $e$  - electron charge  
 $\epsilon_0$  - vacuum permittivity  
 $m_0$  - mass of the incident particle

The energy loss described by the Bethe-Bloch equation mainly depends on the velocity of the particle and the absorber material, i.e  $Z/A$ , the density  $\rho$  and the ionization potential  $I$ . The  $1/\beta^2$ -term dominates for low particle energies, whereas the  $\ln \gamma$ -term dominates for high energies. Particles with

<sup>45</sup> I.e. for electrons and positrons modifications to equation 4.4 are necessary.

different mass have different  $\beta$  and  $\gamma$  (or velocity). This dependence enables particle identification, because the  $dE/dx$  curves as functions of the particle momentum are shifted for different masses. Hence, the energy loss depends on the particle mass and the mass  $m_0$  of the traversing particle can be calculated, once its momentum  $p$  has been determined from the curvature of the particle track in the magnetic field. The specific momentum interval, within which particle identification is possible with this information, depends on the detector resolution [Ber09]. Figure 23 and figure 24 depict how particle identification is done in the CDC with an energy loss measurement. After a particle has been identified as belonging to a certain particle species via the application of cuts on the mass range, its mass is set to its nominal value in order to calculate its energy  $E$  together with the measured momentum  $p$ , hence establishing the four-momentum  $p^\mu$  of the respective particle.

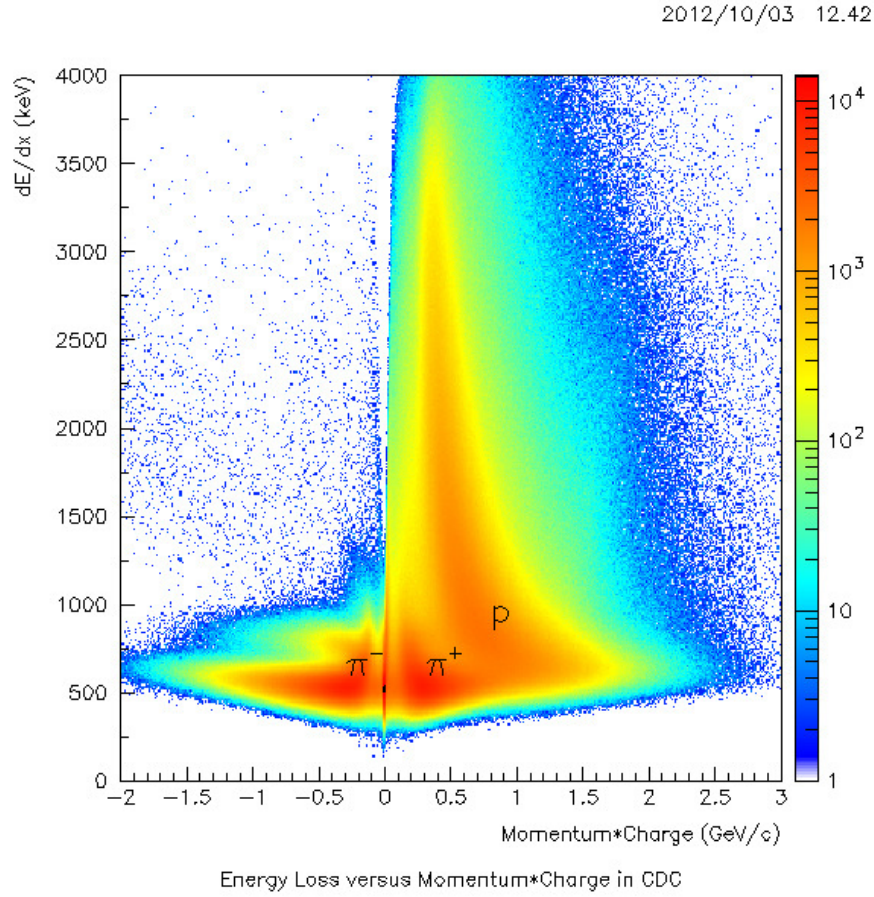


Figure 23: After measurement of the specific energy loss sustained by a charged particle while traversing through the CDC detector gas and its momentum, particle identification can be done. Parametrization of the Bethe-Bloch formula given in equation 4.4 with the known mass of a particle yields its expected position in the plot. Pions and protons can easily be distinguished.

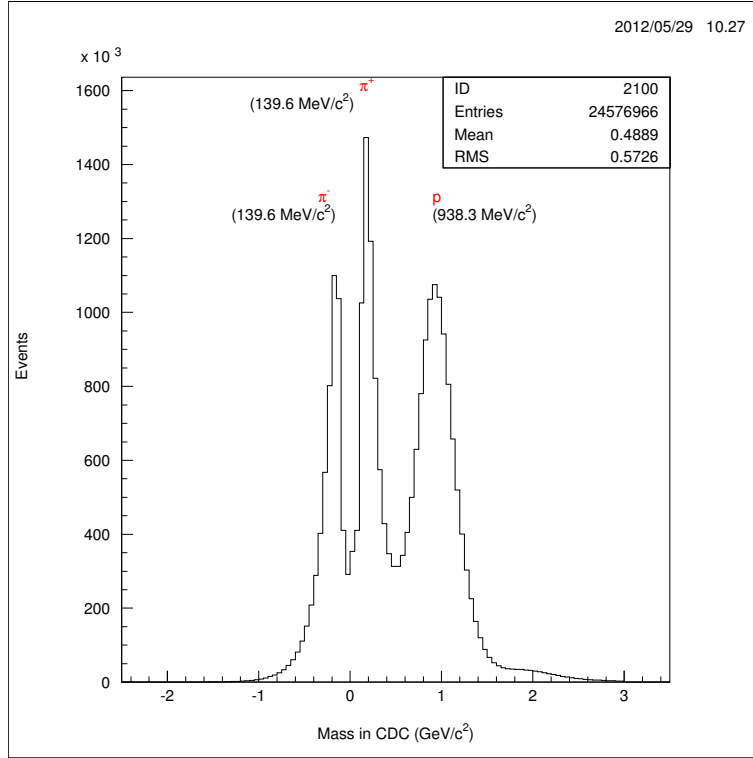


Figure 24: CDC mass (times charge) spectrum as derived from Bethe-Bloch parametrization. It allows to select a certain particle species by applying a cut on the mass range. Therefore, particles that have momentum and energy loss falling into these cuts are identified as a certain species.

## 4.2 Time of Flight

The other method to identify particles is to measure their time of flight  $\Delta t$ . This information is extracted from the TOF detectors, which are described in section 3.3, and the start counter, respectively, which is described in section 3.4.1. With the knowledge of the momentum  $p$ , the particle rest mass  $m_0$  can be derived with equation 4.8. The velocity  $v = \beta c$  can be derived from the length of the flight path  $L$  as follows in equation 4.7.

$$\beta c = \frac{L}{\Delta t} \quad (4.7)$$

$$p = m_0 \gamma \cdot \beta c \Rightarrow m_0 = \frac{p}{\beta c} \sqrt{1 - \beta^2} \quad (4.8)$$

Figure 25 and figure 26 depict how particle identification is done via the time of flight measurement in the different TOF detector components of the FOPI spectrometer that are suitable for his purpose. Particles emitted in the forward

direction (Helitron acceptance) are identified via the TOF information provided by the PLAWA detector whereas backward<sup>46</sup> emitted particles are identified via the MMRPC information if they fall into its acceptance<sup>47</sup>. As the momentum of these backward flying particles is still measured by the CDC, a good matching capability of the two detectors (MMRPC-CDC) is required.

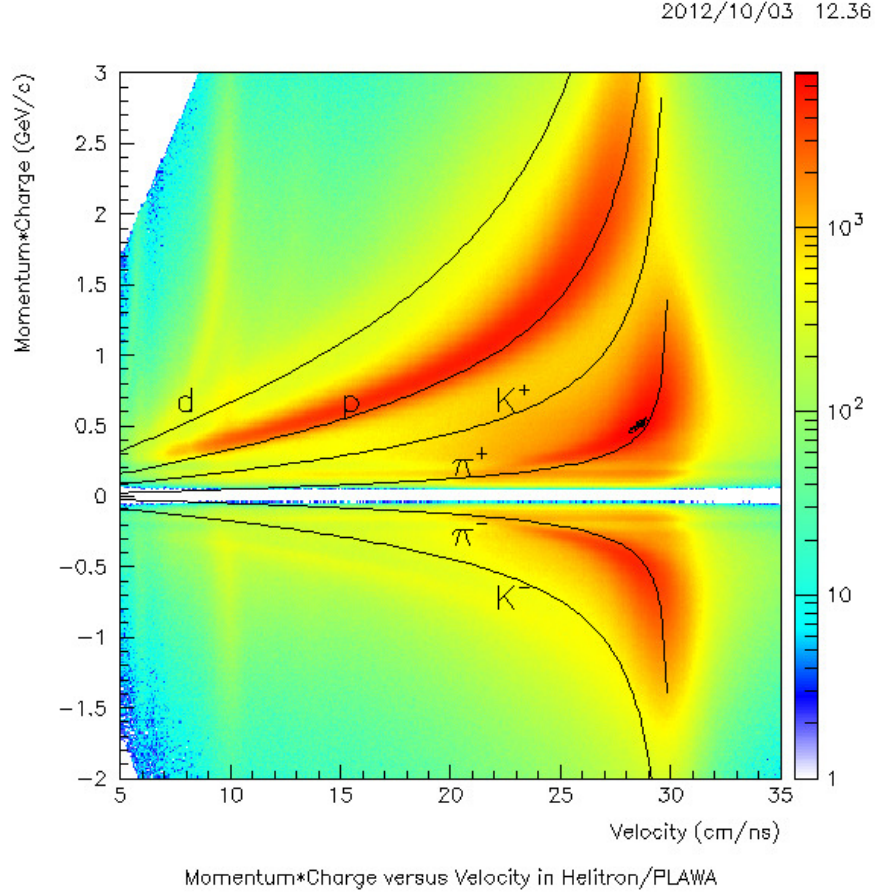


Figure 25: Momentum  $p$  (multiplied by charge  $q$ ) is plotted against the particle velocity  $v$  to identify particles via a time of flight measurement done with the PLAWA in forward direction. The black lines have been calculated with equation 4.8 and show the positions of the different particle species.

<sup>46</sup> with respect to the cms

<sup>47</sup> Otherwise they are identified via the energy loss information provided by the CDC as described in the previous section 4.1.

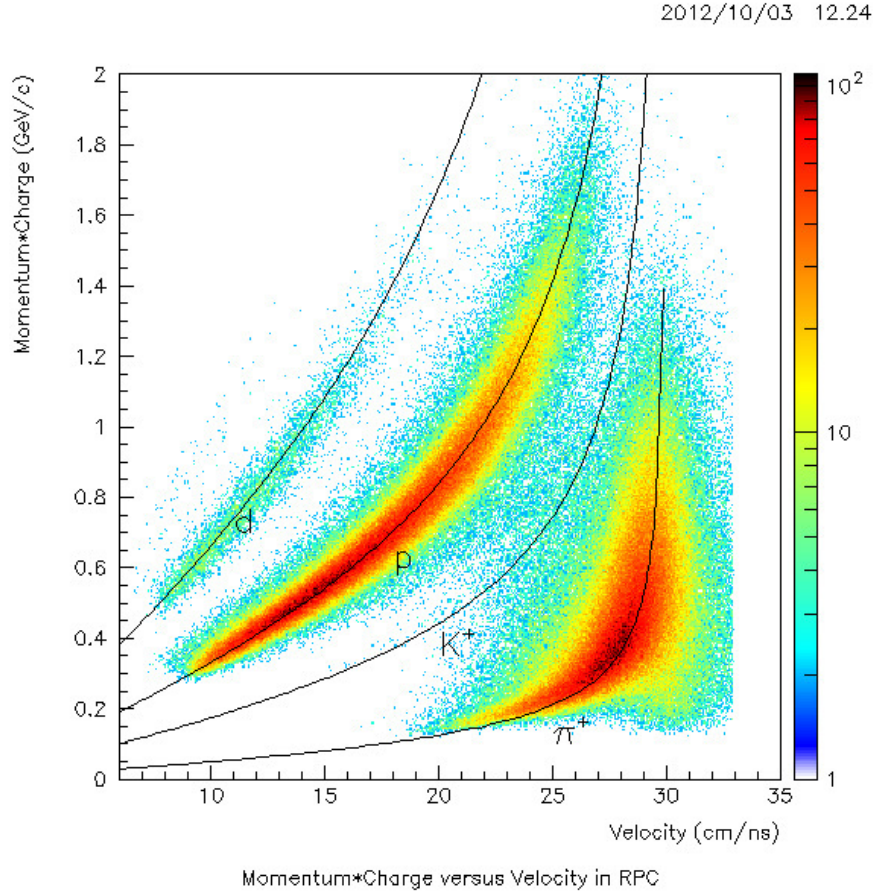


Figure 26: Momentum  $p$  (multiplied by charge  $q$ ) is plotted against the particle velocity  $v$  to identify particles via a time of flight measurement done with the MMRPC. The black lines have been calculated with equation 4.8 and show the positions of the different particle species. By comparing the plot with the one in figure 25, one can see that due to the better time resolution of the MMRPC TOF detectors kaons can be more clearly separated with the MMRPC than with the PLAWA. The task of kaon identification is of major importance to the pp experiment since it aims at reconstructing the  $ppK^-$  state, which is supposed to contain a  $K^+$  meson in the final state (see equation 1.3).

## 5 Data Analysis

Within this section, the analysis work that has been performed is explained and the results of this thesis are illustrated.

At first, the invariant and missing mass methods for the identification of short-lived particles like the neutral strange  $\Lambda$ -Hyperon are described. Further on, the vertex reconstruction techniques for the primary and secondary vertices, respectively, are explained. The quantities and criteria, which are used to select the secondary vertex, are discussed and depicted right afterwards. An important step constitutes the determination of the background spectrum with the event-mixing method and its subtraction from the invariant mass distribution of the  $\Lambda$ -Hyperon in order to get the quantities that are of interest (e.g. number of  $\Lambda$ -Hyperons). Finally the background corrected invariant mass spectra are presented for the reconstructed  $\Lambda$  candidates.

### 5.1 Invariant Mass and Missing Mass Technique

Since the short-lived  $\Lambda$ -Hyperon is a neutral particle, it is not possible to identify it directly with the methods described above in section 4. Depending on its life time, it decays immediately or with brief delay after its creation and does therefore usually not reach the FOPI sub-detectors.

Instead, the charged decay products of a decaying mother particle are detected and if all of them are measured and identified, a method called invariant mass technique can be applied in order to reconstruct the short-lived neutral mother particle [Sie10].

The invariant mass  $m_0$  of a particle is related to its energy  $E$  and the magnitude of its momentum  $|\vec{p}|$  by the relation given in equation 5.1, what follows from the energy-momentum relation  $E^2 - (\vec{p})^2 c^2 = m_0^2 c^4$  with four-momentum<sup>48</sup>  $p^\mu = m_0 v^\mu = (m_0 \gamma c, m_0 \gamma \vec{v})^T = (E/c, \vec{p})^T$  and the equivalence of mass and energy  $E = m_0 \gamma c^2$ .

$$m_0 = \frac{1}{c} \sqrt{p_{mother}^\mu p_{\mu, mother}} = \frac{1}{c^2} \sqrt{E^2 - (\vec{p})^2 c^2} \quad (5.1)$$

At the moment of decay, the decaying mother particle is at rest in the center of mass system (cms) of the decay products (daughter particles). Hence, the sum of the four-momenta of the daughters  $p_i^\mu$  is given by the mass of the mother, which is referred to as invariant mass. Provided that all decay products are

<sup>48</sup>  $p^\mu$  is a Lorentz invariant scalar and therefore independent of the reference frame in use.



detected, the mass of the mother particle can be reconstructed via this technique [Ple12].

Equation 5.2 shows the relation for the invariant mass  $m_{inv}$  of the decaying mother particle if the energy  $E_i$  and the three-momentum  $\vec{p}_i$  of all the  $n$  daughter particles are added up. As a function of the conserved quantities energy and momentum, the invariant mass itself represents also a conserved quantity.

$$m_{inv} = \frac{1}{c^2} \sqrt{\left(\sum_{i=1}^n E_i\right)^2 - \left(\sum_{i=1}^n \vec{p}_i\right)^2 c^2} \quad (5.2)$$

The mass of the mother particle can also be calculated by exploiting energy and momentum conservation. Given that the mother particle is produced together with  $n$  other particles, which have to be detected and identified in the sub-detectors of the FOPI spectrometer, the “missing” mass of the short-lived particle can be calculated with the formula given in equation 5.3.  $p_b^\mu = (E_b/c, \vec{p}_b)^T$  denotes the four-momentum of the beam particles and  $p_t^\mu = (E_t/c, \vec{p}_t)^T$  the four-momentum of the target particles, respectively [Sie10].

$$m_{miss} = \frac{1}{c^2} \sqrt{\left(E_b + E_t - \sum_{i=1}^n E_i\right)^2 - \left(\vec{p}_b + \vec{p}_t - \sum_{i=1}^n \vec{p}_i\right)^2 c^2} \quad (5.3)$$

Provided that energy and momentum conservation are fulfilled, both methods - missing mass and invariant mass - should yield the same mass for the decaying mother particle [Ple12].

Compared to prior experiments that have been searching for deeply bound kaonic states, an advantage of the FOPI pp experiment lies in the possibility of performing an exclusive measurement of the decay particles, a  $\Lambda$ -Hyperon and a proton, with an invariant-mass spectroscopy. This is enabled by the full solid angle coverage of the FOPI spectrometer, which allows to detect all daughter particles. In addition, the newly installed detector component Si $\Lambda$ ViO improves tracking for small polar angles in the Helitron acceptance region (see section 3.6). In the case of the  $ppK^-$  cluster, all decay products in the final state (see figure 11) - a proton from the  $ppK^-$  decay and another proton and a  $\pi^-$  meson from the intermediate  $\Lambda$ -Hyperon decay - are identified in the FOPI sub-detectors. Thus, information on the possible formation of a  $ppK^-$  cluster can be obtained from the invariant mass spectrum of the prior reconstructed  $\Lambda$ -Hyperon and a proton,  $M_{inv}(\Lambda p)$ . On the other hand, the missing mass distribution of the  $K^+$  meson yields the missing mass  $M_{miss}(K^+)$ , and therefore as well information on the  $ppK^-$  state as displayed in equation 1.1.

## 5.2 Tracking and Vertex Reconstruction

In order to get information on charged particles that have been created in pp collisions, their trajectories within the FOPI spectrometer have to be reconstructed.

For this purpose, the charges that are created by the primary ionization process and multiplied by the multiplication factor  $M$  (see equation 3.2) are collected on the signal wires of the drift chambers (see section 3.2) and their positions are determined (hit reconstruction). The  $z$  position along the signal wire is calculated with the charge division method, which uses the ratio of the charges that are collected on both ends of the wire. As already mentioned in section 3.2.1, the position resolution achieved in the  $x$ - $y$  plane is better than  $500\ \mu\text{m}$ , whereas the  $z$  position can only be determined with a precision of a few centimetres [Mer04].

If all hitpoints have been determined, the track finding routine starts to work. It consists of several algorithms (refer to the figures below) that implement a special tracking strategy, which is required because of the different position resolutions in the  $x$ - $y$  plane and  $z$  direction.

It first searches for hits that lie on an arc in the two-dimensional transverse plane. This arc reaches back to the target area, within which the primary vertex of an event is located. This process is illustrated in panel (b) of figure 27. The procedure varies the centres and radii of possible arcs in order to obtain the minimal deviation of the hits from a particle's trajectory. As a result, the arc finally represents the particle trajectory.

In a second step, the primary vertex is determined in an iterative routine, which interpolates back the reconstructed particle tracks to the target area in order to find the point that best fits all tracks to serve as primary vertex. Its accuracy reflects the position resolutions in the  $x$ - $y$  and  $r$ - $z$  planes. As the proton beam is focused in the  $x$ - $y$  plane, constraints on the  $z$  coordinate of the primary vertex position can be used to suppress background events, which do not originate from the target. Afterwards, the closest approach -  $dQ$  in the  $x$ - $y$  and  $z_0$  in the  $r$ - $z$  plane as illustrated in figure 27 - of each trajectory to the previously established primary vertex can be calculated (details given in section 5.3).

Finally, the  $z$  positions of the hits are used to derive the polar angle  $\vartheta$  of the particle trajectory that is displayed in panel (a) of figure 27. In this context, it is important to consider the limited precision capability of the drift chamber in the  $z$  direction, which may cause the deduced polar angle to be distorted on the  $z$ -axis. This problem can be fixed with a refit routine, which forces the primary vertex to be within the target region. Within this whole procedure, mirror tracks (already discussed in section 3.2) have to be excluded, what can

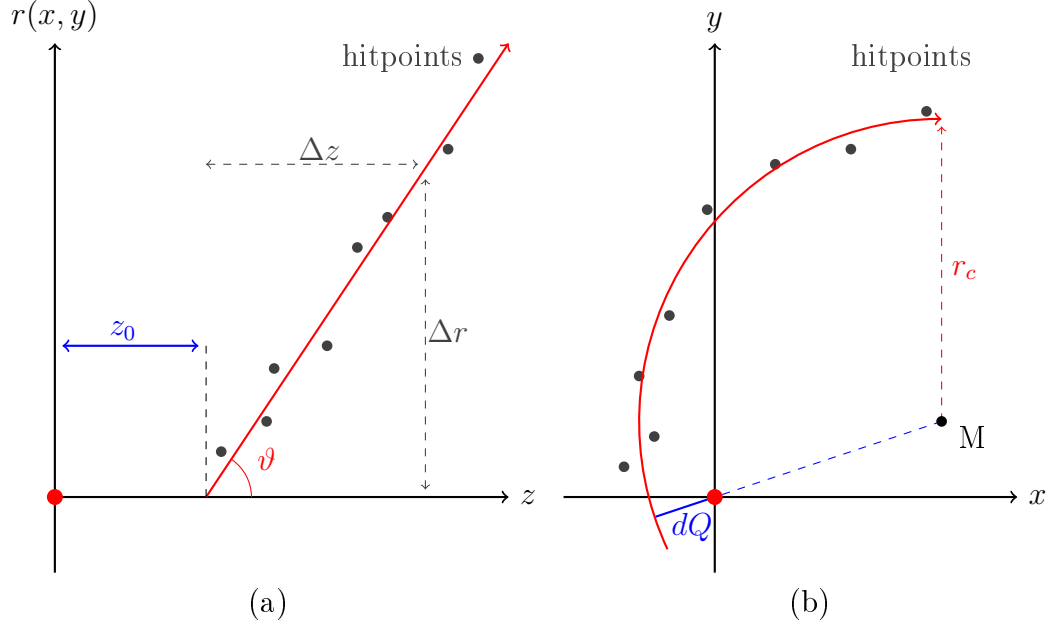


Figure 27: Determination of the shortest distance (or resolution of the detector) -  $z_0$  and  $dQ$  - to the primary vertex in the target area shown as red dot at the origin of the coordinate system (0,0). The procedure is illustrated in the beam direction  $z$  in (a) and in the transverse plane in (b) in approximation for a sector of a particle trajectory, respectively.  $dQ$  and  $z_0$  are used as vertex cut quantity for the reconstruction of the  $\Lambda$  decay (for explanation see section 5.3); their thresholds are given in table 8.  $r_c$  denotes the radius of curvature for the reconstructed particle trajectory, which occurs under the influence of the magnetic field. Illustrations taken from [Mer04] and [Ben07], but modifications applied.

easily be done with the geometrical features (staggering; tilted anode plane), which have been integrated in the design of the FOPI drift chambers [Mer04] [Ryu09].

After fitting the track curve, the track parameters drift velocity  $v_D$ , Lorentz angle<sup>49</sup>  $\alpha_L$  and total time offset  $t_0$ , which is used to calculate the drift time  $t_D$ , are calibrated such that after iterative application of hit reconstruction, tracking and adjustment of these parameters, no track discontinuities are left over [Mer04].

<sup>49</sup> The Lorentz angle, or drift angle  $\alpha_L$ , is the angle by which particles moving inside an electric field are deflected under the influence of a magnetic field. It is therefore the angle between the drift direction of charge carriers influenced by deflection and the direction of electric field. It depends on the gas mixture, the pressure and the electric and magnetic field inside the drift chamber [Mer04].

### 5.2.1 Secondary Vertex Reconstruction of the $\Lambda$ Decay

As already discussed, neutral short-lived particles like the  $\Lambda$ -Hyperon can not be directly identified by combining CDC with Plastic Barrel/MMRPC or Helitron with PLAWA information, as described in section 4. The method of direct PID can be applied for example in the case of  $K^+$  mesons or protons, but neutral short-lived particles have to be reconstructed from their charged decay products, which are directly identified.

Hence, the  $\Lambda$ -Hyperons decay at some distance to the primary vertex in the target area, producing a so-called secondary vertex that is searched for by combing all possible decay daughters in an event. In particular, all protons in an event, which have been identified via the measurement of their specific energy loss as given by the Bethe-Bloch formula in equation 4.4 and their momenta, are combined with all (in the same way identified)  $\pi^-$  mesons in order to identify their mother particle, the  $\Lambda$ -Hyperon, with the invariant mass method that is explained in section 5.1.

As a result, this procedure yields the invariant mass distribution  $M_{inv,\Lambda}(p\pi^-)$  of the  $\Lambda$ -Hyperon. From the obtained spectrum, all background events have to be subtracted. Section 5.4 describes how the background is modelled.

The properties - mass  $m$ , mean life time  $\tau$  and mean decay length  $c \cdot \tau$  - of the weakly decaying strange  $\Lambda$ -Hyperon, as illustrated in figure 28, and its decay channels with their branching ratios, respectively, are listed in table 7. As the name suggests, the mean decay length serves as an estimate of the distance between the primary vertex, where the  $\Lambda$ -Hyperon is created, and the secondary vertex, where it decays.

$\Lambda^0$	m [GeV]	$\tau$ [s]	$c \cdot \tau$ [cm]	decay channel	BR [%]
uds	1.116	$2.6 \cdot 10^{-10}$	7.89	$p + \pi^-$	63.9
				$n + \pi^0$	35.8
				$n + \gamma$	$1.8 \cdot 10^{-3}$
				$p + \pi^- + \gamma$	$8.4 \cdot 10^{-4}$
				$p + e^- + \bar{\nu}_e$	$8.3 \cdot 10^{-4}$
				$p + \mu^- + \bar{\nu}_\mu$	$1.6 \cdot 10^{-4}$

Table 7: Properties of the  $\Lambda$ -Hyperon [PDG].

The first step in the  $\Lambda$  reconstruction process is, to select all of the decay products of a certain decay channel. The FOPI spectrometer can only identify charged particles, therefore channels that contain neutral daughters are not available. Nevertheless, the main decay mode  $\Lambda \rightarrow \pi^- + p$  with a branching

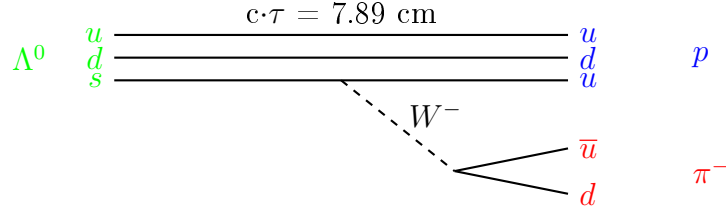


Figure 28: Schematic illustration of the decay of the  $\Lambda$ -Hyperon into its main decay mode  $\pi^- + p$  with a branching ratio of 63.9% at a time scale of  $10^{-10}$  s. Illustration taken from [Mer04], but modified.

ratio of approximately 64% can be fully exploited and therefore the analysis focuses on this channel.

From the CDC (matched with the MMRPC) information that is provided for each trajectory, the number of hits on a track (hit multiplicity), the particle mass  $m$ , the curvature radius  $r_c$  and the shortest distance to the primary vertex in the transverse plane  $dQ$  are used. The quantities  $r_c$  and  $dQ$  are illustrated in figure 27. The curvature is, as already mentioned, a measure for the transverse momentum  $p_t$  of a particle. The connection between these variables is given in equation 4.2. The hit multiplicity specifies how many hitpoints belong to a certain trajectory. The particle mass is derived with the methods described in section 4. A certain particle species can be selected by applying cuts on the mass range, what is depicted in panel (b) of figure 23. The shortest distance to the primary vertex is calculated after the particle track has been reconstructed and represents the distance of each trajectory to this vertex in the transverse direction. In order to select particles that originate from a secondary vertex, a lower threshold is used for this distance.

Further on in the reconstruction process of the  $\Lambda$ -Hyperon, the selected  $\pi^-$  meson and proton track pairs are intersected in the transverse plane, as displayed in figure 29. For this purpose, the arcs that represent the particle trajectories are extended to a circle and the distance  $d_{21}$  between the two centres,  $M_1$  and  $M_2$ , of these circles is calculated and compared to the sum of the two curvature radii  $r_{c,1}$  and  $r_{c,2}$ . If the distance  $d_{21}$  is larger than the sum of the radii, no intersection point of the two circles exists. In this case, the combination possibility is discarded. In every other case, where  $d_{21} > r_{c,1} + r_{c,2}$ , two intersection points are found, which represent the possible positions of the secondary vertex of the  $\Lambda$  decay. The case, in which the two quantities are exactly the same, yields only one intersection point and has no practical relevance. Finally, the angle  $\alpha$ , which is the angle between the two intersections points with respect to the centre of the circle and also illustrated in figure 29, is determined. The geometrical reconstruction is completed by calculating the coordinates of the secondary vertex positions in the x-y plane.

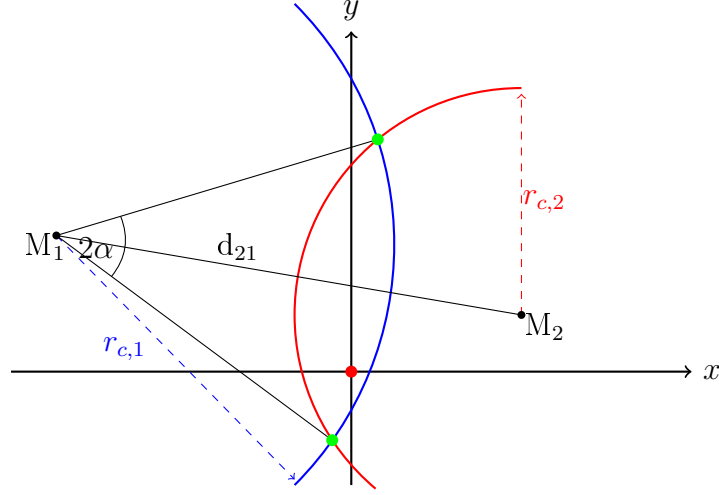


Figure 29: Determination of the secondary vertex of the  $\Lambda$ -Hyperon decay into  $\pi^- + p$ . The thick blue and red curves indicate parts of the trajectories of the daughter particles  $\pi^-$  and  $p$ . The red dot at the origin of the coordinate system symbolizes the primary vertex in the target area, the black dots the centres of the circles that indicate the track of the daughters, respectively, and the green dots the possible positions of the secondary vertex, which are obtained by intersecting the two trajectories. Details about the geometrical reconstruction of the secondary vertex position are given in the text. Illustration taken from [Mer04] and [Ben07], but modifications applied to it.

In the next step, the momentum and the invariant mass of the  $\Lambda$ -Hyperon are calculated for each intersection point with the information that is obtained from the involved pair of combined decay products. This is, of course, only performed if intersection points exist and the properties that are involved are displayed in figure 30. The correct secondary vertex position is finally determined by applying thresholds for certain cut quantities, which are explained in section 5.3. Above all, intersection points are rejected if they are located far from the primary vertex or if the reconstructed  $\Lambda$  tracks do not point back to the primary vertex.

For the determination of the transverse distance  $dr$  between the secondary vertex candidate and the primary vertex, the transverse coordinates of the vertex candidate are used. Furthermore, the azimuthal angle  $\varphi$  and the longitudinal positions  $z_1$  and  $z_2$  of the two particle trajectories at the radial distance of the secondary vertex candidates are calculated. The polar angle  $\vartheta$  has already been determined for each track during the application of the track finding routine.

With the polar angle  $\vartheta$ , the azimuthal angle  $\varphi$  and the curvature  $r_c$ , the four-momenta  $p^\mu$  of the daughter particles at the position of the secondary vertex are computed. Then the transverse momentum  $p_t$  and total momentum  $p$  of the  $\Lambda$  candidate, as given equation 4.2 and equation 4.3, are calculated and

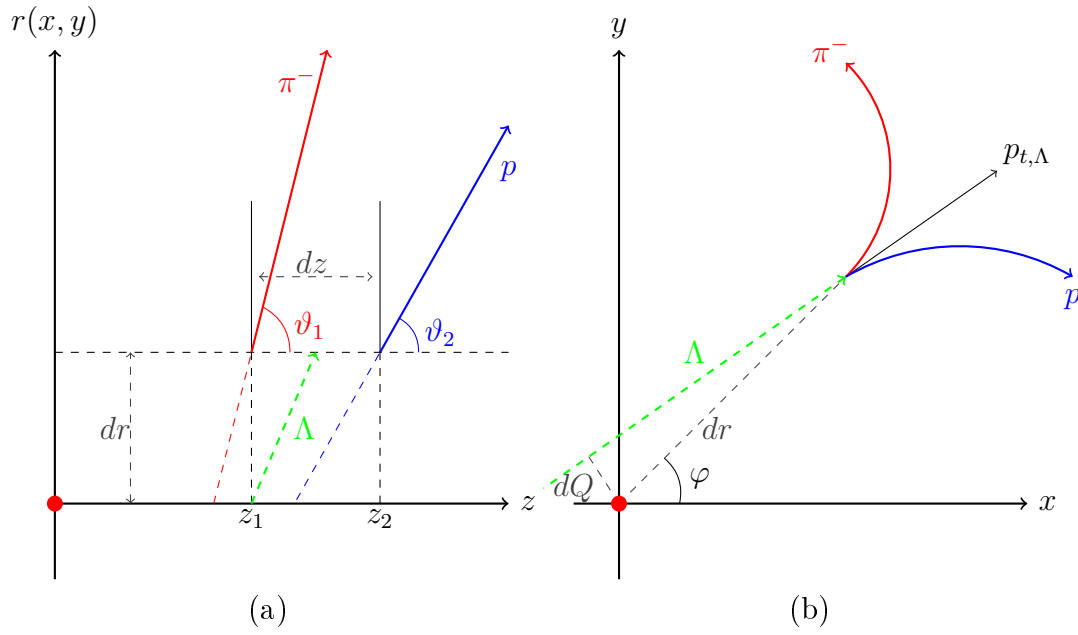


Figure 30: Schematic view of the reconstruction method of strange particles in the CDC sub-detector of the FOPI spectrometer. The decay of a  $\Lambda$ -Hyperon, which is shown as a dashed green line, is displayed for the  $r$ - $z$  plane in (a) and for the transverse plane  $x$ - $y$  in (b). The thick red and blue lines in (a) or curves in (b) indicate parts of the trajectories of the daughter particles  $\pi^-$  and  $p$ , respectively. The cut quantities that are applied for the selection of the  $\Lambda$ -candidates -  $dQ$  and  $dr$  - are illustrated in gray and explained in the text. The red dot at the origin of the coordinate systems symbolizes the primary vertex, which is located in the target area. Illustration taken from [Mer04] and [Ben07], but modified.

subsequently used to obtain its azimuthal angle  $\varphi$  and polar angle  $\vartheta$ , respectively.

In this context, further cut quantities, for example the shortest distances to the primary vertex in the transverse -  $dQ$  - and longitudinal direction -  $z_0$  - of each track, are determined. Moreover, the momentum resolution of the  $\Lambda$ -Hyperon can be enhanced by applying refitting techniques for the daughter tracks at the position of the secondary vertex (refer to section 6.2) [Mer04].

Finally, the invariant mass of the  $\Lambda$  candidate is derived with the invariant mass technique described in section 5.1 using equation 5.2. The results are displayed and discussed in section 5.5.

### 5.3 Vertex Cuts

After the reconstruction of the particle tracks and the primary and secondary vertex has been established, so-called vertex cuts are applied in order to discard secondary vertices that are the result of combined  $\pi^-$  and  $p$  pairs, which do not originate from a  $\Lambda$ -Hyperon decay. This is necessary, because the analysis is based on the combination of all protons with all  $\pi^-$  mesons of an event, thus producing many fake  $\Lambda$  candidates that have to be rejected.

In the case of a fake secondary vertex, the reconstructed particle track of the  $\Lambda$  candidate does not point back to the primary vertex, where it is expected to originate from. As a consequence, the reconstructed daughter particle tracks do not point far enough away from the primary vertex, what they are supposed to if they originate from a proper secondary vertex candidate.

Moreover, secondary vertex candidates that are located too far away from the primary vertex are eliminated. In this context, the mean decay length of the  $\Lambda$ -Hyperon, which is given with approximately 7.89 cm, is taken as an estimate, although it has exponential length distribution.

Those pairs of combined daughter particles that nevertheless pass the vertex cuts, although not being correlated by a  $\Lambda$  decay, leave over a combinatorial background, which has to be modelled and subtracted thereafter from the reconstructed invariant mass spectrum of the  $\Lambda$ -Hyperon in order to extract its mass and the number of  $\Lambda$  that are contained in the spectrum. The methods that are used to derive the background corrected mass distribution are explained in section 5.4.

Table 8 displays the quantities that have been used as vertex cuts, most of which are illustrated in figure 30 or in figure 31, respectively.

First of all, cuts on the number of particles that participate in an event are



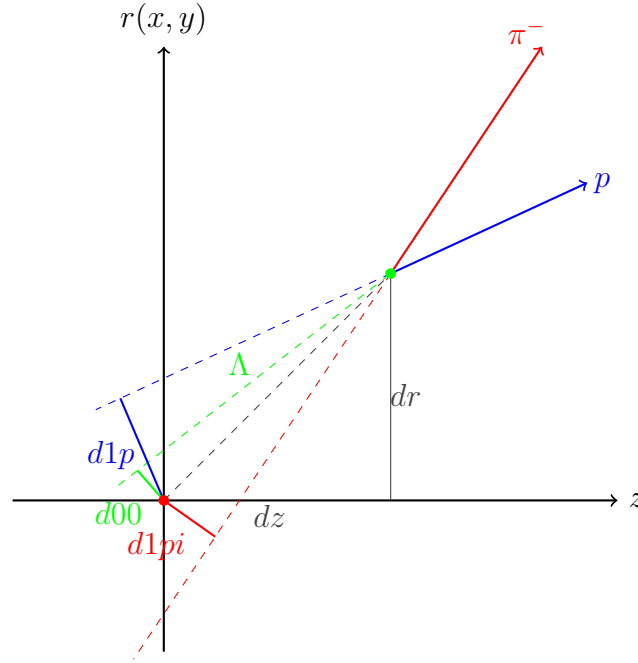


Figure 31: Schematic view in the  $r$ - $z$  plane of the geometrical vertex cut quantities that have been applied in order to reconstruct the decaying  $\Lambda$ -Hyperon, which is shown as green dashed line. The daughter particles  $\pi^-$  and  $p$  are displayed as red and blue lines, respectively. The red dot at the origin of the coordinate system symbolizes the primary vertex in the target area, whereas the green dot symbolizes the secondary vertex position of the  $\Lambda$  decay. The vertex cut quantities - shortest distances to the primary vertex of the  $\pi^-$  meson ( $d1\pi$  - red line), proton ( $d1p$  - blue line) and  $\Lambda$ -Hyperon ( $d00$  - green line), respectively, and the distance of primary to secondary vertex  $dr$  - are explained in the text and the thresholds are given in table 8. Illustration taken from [Mer04], but modifications applied to it.

cut quantity	threshold
no. of p	$\geq 2$
no. of $\pi^-$	$\geq 1$
dQ [cm]	$< 2$
d00 [cm]	$< 1.2$
d1p [cm]	$> 0.3$
dr [cm]	$0.3 < \dots < 30.5$
$p_{t,p}$ [GeV/c]	$0.3 < \dots < 1.8$
multiplicity CDC+PLAWA	$2 \leq \dots \leq 4$

Table 8: Used vertex cut quantities, given with their thresholds. They have been used for the analysis.

defined. As the signature of a  $p + p \rightarrow ppK^- + K^+$  event contains in about 32% of all decay scenarios two protons, a  $\pi^-$  and a  $K^+$  meson in its final state (see equation 1.3), one asks for at least two protons and one  $\pi^-$  meson in an event. These are the requirements in the case that an inclusive event analysis is performed (see section 5.5), which focuses only on the reconstruction of the decaying mother particle, namely the  $\Lambda$ -Hyperon. If a semi-inclusive event analysis is carried out, the identification of a  $K^+$  meson is required in addition. Finally, the exclusive event analysis demands for exactly four particles in the final state: two protons, a  $\pi^-$  and a  $K^+$  meson, respectively.

Two cuts on the reconstructed  $\Lambda$  flight path, which is illustrated as green dashed line in panel (b) of figure 30 and in figure 31, respectively, assure that the reconstructed  $\Lambda$  candidate originates from the primary vertex, which has been determined for each event. Thus, the previously calculated closest distance of the trajectory to the primary vertex in the transverse plane ( $dQ$  - see figure 30) and in the longitudinal direction  $z$  ( $z_0$ : in this context denominated as  $d00$  for the  $\Lambda$ -Hyperon - see figure 31) has to fulfil certain constraints. These quantities reflect the resolution of the detector, which is quite limited in the  $r$ - $z$  plane in comparison to the resolution that is achieved in the transverse plane  $x$ - $y$ . This has already been discussed above in connection with figure 27, which introduced the concept of the closest approach of a track to the primary vertex.

In the same way, cuts on the closest approaches to the primary vertex of the proton and  $\pi^-$  meson tracks are applied in the  $r$ - $z$  plane. These quantities are depicted and labelled in figure 31 as  $d1p$  (blue) for the reconstructed proton and  $d1pi$  (red) for the reconstructed  $\pi^-$  flight path, respectively. In contrast to the threshold on the closest approach  $d00$  of their mother particle ( $\Lambda$ ), which is given as an upper limit, the threshold on  $d1p$  is set as a lower boundary to achieve the opposite result. The origin of the daughters is of course fixed with the secondary vertex, thus offering the reconstruction possibility of the

mother and therefore they must not point back to the primary vertex as they do not originate from it. Such a constraint is put on the proton track, because in an event, which contains a  $ppK^-$  decay, a second proton originates directly from the primary vertex and therefore combinations of  $\pi^-$  mesons with this proton must be rejected. Consequently, there exists no such directly produced  $\pi^-$  meson in that case (see equation 1.3), thus an identified  $\pi^-$  in the sub-detectors may only origin from a secondary vertex and a threshold is per se not needed for its closest distance to the primary vertex.

In addition, a lower and upper limit is set for the transverse distance  $dr$  between the reconstructed primary and secondary vertices in order to reduce the background that results from primary particles<sup>50</sup> and to discard secondary vertices that are located too far away from the primary vertex, respectively. In this context, the mean decay length ( $c \cdot \tau$ ) of the  $\Lambda$ -Hyperon (7.89 cm, listed in table 7) serves as an estimate for the upper threshold of this quantity, which is determined by approximately  $4 \cdot 7.89$  cm.

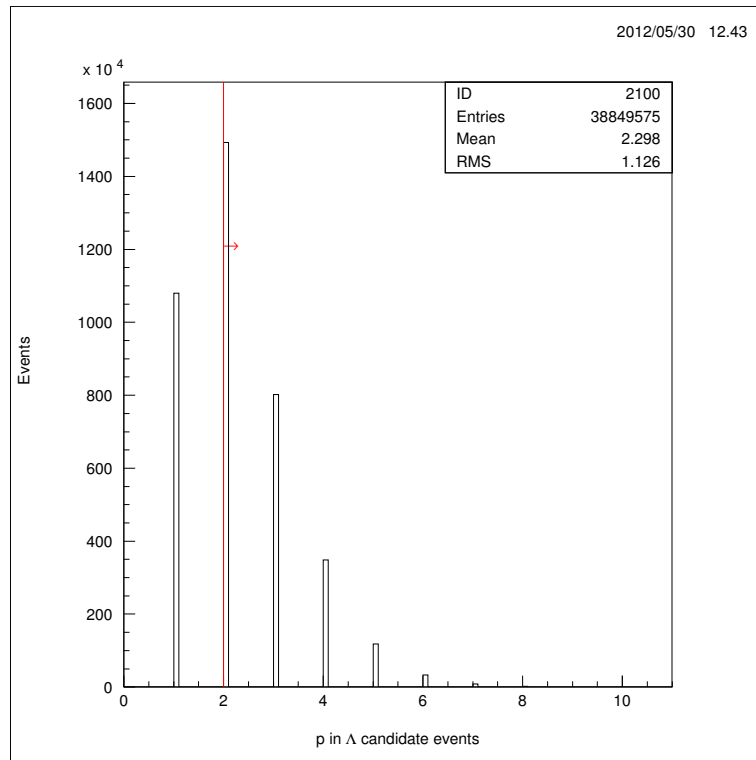
Another constraint on a proton quantity is defined by a lower and upper boundary on its transverse momentum  $p_{t,p}$  to exclude protons, which are either too slow<sup>51</sup> and therefore not suited to be the product of a possible  $ppK^-$  decay, or too fast to be identified with the CDC in combination with the MMRPC information.

Finally, the multiplicity condition is set as the sum of the multiplicities that are measured by the CDC and PLAWA sub-detectors, respectively. A total of two (minimum a pair of daughter particles to be reconstructed) to four tracks (maximum number of particles in the final state) may be detected in the FOPI spectrometer. In combination with the constraints on the number of the proton (min. 2) and the  $\pi^-$  meson (min. 1) in an event, this threshold reduces the combinatorial background and selects so-called four-prong events, which contain a maximum of four particles in the final state. This corresponds to the characteristics of the hypothetical  $ppK^-$  production and decay that the FOPI pp experiment searches for. Nevertheless, the specifications of the fourth particle - which is supposed to be a  $K^+$  meson - are completely left open at this stage of the analysis, as neither charge nor mass constraints are applied on it.

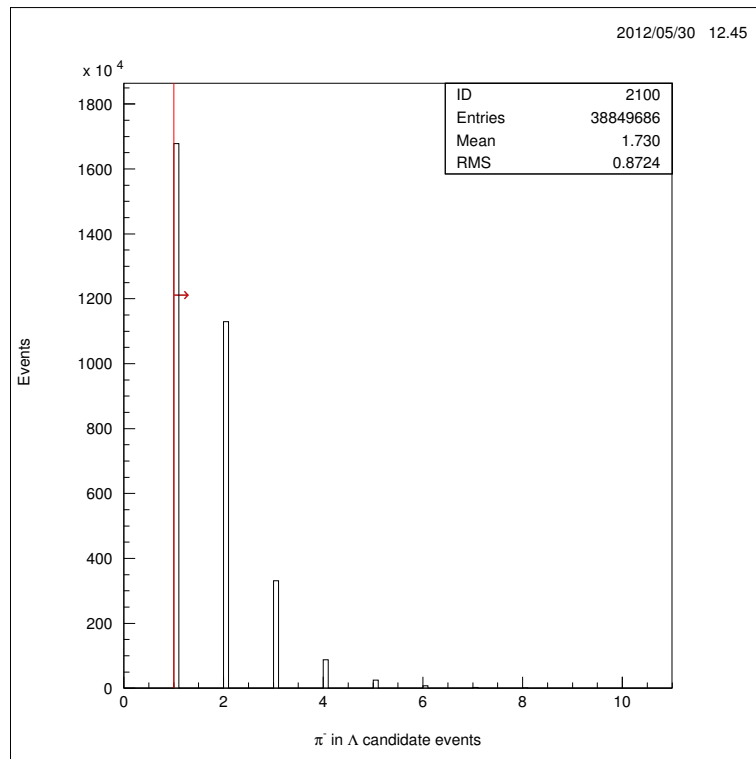
Figure 32 depicts the spectra of the various cut quantities, which have been explained above. The red lines together with the red arrows illustrate the thresholds that have been applied on the distributions.

<sup>50</sup> A particle that originates from the primary vertex.

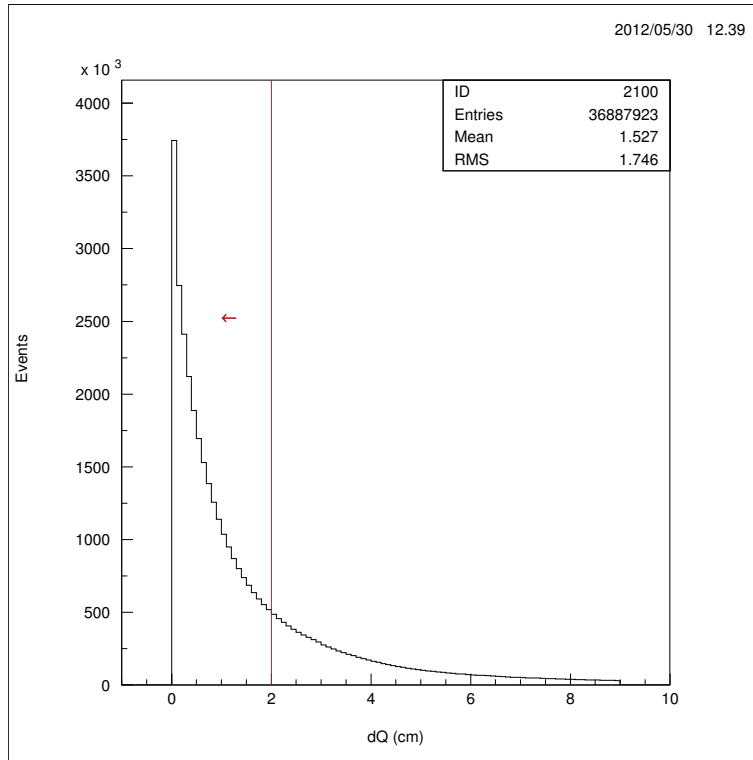
<sup>51</sup> The decay daughters of a possible  $ppK^-$  cluster, i.e. the  $\Lambda$ -Hyperon and therefore the considered proton too, are supposed to be forward boosted.



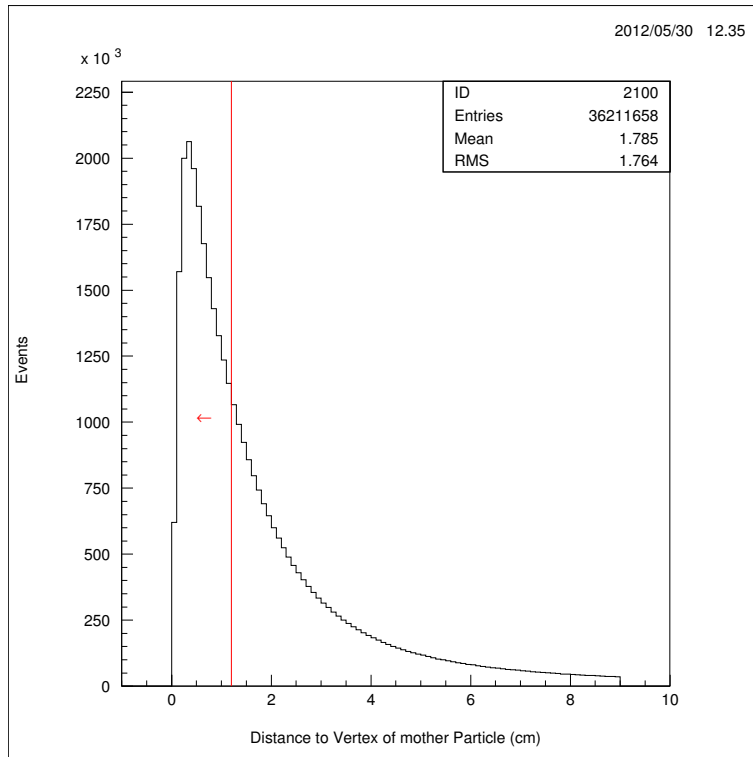
(a)



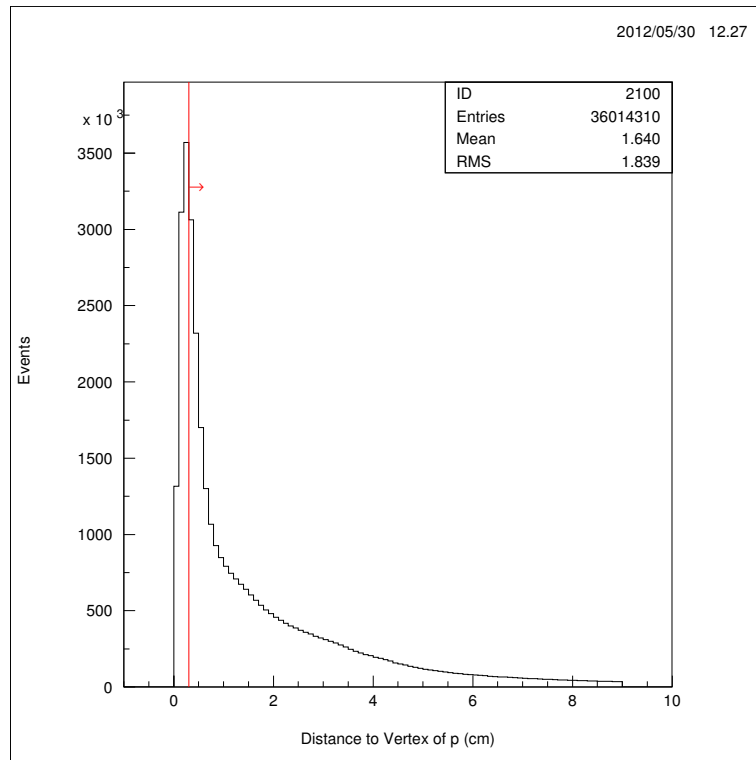
(b)



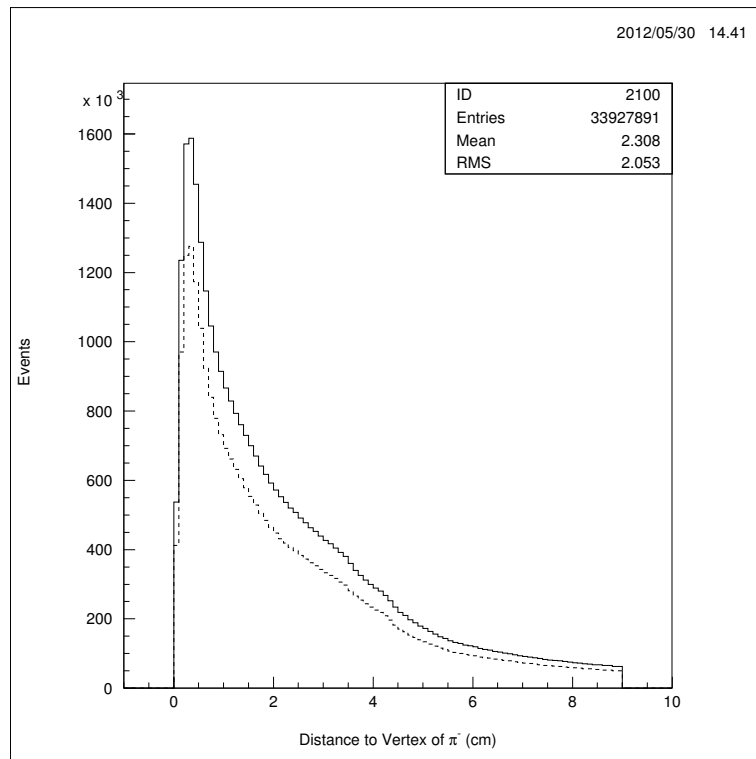
(c)



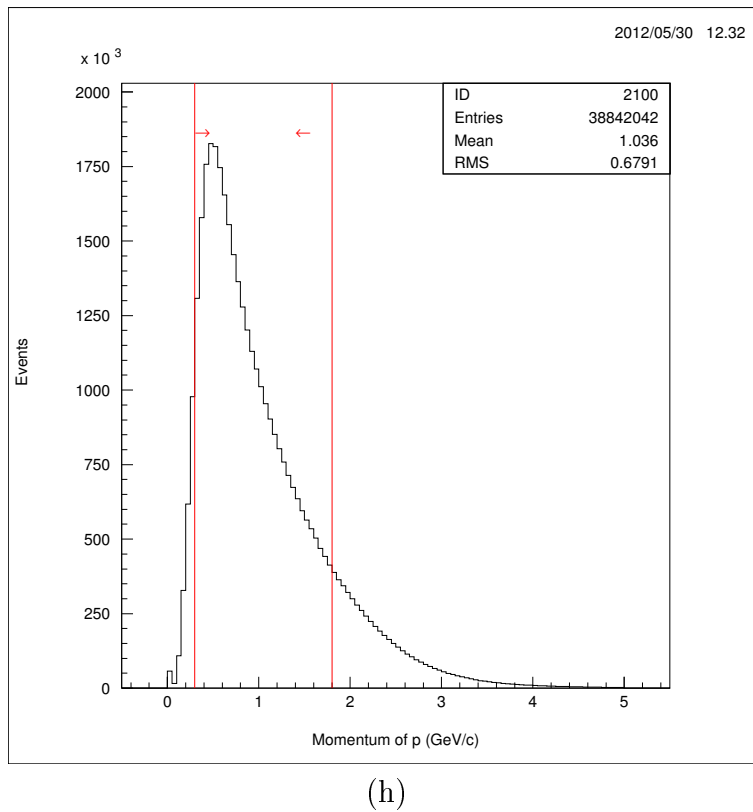
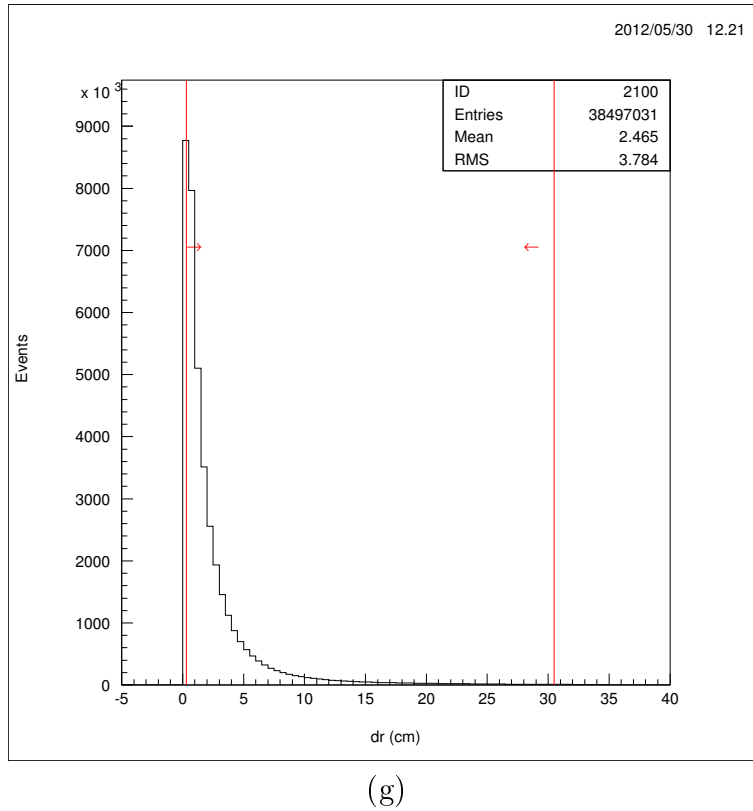
(d)

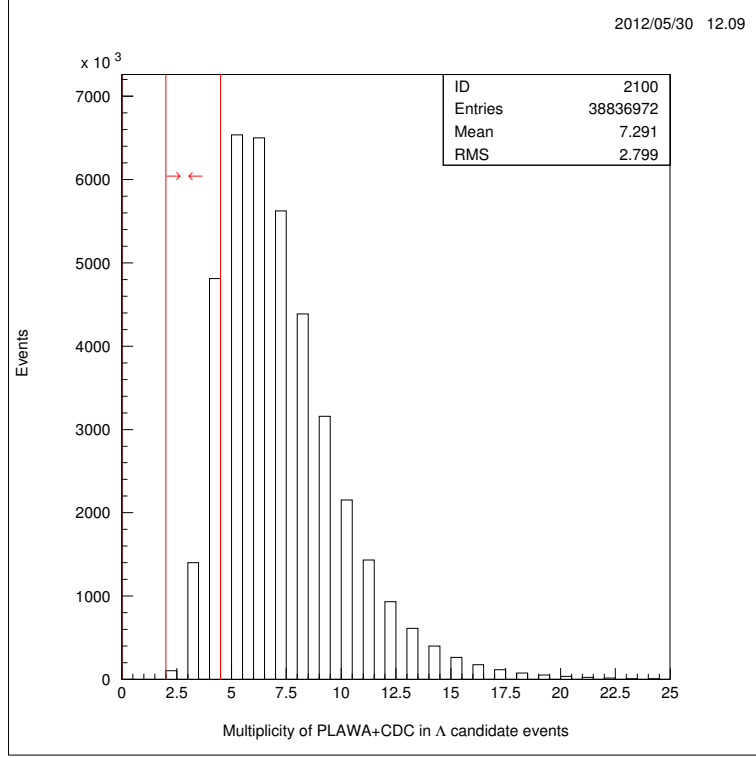


(e)



(f)





(i)

Figure 32: Spectra of the cut quantities for the  $\Lambda$  decay particles  $\pi^-$  and p, respectively, and the  $\Lambda$  itself: (a) number of protons (b) number of  $\pi^-$  mesons (c) closest distance of the  $\Lambda$ -Hyperon track to the primary vertex in the x-y plane ( $dQ$ ) (d) closest distance of the  $\Lambda$ -Hyperon track to the primary vertex in the r-z plane ( $d00$ ) (e) closest distance of the proton track to the primary vertex in the r-z plane ( $d1p$ ) (f) closest distance of the  $\pi^-$  track to the primary vertex in the r-z plane ( $d1pi$ : no explicit cut applied on this quantity (refer to text); the dashed line shows the reduction effect, when the corresponding  $d1p$  cut acts on it) (g) transverse distance between the primary and the secondary vertex ( $dr$ ) (h) transverse momentum of the proton ( $p_{t,p}$ ) (i) sum of the multiplicities of the CDC and PLAWA sub-detectors; the high multiplicities are obtained from particle tracks that are interrupted at some point during their flight through the spectrometer, thus being reconstructed as multiple tracks.



## 5.4 Background Models

In order to obtain the desired quantities, i.e. the number of reconstructed  $\Lambda$ -Hyperons, the background has to be modelled and subtracted from the reconstructed invariant mass spectrum of the  $\Lambda$  particle. Two different methods of background determination have been carried out, which are both suited for quantifying the signal-to-background ratio (S/B) and the content of the  $\Lambda$  signal. They are explained in the subsequent sections.

As already mentioned, the  $\Lambda$  candidates are searched for by applying the secondary vertex reconstruction method to all  $\pi^-$  meson and proton pairs as possible decay daughters in an event. Hence, track pairs that contain protons or  $\pi^-$  mesons, which do not originate from a  $\Lambda$  decay, cannot contribute to the invariant mass spectrum and their combinations produce “fake”  $\Lambda$ -Hyperons, which produce a combinatorial background that has to be modelled.

Most of this background results from the fact that the nuclear force, which is the force between two or more nucleons, is mediated by  $\pi$  mesons. Those are therefore numerous produced, thus offering many combination possibilities of protons and  $\pi^-$  mesons in an event.

The majority of these combinations has already been ruled out by making use of the various vertex cuts, which have been described in the previous section 5.3. Nevertheless, some  $\pi^-$  and proton pairs pass the reconstruction cuts, although they are not correlated by a  $\Lambda$  decay. As a result, a combinatorial background that needs to be subtracted from the invariant mass distribution remains. Figure 36 illustrates the reduction effect that the different cut quantities have on the invariant mass distribution of the  $\Lambda$ -Hyperon.

### 5.4.1 Mixed Event Background

A possible method to model the background is to combine decay particles from different events, i.e. event mixing [DFN84] [Mer04].

Combinations of uncorrelated particles produce a background spectrum in the shape of the combinatorial background of the invariant mass distribution of the  $\Lambda$ -Hyperon. After normalization, the mixed event background can be subtracted from the combinatorics, which contains pairs of  $\pi^-$  mesons and protons that do not belong to a  $\Lambda$  decay, as discussed above. In the following, the method will be explained in detail.

Panel (a) of figure 33 depicts in its upper plot the derived invariant mass spectrum of the  $\Lambda$ -Hyperon, gained from all possible combination pairs of available daughter particles. The nominal  $\Lambda$  mass is given with  $1.116 \text{ GeV}/c^2$ , as listed in table 7. The peak that surrounds this value is clearly visible (after the vertex

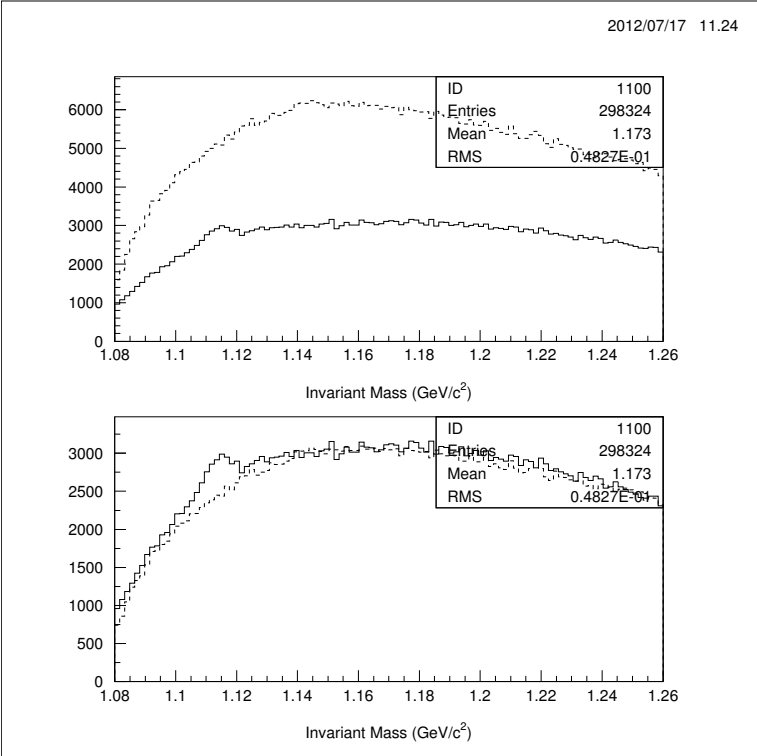
cuts described in section 5.3 have been applied) and contains the  $\Lambda$  candidates. In addition, an underlying background is visible, which ranges from about 1.08 GeV/c<sup>2</sup> - this is the sum of the proton and  $\pi^-$  meson mass as given in table 6 - to the upper end of the displayed part of the spectrum.

As already described above, the combinatorial background spectrum represents fake  $\Lambda$  candidates, which passed the vertex cuts and which result from “daughter” particles that are not correlated by a  $\Lambda$  decay. Therefore, the background is determined with the event mixing method that combines proton and  $\pi^-$  mesons from different events. As they are by definition not correlated, the corresponding invariant mass spectrum, which is presented as dashed curve in the upper plot of panel (a) in figure 33, does not show the mass peak of the  $\Lambda$ -Hyperon.

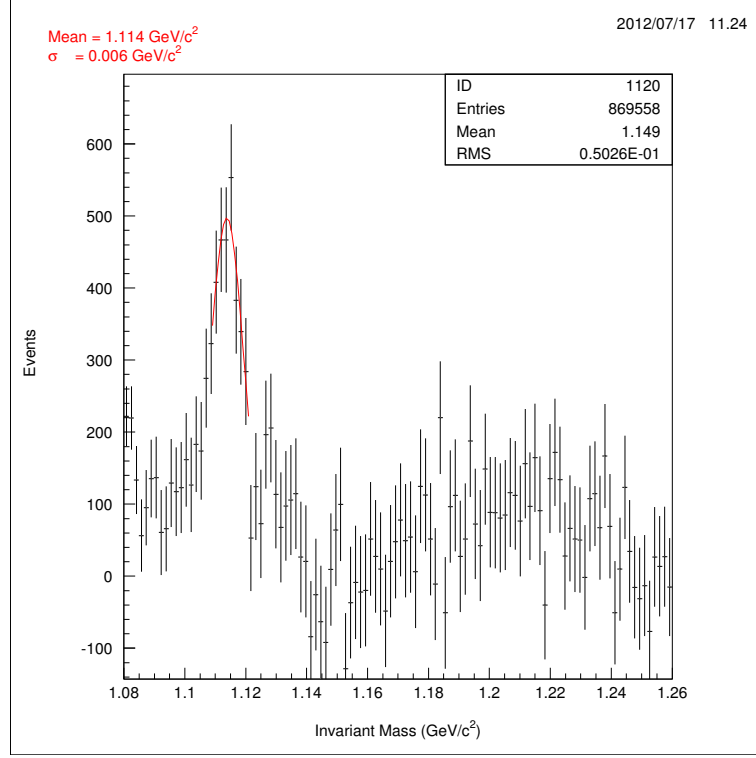
Before the mixed event background spectrum can be subtracted from the combinatorics, it has to be adjusted to it by applying a normalization factor. This factor is determined by integrating each of the two spectra over an identical mass range, where only combinatorial background is expected. Thereafter the ratio of the resulting integrals is computed, hence yielding the normalization factor.

The lower plot of panel (a) in figure 33 depicts the normalized background spectrum (dashed line) together with the measured invariant mass spectrum (solid line) before they are subtracted. The result of the subtraction is finally shown as background corrected mass spectrum in panel (b) of figure 33, where the remaining mass peak is already fitted with a Gaussian distribution yielding the mass of the reconstructed  $\Lambda$ -Hyperon. Although it is not obvious that the detector acceptance is symmetric and therefore the mass peak Gaussian distributed, the  $\chi^2$  value of 0.52 indicates that the peak can be described sufficiently well by a Gaussian curve.

As the combinatorial background has vanished at this stage of the analysis on a wider fitting range than just around the significant mass peak, the event mixing method can be seen as reasonably well suited for the description of the combinatorial background.



(a)



(b)

Figure 33: Illustration of the background subtraction process with the event mixing method for the invariant mass distribution of the  $\Lambda$ -Hyperon. (a) The solid black curve in the upper plot depicts the invariant mass spectrum (combinatorics) for the entire statistics, as deduced from combining all possible proton and  $\pi^-$  meson pairs of an event. The position of the nominal  $\Lambda$  mass is given with  $m_\Lambda = 1.116 \text{ GeV}/c^2$  (refer to table 7). The  $\Lambda$  candidates are clearly visible as peak surrounding this value. The dashed black curve in the upper plot shows the mixed event background spectrum, as derived from combinations of uncorrelated p and  $\pi^-$  pairs, namely those of different events. As they are not correlated, no mass peak is observed. To determine the normalization factor for the mixed event background, these two spectra are integrated over a certain range, where only combinatorial background is expected and the areas are compared thereafter. The lower plot displays the combinatorics and the scaled background spectrum before they are subtracted. (b) Background corrected invariant mass spectrum of the  $\Lambda$ -Hyperon after the subtraction of the scaled background distribution has been carried out. In good approximation, it can be fitted with a Gaussian distribution yielding a  $\chi^2$  of 0.52.

### 5.4.2 Polynomial Background

Another possibility to determine the background is to fit a polynomial curve to the measured spectrum, where the mass peak is taken into account as Gaussian function.

In detail, a polynomial function of fifth order

$$P(x) = \sum_{i=0}^5 a_i x^i = a_0 + a_1 x^1 + a_2 x^2 + a_3 x^3 + a_4 x^4 + a_5 x^5$$

in combination with a Gaussian distribution

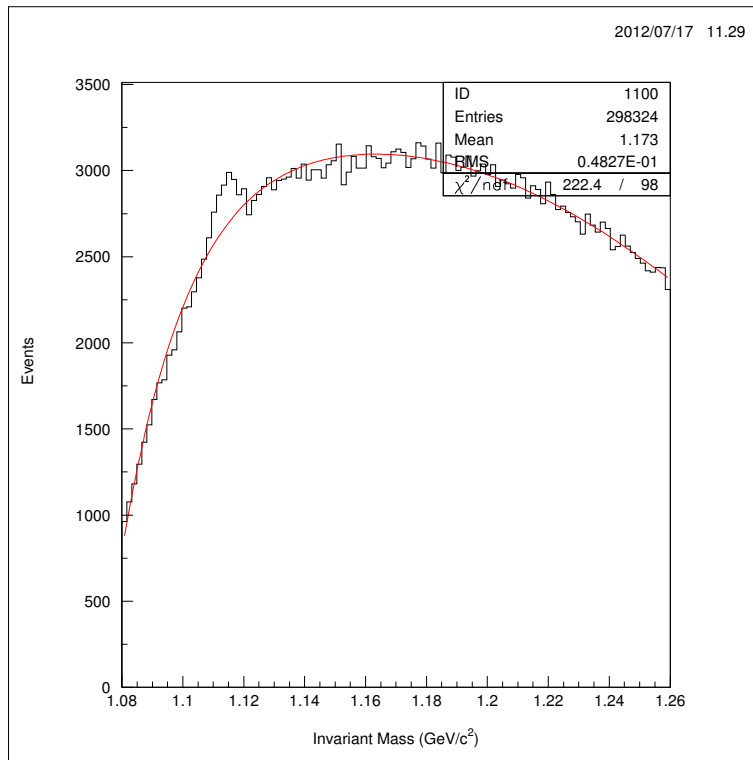
$$G(x) = \frac{1}{\sigma\sqrt{2\pi}} \exp^{-\frac{1}{2}\left(\frac{x-\mu}{\sigma}\right)^2}$$

with expectation value  $\mu$  for the location of the peak and standard deviation  $\sigma$ , thus  $P(x) + G(x)$ , is fitted to the invariant mass spectrum of the  $\Lambda$ -Hyperon in a relatively wide mass region around the mass peak, trying to have a rather good description of the combinatorial background. The region that was chosen ranges from 1.08 GeV/c<sup>2</sup>, what is approximately the sum of the proton and the  $\pi^-$  masses, to 1.26 GeV/c<sup>2</sup>, where only combinatorial background is expected. Afterwards, only the polynomial part of the fit is subtracted from the distribution, as the Gaussian accounts for the mass peak that should be left over after background elimination. The procedure and the result of this method are shown in panels (a) and (b) of figure 34, respectively.

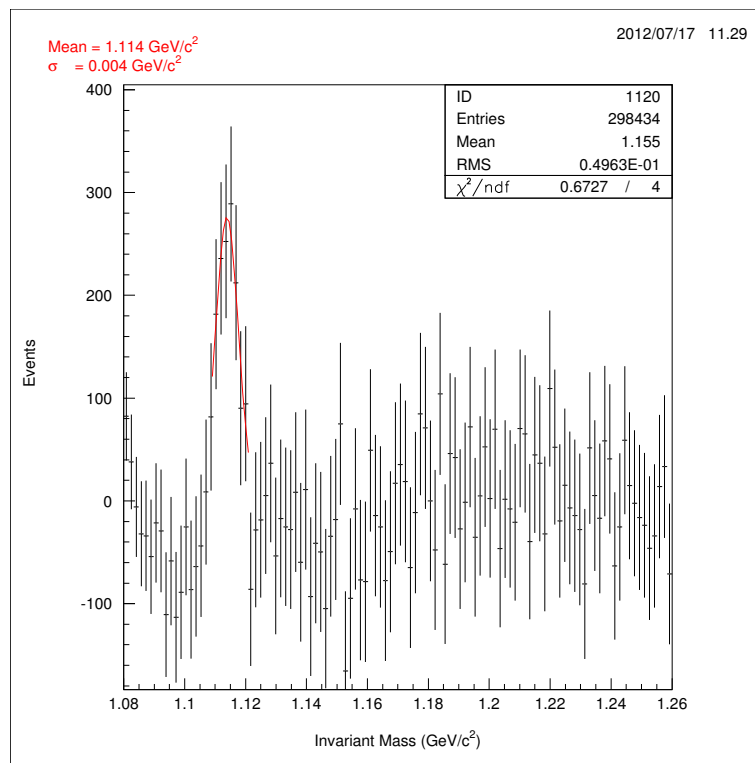
Since in contrast to the mixed event method the shape of the combinatorial background is not known a priori, it may not be beneficial to include such a wide fitting region. This is advantageous in the case of linear backgrounds or in the case of spectra with already known background, e.g. mixed event background, because either the extrapolation precision is then expected to be improved, or it can be shown that if the background vanishes in the corrected invariant mass spectrum after subtraction of the background function, the mixed event method works. Moreover, the analysis focuses on the reconstruction of the  $\Lambda$  signal, whose location is exactly known ( $m_\Lambda = 1.116$  GeV/c<sup>2</sup>), rather than on the search for an unknown resonance with unidentified mass. Hence, it is clear that the invariant mass spectrum should only contain a Gaussian function, which is located at the position of the known  $\Lambda$  mass. Therefore, only a tiny region around the mass peak, ranging from 1.09 GeV/c<sup>2</sup> to 1.15 GeV/c<sup>2</sup>, is fitted with the polynomial function of fifth order plus the Gaussian distribution that represents the mass peak. This fit function tries to describe the spectrum to the right and to the left of the peak reasonably well. If finally the subtraction

of the polynomial part of the fit yields a distribution that can be described sufficiently well with a Gaussian function without undershoots on the left or right, the background determination is well suited to quantify the content of the  $\Lambda$  signal [Suz12] [Har12]. Panels (c) and (d) of figure 34 present the procedure and the result of this kind of background determination.

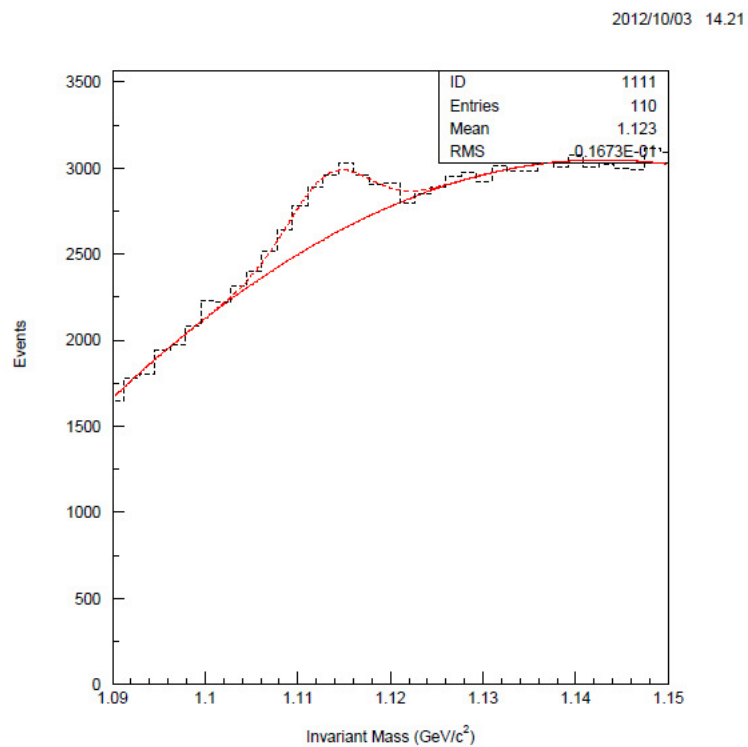
On comparison of the  $\chi^2$  values of the fit curves, one can see that the method that includes only a tiny fitting range around the mass peak is better suited for describing the combinatorial background. It yields a  $\chi^2$  value of 0.67 compared to a  $\chi^2$  of 2.27, which is achieved by fitting a broader range of the invariant mass distribution, as shown in panel (a) of figure 34.



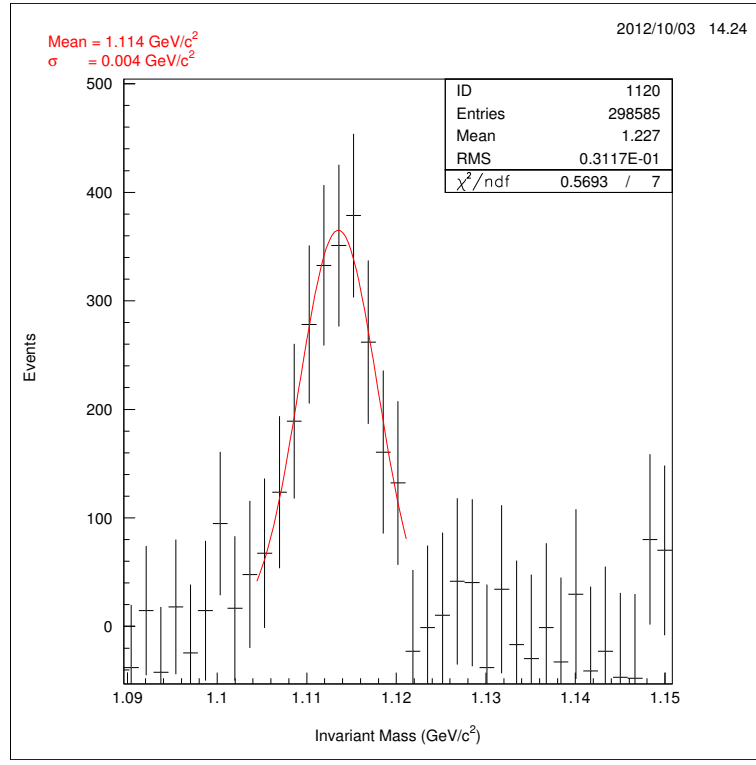
(a)



(b)



(c)



(d)

Figure 34: Illustration of the background subtraction process with a polynomial fit in combination with a Gaussian distribution for the invariant mass distribution of the  $\Lambda$ -Hyperon. (a) Invariant mass spectrum (combinatorics) for the entire statistics, as derived from the combination of all possible proton and  $\pi^-$  mesons of an event. The  $\Lambda$  candidates are clearly visible as a peak surrounding the nominal  $\Lambda$  mass of  $m_\Lambda = 1.116 \text{ GeV}/c^2$ , as given in table 7. The red curve depicts the background spectrum, which is modelled with the polynomial part of the polynomial fit curve of fifth order plus the Gaussian distribution. (b) Background corrected invariant mass spectrum of the  $\Lambda$ -Hyperon, which is achieved after the subtraction of the polynomial background curve (displayed as red curve in the panel above) has been applied. (c) Invariant mass spectrum displayed in the mass region (= fitting region) from  $1.09 \text{ GeV}/c^2$  to  $1.15 \text{ GeV}/c^2$ . In this case the spectrum is fitted with a polynomial curve of fifth order plus a Gaussian function that accounts for the  $\Lambda$  mass peak (red curve) such that the spectrum to the left and to the right of the mass peak is well described. Both parts of the fit curve are explicitly displayed. (d) Background corrected invariant mass spectrum after subtraction of the polynomial part of the fit function. The distribution can be described by a Gaussian function, which is therefore reasonably well suited to quantify the signal content.



## 5.5 Inclusive Event Analysis

In order to achieve the invariant mass distribution  $M_{inv,\Lambda}(p\pi^-)$  of the  $\Lambda$ -Hyperon with the invariant mass technique, all possible  $p\pi^-$  pairs of an event are correlated, producing secondary vertex candidates. Figure 35 shows the obtained invariant mass distribution of the  $\Lambda$ -Hyperon before the various vertex cuts, which are listed in table 8, are applied to it. The respective steps of this analysis have been described in the previous sections.

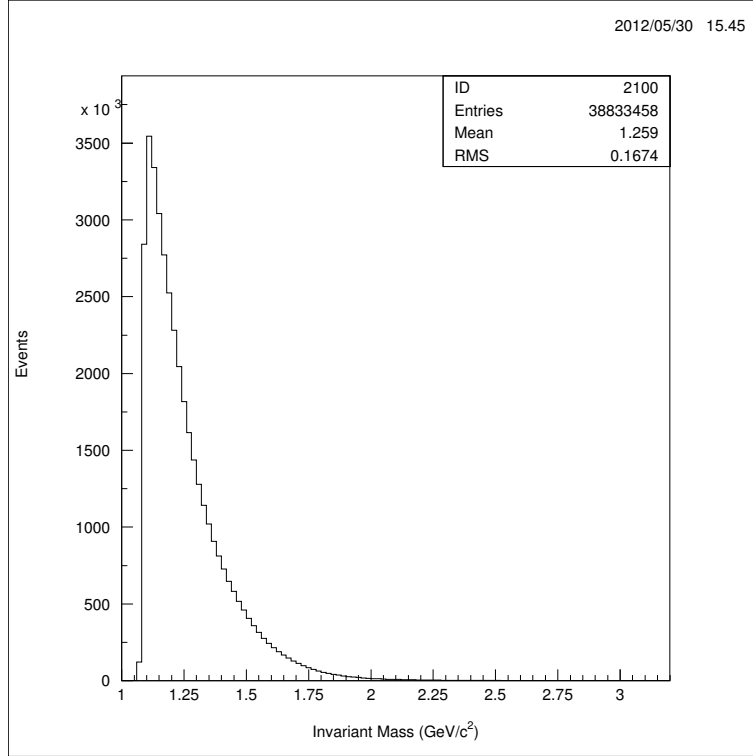


Figure 35: Invariant mass spectrum of the  $\Lambda$ -Hyperon before the vertex cuts, which are listed in table 8, are applied.

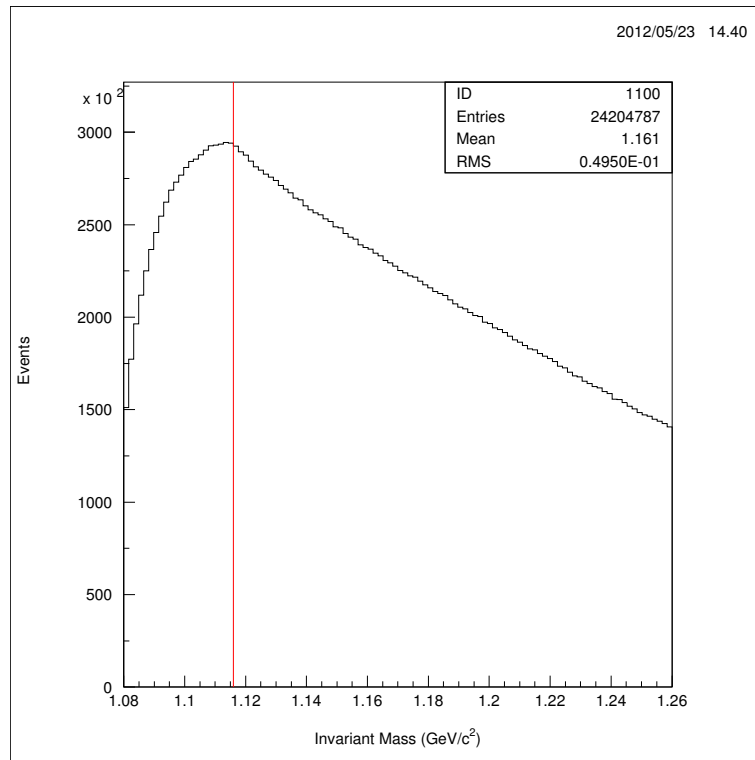
This spectrum is again depicted in panel (a) of figure 36. But now, the spectrum ranges from 1.08  $\text{GeV}/c^2$ , what corresponds to the sum of the masses of the proton and the  $\pi^-$  meson, to 1.26  $\text{GeV}/c^2$ , a value that is supposed to be located far enough from the expected  $\Lambda$  mass peak around its nominal mass  $m_\Lambda = 1.116 \text{ GeV}/c^2$  (see table 7) such that a sufficient region, where only combinatorial background is expected, is left over for the calculation of the normalization factor, with which the mixed event background is adjusted. All invariant mass distributions, which are shown in the following figures, will be limited to this mass range.

The majority of the uncorrelated decay particles (“fake”  $\Lambda$ -Hyperons) is subsequently ruled out via the application of vertex cuts. The panels (b) to (i)

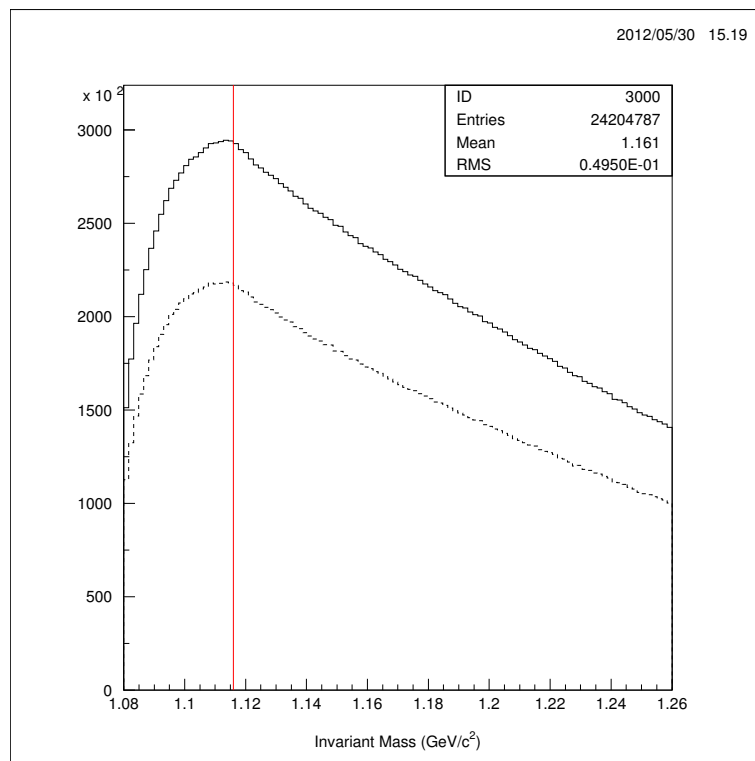
illustrate the reduction effect that the various vertex cuts have on the invariant mass distribution by comparing the spectrum without vertex cuts to the spectrum that is achieved with the respective vertex cut. There are very loose constraints, such as the cut on the number of  $\pi^-$  mesons per event or the cut on the transverse distance  $dr$  between the primary and the secondary vertex, while others cause a rather strong decimation of the  $\Lambda$  candidates, e.g. the demand for a maximum of four detected tracks per event (multiplicity cut). Table 9 displays the reduction effect of the various vertex cuts in percentage terms.

cut quantity	reduction effect [%]
no. of p	27.04
no. of $\pi^-$	00.00
dQ	35.07
d00	55.62
d1p	20.81
dr	10.56
$P_{t,p}$	16.10
multiplicity CDC+PLAWA	87.46

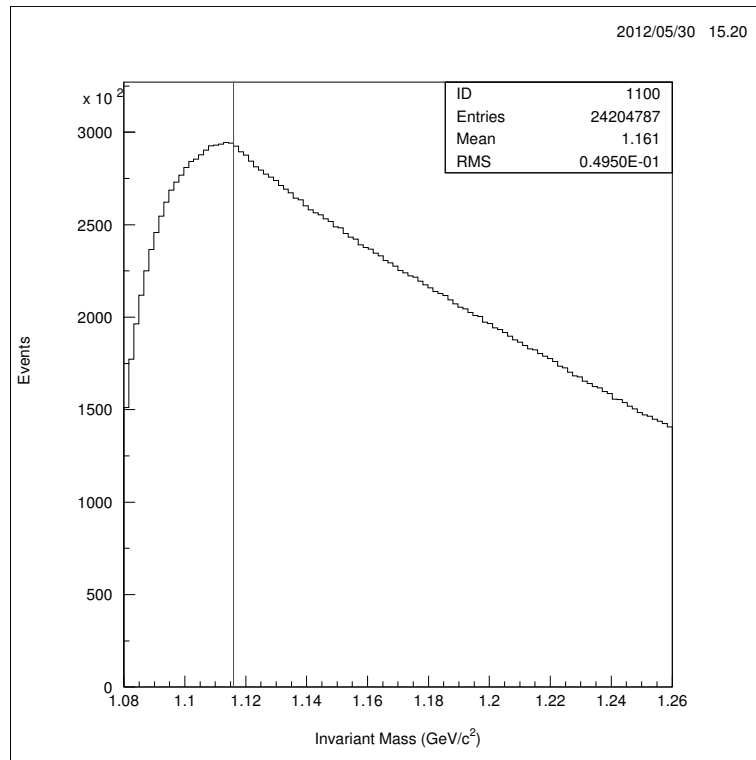
Table 9: Reduction effect that the various vertex cuts have on the invariant mass distribution of the  $\Lambda$ -Hyperon.



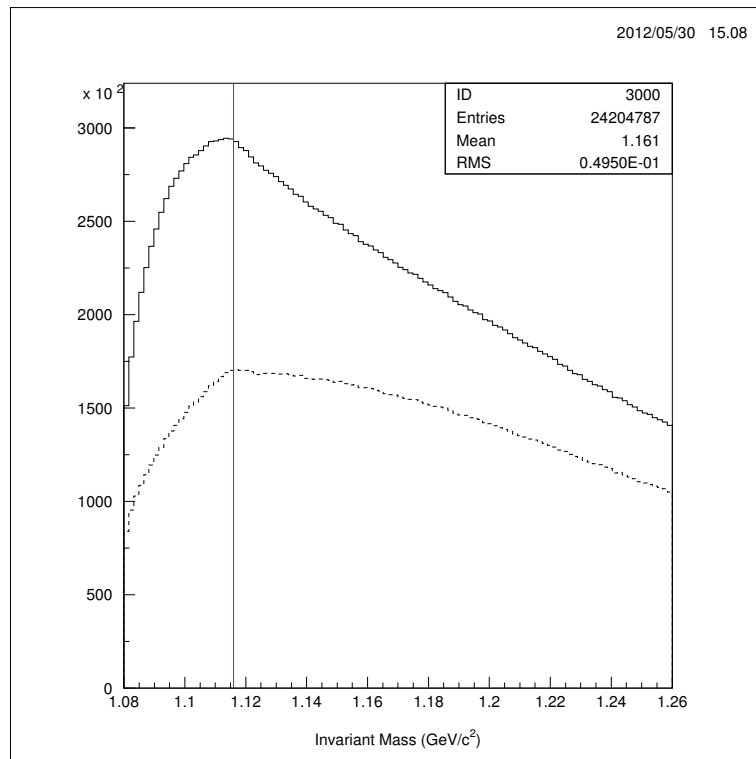
(a)



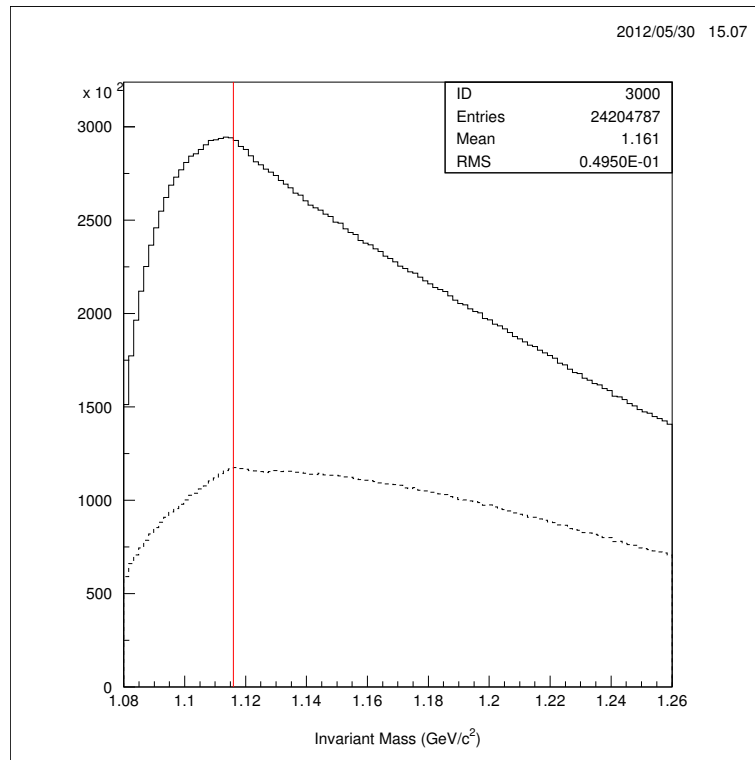
(b)



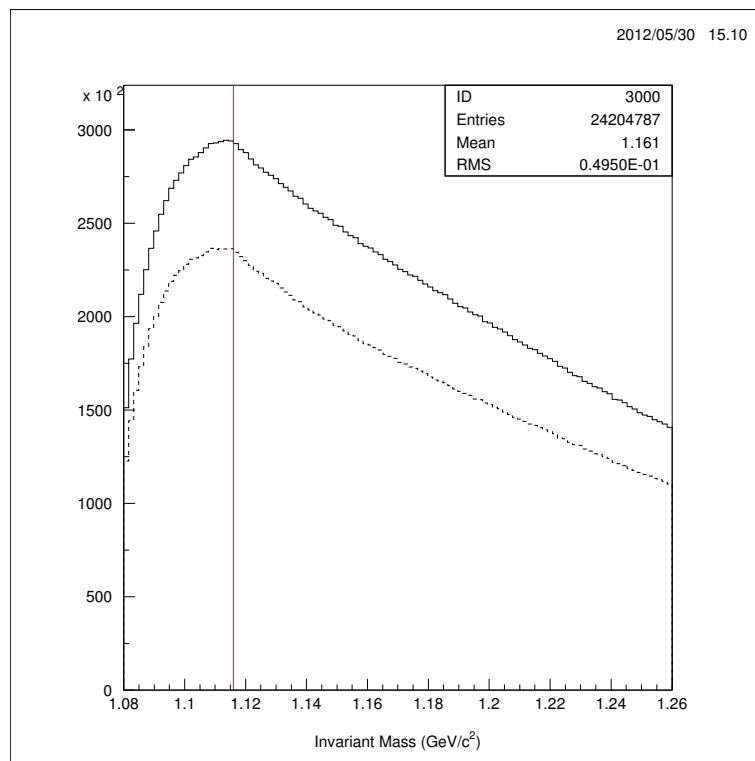
(c)



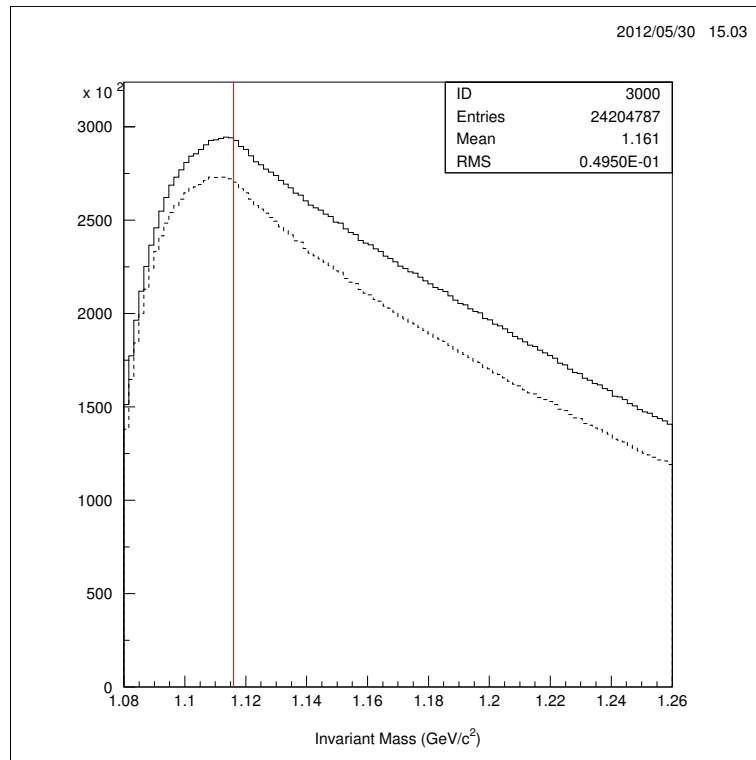
(d)



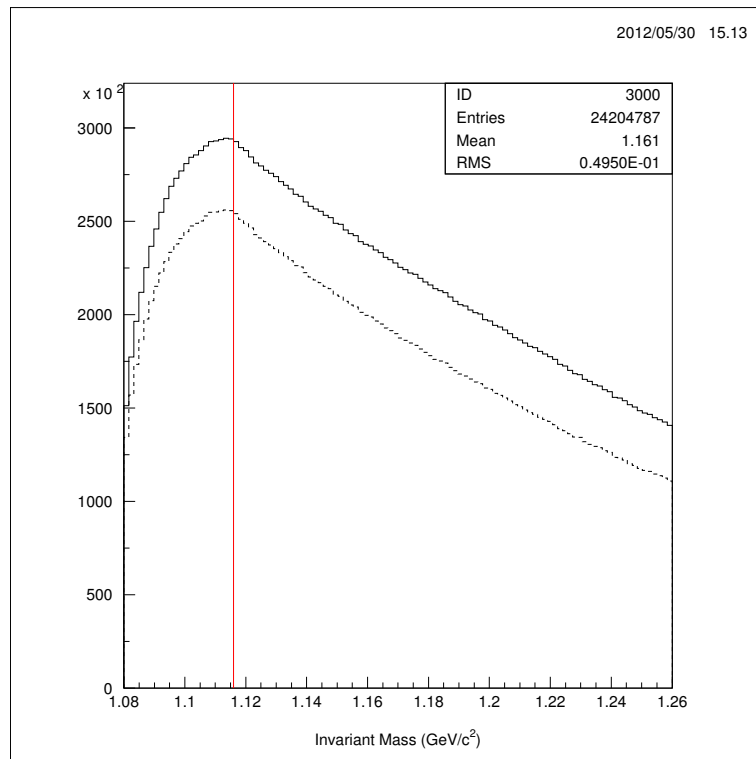
(e)



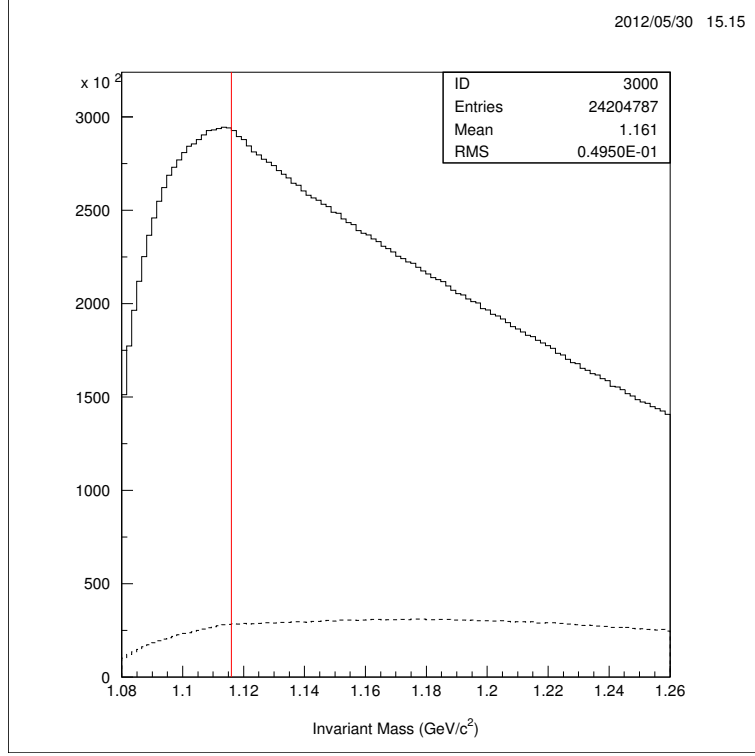
(f)



(g)



(h)



(i)

Figure 36: Invariant mass distribution of the  $\Lambda$ -Hyperon, derived from the combination of all possible proton and  $\pi^-$  meson pairs in an event for the entire statistics. The red line symbolizes the position of the nominal mass of the  $\Lambda$ -Hyperon,  $m_\Lambda = 1.116 \text{ GeV}/c^2$ . The different pictures illustrate the reduction effect that the various vertex cuts have on the invariant mass distribution. The solid line spectrum represents the plain mass distribution, where no vertex cut has been applied. On the contrary, the dashed line spectrum depicts the mass distribution that is achieved after a certain cut has been applied to it. Vertex cuts: (a) without any applied vertex cuts (plain distribution) (b) number of protons (c) number of  $\pi^-$  mesons (This vertex cut has no effect on the invariant mass spectrum at all, as it happens that there is at least one  $\pi^-$  meson identified in each event.) (d) closest distance of the  $\Lambda$ -Hyperon track to the primary vertex in the x-y plane ( $dQ$ ) (e) closest distance of the  $\Lambda$ -Hyperon track to the primary vertex in the r-z plane ( $d00$ ) (f) closest distance of the proton track to the primary vertex in the r-z plane ( $d1p$ ) (g) transverse distance between the primary and the secondary vertex ( $dr$ ) (h) transverse momentum of the proton ( $p_{t,p}$ ) (i) sum of the multiplicities of the CDC and PLAWA sub-detectors.

Figure 37 displays the invariant mass spectrum, which is finally obtained with the cumulative application of all vertex cuts. It reveals a well-defined peak around the nominal  $\Lambda$  mass (red line) that sits on the top of the combinatorial background, resulting from uncorrelated decay pairs, which have passed the reconstruction cuts.

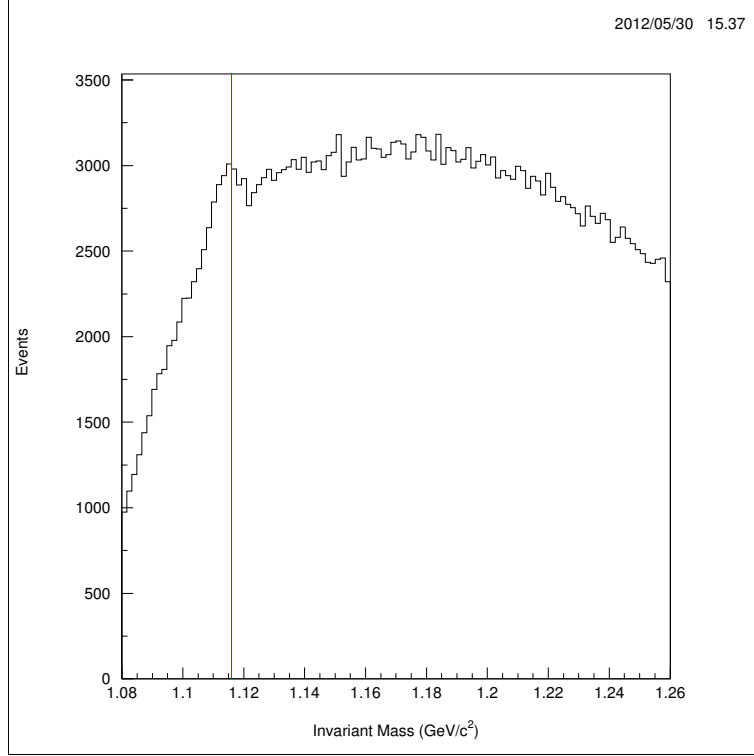


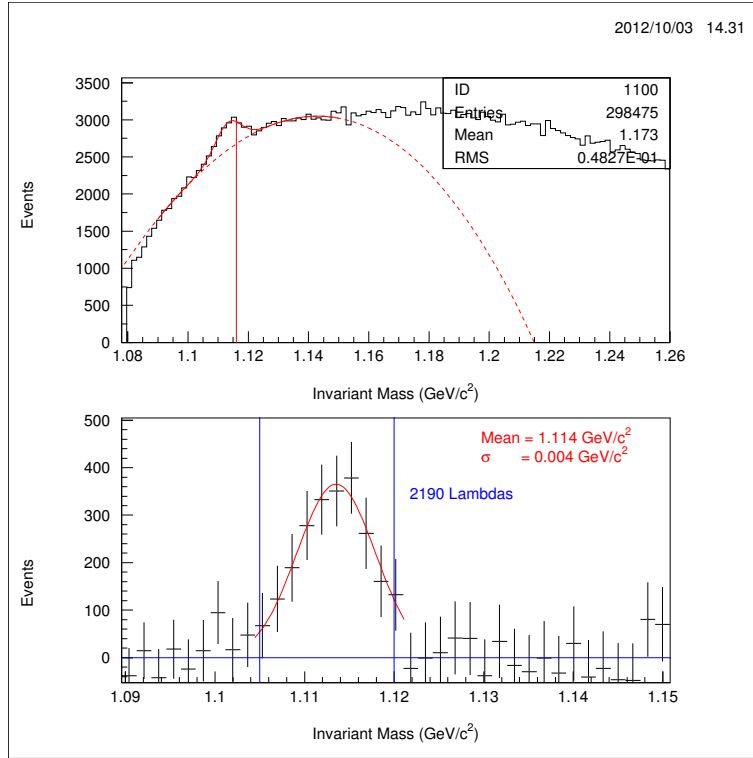
Figure 37: Invariant mass spectrum of the  $\Lambda$ -Hyperon after all vertex cuts, which are listed in table 8, have been applied. The red line shows the position of the nominal  $\Lambda$  mass  $m_{\Lambda} = 1.116 \text{ GeV}/c^2$ .

The next step in the inclusive event reconstruction constitutes the subtraction of the combinatorial background. I have made several approaches to sufficiently describe the background shape, which are all discussed in section 5.4. First, I fitted the invariant mass distribution in the small region ranging from 1.09  $\text{GeV}/c^2$  to 1.15  $\text{GeV}/c^2$  with a polynomial curve of fifth order plus a Gaussian function that accounts for the observed mass peak. The result is depicted in panel (a) of figure 38. The second attempt involves the creation of a mixed event background, as described in section 5.4.1, which is adjusted to the invariant mass spectrum with a normalization factor of approximately 0.52. The corresponding background corrected invariant mass spectrum is shown in panel (b) of figure 38. After the subtraction of the background, the mass peak in the corrected spectrum was fitted with a Gaussian distribution in good approximation of the mass distribution to extract the mass and the width of the peak. It

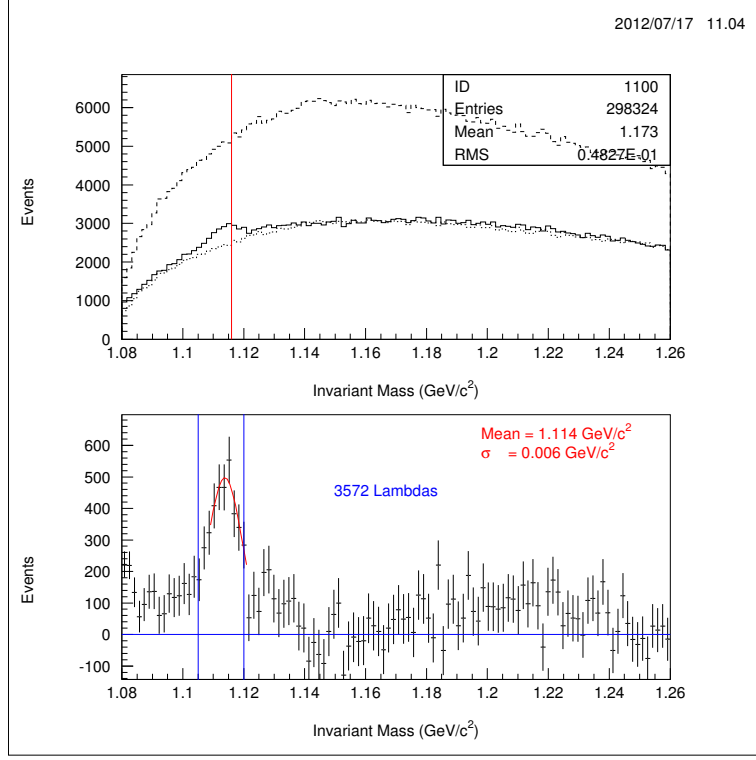


can be observed that the peak position and the width  $\sigma$  agree for all attempts. The horizontal blue lines symbolize the region of the spectrum, in which the mass peak was integrated over in order to obtain the number of reconstructed  $\Lambda$ -Hyperons.

As already pointed out in section 5.4.1, Panel (b) of figure 38 shows again that the mixed event background seems to be reasonably well suited for describing the combinatorial background of the invariant mass spectrum. The event mixing method is moreover generally accepted for the description of combinatorial background shapes, because it uses experimental data instead and does not need to rely on the accuracy of various fitting techniques. Furthermore, figure 38 reveals that the content of  $\Lambda$  signal is higher compared to the one that the polynomial background description yields. For all those reasons, I have finally made my decision to the credit of this method. The peak in the background corrected  $\Lambda$  spectrum is located at  $1.114 \text{ GeV}/c^2$ , which is only slightly below the nominal  $\Lambda$  mass of  $m_\Lambda = 1.116 \text{ GeV}/c^2$ . The width of only  $6 \text{ MeV}/c^2$  is determined by the momentum resolution of the CDC drift chamber.



(a)



(b)

Figure 38: Two approaches for the description of the combinatorial background of the invariant mass spectrum  $M_{inv,\Lambda}(p\pi^-)$  of the  $\Lambda$ -Hyperon are illustrated. The upper panels of the figures show the combinatorics (black curve) and the fitting function as red curve (polynomial function of fifth order - here drawn for the total visible spectrum, but of course only the sector between 1.09 GeV/c<sup>2</sup> and 1.15 GeV/c<sup>2</sup> of the polynomial function is subtracted - plus Gaussian distribution for the mass peak) in (a) or the mixed event background and the normalized mixed event background as dashed black curve in (b), respectively. The background corrected spectra after the subtraction of the polynomial background in a small region around the mass peak (a) and the mixed event background (b), are depicted in the lower panels together with the  $\Lambda$  yield.

There are two main regions for the  $\Lambda$  reconstruction that are of particular interest. According to the kinematical relations, which have been obtained from simulation (see section 1.2.3), the decay particles from the  $\Lambda$  decay are expected to fly out at a forward angle. Therefore, the most interesting case is the one where particle tracks are reconstructed in the Helitron drift chamber. This situation is depicted in figure 39. In panel (a) the case with two forward flying decay particles is illustrated and panel (b) shows the situation, where a proton detected with the Helitron and a  $\pi^-$  meson tracked by the CDC are combined.

In this context, the necessity of the detector component SiAViO (see section 3.6) gets obvious, as the Helitron is characterized by a rather low momentum resolution and a very limited secondary vertex reconstruction capability. This region is dominated by combinatorial background and a rather low S/B ratio for the invariant mass of the  $\Lambda$ -Hyperon. Thus, additional tracking information provided by SiAViO is inevitable for this acceptance region.

Nevertheless, the Helitron region is still characterized by resolution problems, which do not allow to reasonably reconstruct a secondary vertex candidate and to extract a significant signal out of the dominating combinatorial background if both particles travel forward. Therefore, the case in which the proton is forward boosted, thus being detected by the Helitron, and the  $\pi^-$  meson traverses through the CDC, becomes the most interesting one for the reconstruction of the  $\Lambda$ -Hyperon. This case is illustrated in panel (b) of figure 39 and accounts for the majority of the reconstructed  $\Lambda$  candidates, which are identified in figure 38.

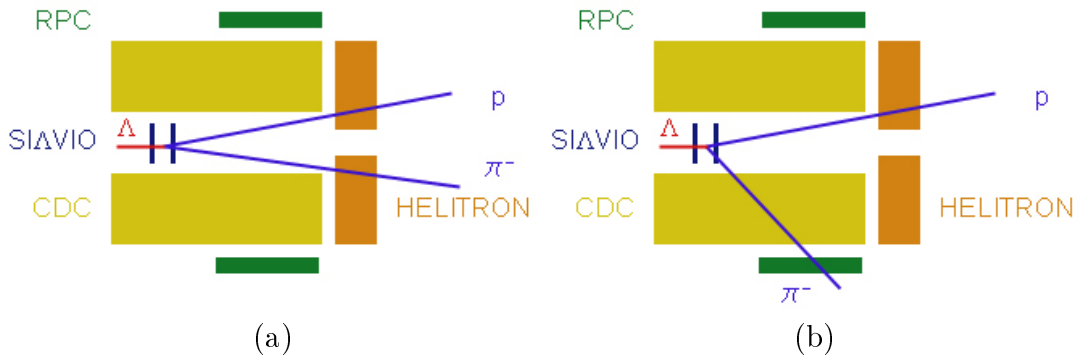


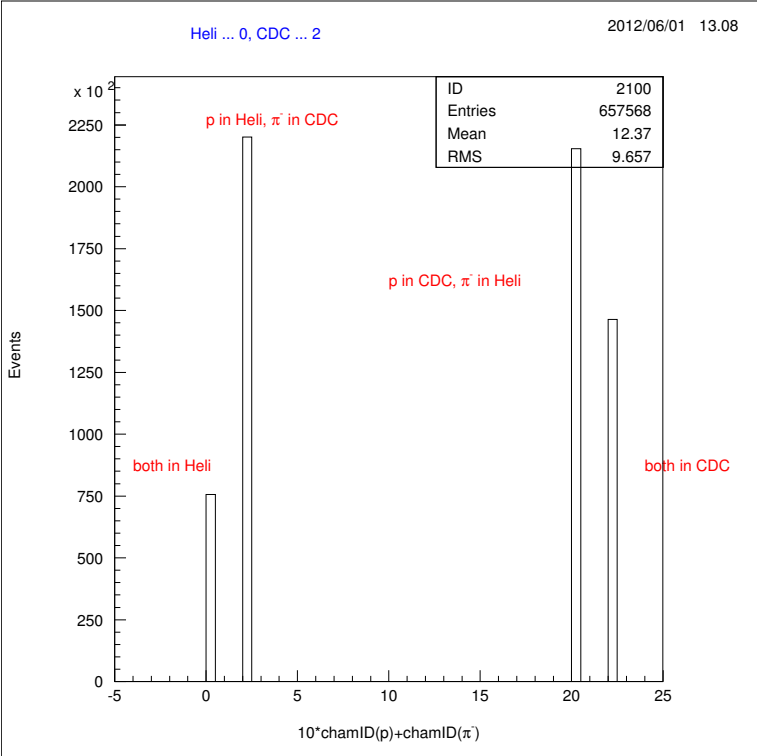
Figure 39: (a) Both decay particles are forward boosted and tracked by the Helitron drift chamber. (b) The proton flies forward and is detected in the Helitron, whereas the  $\pi^-$  meson goes through the CDC.

Besides the two regions described so far, there are two more cases that can be obtained from combining all  $p\pi^-$  pairs of an event. On the one hand, it is possible that both particles, which are used for the secondary vertex recon-

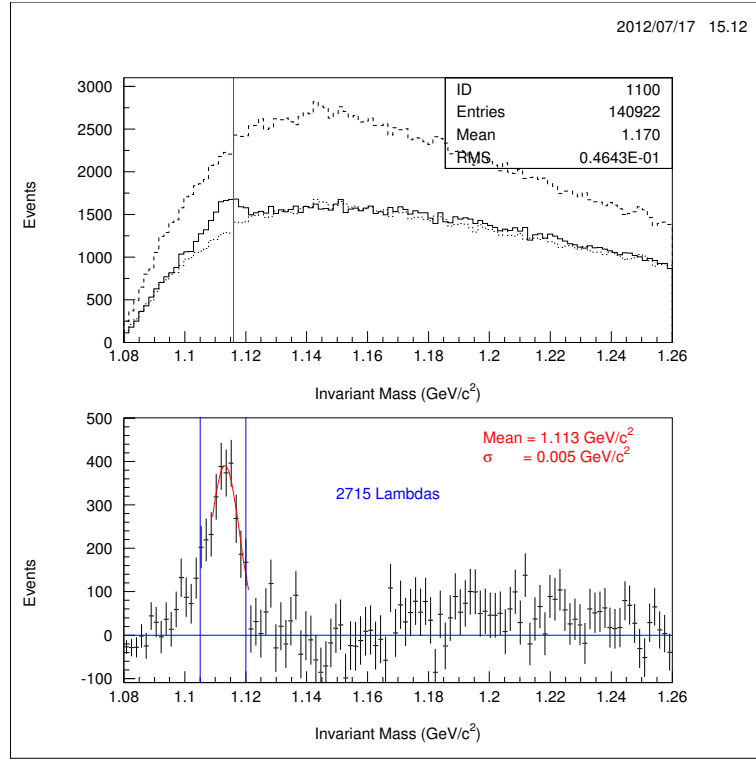
struction, are detected in the CDC. On the other hand there could be pairs, where the proton traverses through the CDC and the  $\pi^-$  goes forward, thus being tracked by the Helitron. These cases are rather unlikely for a possible  $ppK^-$  decay, because the decay products are supposed to be forward boosted (discussed in section 1.2.3). Hence, the corresponding spectrum is dominated by combinatorial background.

Panel (a) of figure 40 shows the likeliness of the various cases in the present analysis. The different regions are given in terms of a chamber ID, which labels the Helitron with ID 0 and the CDC with ID 2, respectively. Each decay particle is either detected by the Helitron or the CDC, thus the combination  $10 \cdot \text{chamID}(p) + \text{chamID}(\pi^-)$  yields an unambiguous code to discriminate between the different regions. Code 0 denominates the case where both particles go through the CDC and code 22 the opposite one where both are tracked by the Helitron. Code 2 stands for combinations where the proton flies forward through the Helitron and the  $\pi^-$  is detected in the CDC, whereas code 20 represents the opposite case with the proton tracked by the CDC and the  $\pi^-$  meson going forward.

The invariant mass spectrum for the region that is coded with 2 (proton in Helitron,  $\pi^-$  in CDC), is depicted in panel (b) of figure 40. It can be observed in comparison with panel (b) of figure 38 that the S/B ratio improves if only this case (with code 2) is considered. Moreover, figure 40 shows that this region accounts for most of the peak content (approximately 76%) of the background corrected invariant mass spectrum in figure 38, as discussed above,.



(a)



(b)

Figure 40: (a) The likeliness of different regions within the FOPI spectrometer, where the decay particles can fall into, is shown. It is given in terms of the chamber ID (Helitron 0, CDC 2) where the combined daughter particles are detected. (b) Invariant mass distribution of the  $\Lambda$ -Hyperon for the case that the proton goes forward and is tracked by the Helitron and the  $\pi^-$  meson traverses through the CDC ( $10 \cdot \text{chamID}(\text{p}) + \text{chamID}(\pi^-) = 2$ ). The mixed event background and the invariant mass spectrum are shown in the same plot (upper panel). The lower panel depicts the background corrected invariant mass spectrum and the peak content. It was fitted in good approximation ( $\chi^2$  value of 0.28) with a Gaussian distribution.

## 6 Outlook

### 6.1 $K^+$ identification and $K^+$ missing mass

The next step in the event analysis is given by a sufficient identification of the  $K^+$  mesons, which occur in the final state of the underlying reaction  $p + p \rightarrow K^+ + [\Lambda + p]$ . This procedure is referred to as semi-inclusive event analysis, as it requires an unambiguously identified kaon in addition to the reconstructed  $\Lambda$ -Hyperon.

According to theoretical calculations, which have been discussed in section 1.2.3, the  $K^+$  mesons are mainly emitted in the backward hemisphere of the FOPI spectrometer with respect to the center of mass frame. Therefore, they should fall into the acceptance region of the CDC, thus being identified via the TOF information provided by the MMRPC detector (see section 4.2). Figure 41 depicts the momentum divided by charge as a function of the particle velocity for the combined information of CDC and MMRPC. The solid black lines represent the analytical hyperbolic cuts, which have been chosen in order to select the kaons. In this first attempt of an semi-inclusive analysis, sufficient separation of the kaons has not been established due to software incompatibilities, as the task of kaon identification within the CDC has to be performed separately and was not included in the software package I have been working with.

Nevertheless, an attempt of a missing mass spectrum  $M_{miss,ppK^+}(pp - K^+)$  has been established with the  $K^+$  mesons that had been previously selected with the TOF information presented in figure 41. The result is shown in figure 42.

On one hand, it can be observed that the distribution falls into the expected region, therefore the conclusion can be drawn that next to the two protons and the  $\pi^-$  meson, a  $K^+$  meson has been selected in the two body final state of the reaction  $p + p \rightarrow K^+ + X^+(S = -1)$ . But on the other hand, it is not possible to observe any signatures or thresholds<sup>52</sup> in the deduced spectrum.

---

<sup>52</sup> E.g.  $p\Lambda$  threshold at 2054.3 MeV,  $\Lambda(1405)p$  threshold at 2343.4 MeV and  $ppK_{free}$  threshold at 2370.3 MeV (for nominal masses of the particles refer to table 1, table 6 and table 7).

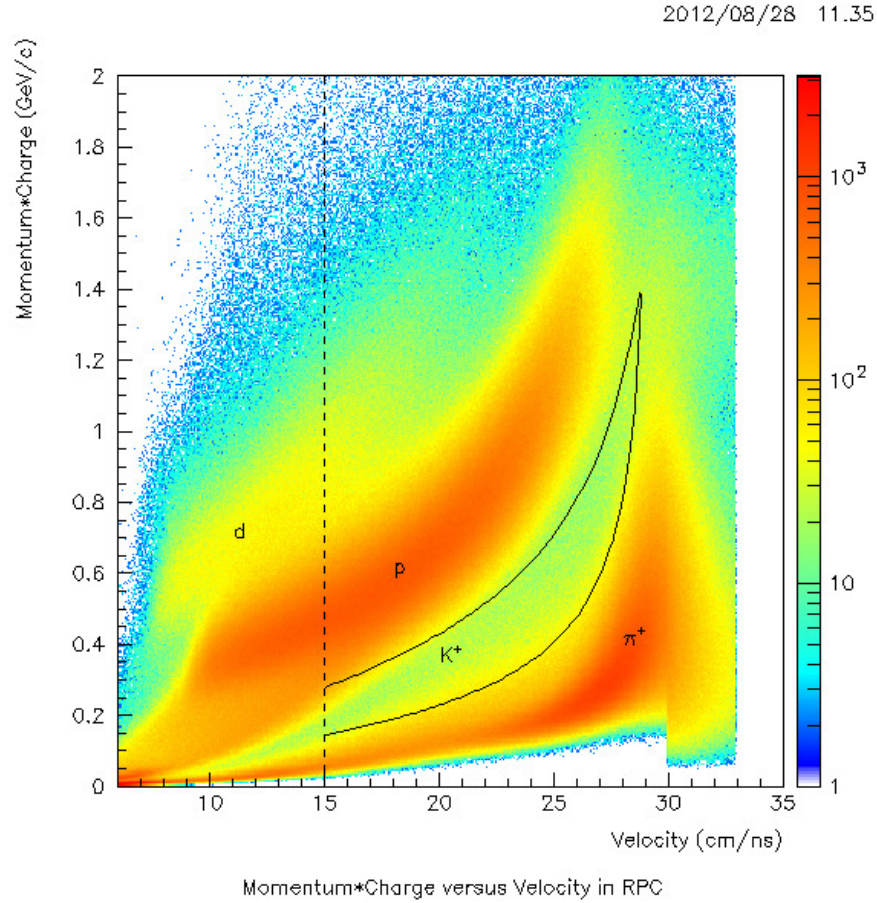


Figure 41: Momentum  $p$  (divided by charge  $q$ ) plotted against the particle velocity  $v$  in order to identify particles via a TOF measurement with the MMRPC detectors. The solid black lines depict the cuts on the mass range in order to select the kaons. Another constraint is imposed by the dashed black line that requires particle velocities above 15 cm/ns.



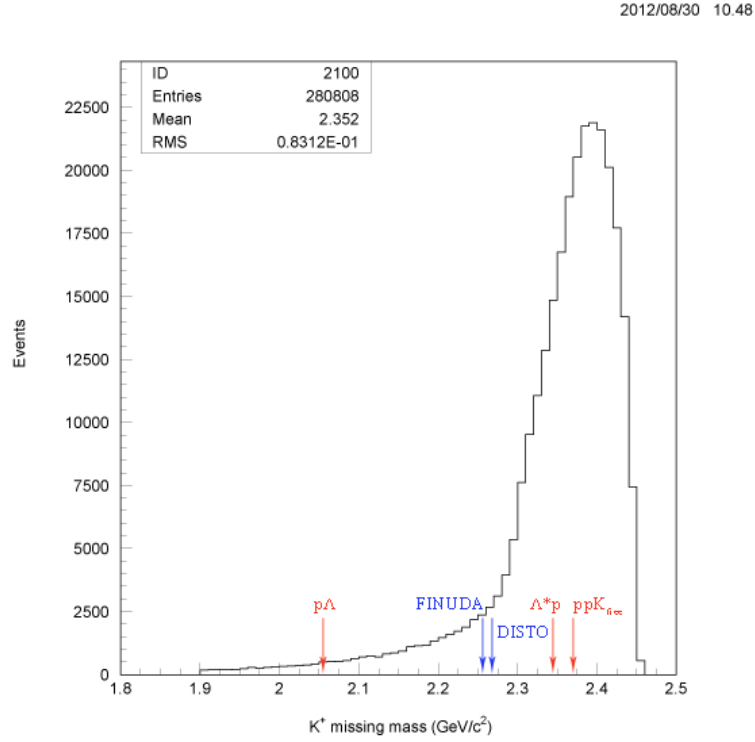


Figure 42: Missing mass spectrum  $M_{miss,ppK^-}(pp - K^+)$  of the  $K^+$  meson. The threshold of  $\Lambda^*p$  is given with 2343.4 MeV, a possible  $ppK^-$  bound state is therefore searched for beyond this boundary (predicted value of 2322 MeV as listed in table 2). The thresholds of  $\Lambda p$  and  $ppK_{free}$  are given with 2054.3 MeV and 2370.3 MeV, respectively. The FINUDA and DISTO collaborations reported on a possible discovery of the  $ppK^-$  state with a mass of 2255 MeV and 2265 MeV, respectively (see section 1.2.4).

## 6.2 $\Lambda p$ correlation

As the aim of the experiment is to observe and investigate the predicted light kaonic nuclear cluster  $ppK^-$ , its decay products have to be correlated within the exclusive event analysis of the reaction  $p + p \rightarrow K^+ + [\Lambda + p]$ . The four charged particles in the final state of this reaction - 2 protons, a  $K^+$  and a  $\pi^-$  meson as illustrated in equation 1.3 - are identified from the energy loss or TOF information combined with the momentum measurement of the respective particles, as described in section 4.

For the purpose of observing the  $ppK^-$  cluster, the  $\Lambda$ -Hyperon has to be reconstructed with the inclusive event analysis, what has been treated within this thesis. Thereafter, the invariant mass spectrum  $M_{inv,ppK^-}(\Lambda p)$  can be obtained with the same procedure that has been developed for the reconstruction of the  $\Lambda$  decay.

For this kind of analysis a sufficient mass resolution and S/B ratio of the reconstructed  $\Lambda$ -Hyperon are essential. A better resolution for the  $\Lambda$  mass can be achieved by using a refitting method, yielding a narrower peak in the invariant mass spectrum  $M_{inv,\Lambda}(p\pi^-)$ . With such a method, the trajectories of the decay particles are refitted after the secondary vertex candidate has been determined, aiming at the improvement of the momentum resolution.

Figure 43 illustrates the principle, on which a possible refitting procedure is based. The original tracks of the decay particles  $p$  and  $\pi^-$  are refitted such that they intersect at the longitudinal position of the secondary vertex  $z_v$  at its transverse position  $dr$  with respect to the primary vertex shown as red dot at the origin of the coordinate system.  $v_z$  is determined by the mean value of the longitudinal coordinates  $z_1$  and  $z_2$  of the real tracks at the position of the secondary vertex. Additionally, the longitudinal positions of the trajectories may be kept fixed at a certain radial position  $r_f$ , which usually corresponds to the middle of the tracking detector (CDC) in r-direction. With the new polar angles  $\vartheta'_1$  and  $\vartheta'_2$ , the 4-momenta of the decay particles can be recalculated, thus achieving a better resolution [Mer04].

Hence, with the development of a refitting method for the decay products of the  $\Lambda$ -Hyperon, a narrower mass peak in the invariant mass spectrum  $M_{inv,\Lambda}(p\pi^-)$  of the reconstructed  $\Lambda$  should be established. In this respect, in particular kinematical refitting constitutes a well-known tool for background reduction and improvement of the mass resolution of intermediate particles, which are reconstructed with the invariant or missing mass technique (see section 5.1).

In [Ple12] a kinematical refit method of this kind has been developed for the exclusive event analysis of the FOPI pp experiment. It represents a mathematical procedure that forces the particle trajectories of the decay products to meet

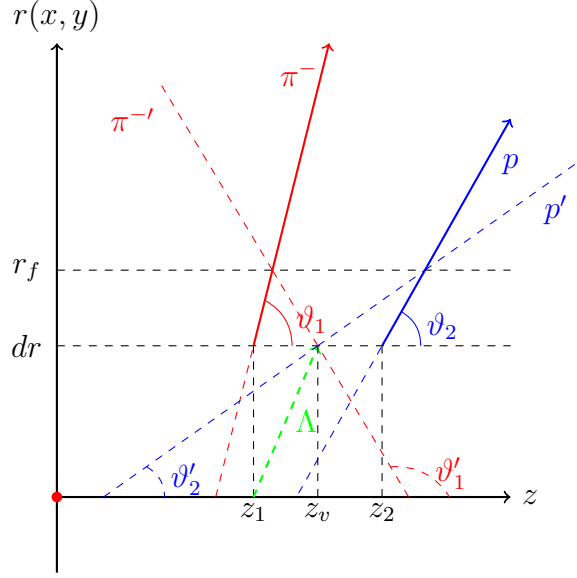


Figure 43: Schematic view of the refitting routine for the trajectories of the decay particles,  $\pi^-$  (solid red line) and  $p$  (solid blue line). The dashed green line depicts the decay of the  $\Lambda$ -Hyperon. The position of the secondary vertex in  $z$ -direction,  $z_v$ , is determined by calculating the mean value of  $z_1$  and  $z_2$ , which are the longitudinal positions of the decay particles at the transverse position  $dr$  of the secondary vertex. The refitted trajectories (red and blue dashed lines) have to intersect at this coordinate and are additionally kept fixed at a certain radial position  $r_f$ , which usually constitutes the axis of the drift chamber in  $r$ -direction.

certain requirements of underlying physical laws and geometrical relations via the application of constraint conditions, such as fundamental principles (energy and momentum conservation), nominal masses of reconstructed particles or geometrical correlations (common vertices). As each particle track is characterized by a certain set of parameters, the outcome of the refitting method is a new set of parameters that meets the external requirements, which are given by the constraint conditions. The trajectories are modified towards new positions, taking estimated uncertainties of the measurements into account. Another key step in this procedure constitutes the identification of the “right” proton - in the sense of originating from the  $\Lambda$  decay - out of the two final state protons. With this in mind, the kinematical refit method has to be applied repeatedly, thus delivering another constraint condition that has to be met.

After all, the application of the refitting method should lead to an improvement of the mass resolution of the intermediate  $\Lambda$ -Hyperon by reducing the large amount of background and therefore enhancing the S/B ratio.

I have made every effort to identify all owners of image copyright and to obtain their approval to use images in this thesis. Should nevertheless a copyright infringement become apparent I kindly request notification.

Ich habe mich bemüht, sämtliche Inhaber der Bildrechte ausfindig zu machen und ihre Zustimmung zur Verwendung der Bilder in dieser Arbeit eingeholt. Sollte dennoch eine Urheberrechtsverletzung bekannt werden, ersuche ich um Meldung bei mir.

## References

- [Aga+09] G. Agakishiev et al. HADES Collaboration,  *$\Phi$  decay: A relevant source for  $K^-$  production at energies available at the GSI Schwerionen-Synchrotron (SIS)?*, Physical Review C, Vol. 80, Issue 2, 025209 (2009) - [doi:10.1103/PhysRevC.80.025209](https://doi.org/10.1103/PhysRevC.80.025209)
- [Agn+05] M. Agnello et al. FINUDA Collaboration, *Evidence for a Kaon-Bound State  $K^-pp$  Produced in  $K^-$  Absorption Reactions at Rest*, Physical Review Letters, Vol. 94, Issue 21, 121303 (2005) - [doi:10.1103/PhysRevLett.94.212303](https://doi.org/10.1103/PhysRevLett.94.212303)
- [Agn+06] M. Agnello et al. FINUDA Collaboration, *A study of the proton spectra following the capture of  $K^-$  in  ${}^6\text{Li}$  and  ${}^{12}\text{C}$  with FINUDA* (2006) - [arXiv:nucl-ex/0606021v1](https://arxiv.org/abs/nucl-ex/0606021v1)
- [ASRS08] M.G. Alford, A. Schmitt, K. Rajagopal, T. Schäfer *Color superconductivity in dense quark matter*, Reviews of Modern Physics, Vol. 80, Issue 4, 1455-1515 (2008) - [doi:10.1103/RevModPhys.80.1455](https://doi.org/10.1103/RevModPhys.80.1455)
- [AY99] Y. Akaishi, T. Yamazaki, *Nuclear medium effects on invariant mass spectra of hadrons decaying in nuclei*, Physics Letters B, Vol. 453, Issue 1-2, pp. 1-6 (1999) - [doi:10.1016/S0370-2693\(99\)00163-X](https://doi.org/10.1016/S0370-2693(99)00163-X)
- [AY02] Y. Akaishi, T. Yamazaki, *Nuclear  $\bar{K}$  bound states in light nuclei*, Physical Revue C, Vol. 65, Issue 4, 044005 (2002) - [doi:10.1103/PhysRevC.65.044005](https://doi.org/10.1103/PhysRevC.65.044005)
- [AY06] Y. Akaishi, T. Yamazaki, *Enhanced formation of a dense  $\bar{K}$  nuclear cluster  $K^-pp$  in  $pp$  collisions -  $\Lambda^*p$  doorway dominance* (2006) - [arXiv:nucl-th/0604049v1](https://arxiv.org/abs/nucl-th/0604049v1)
- [AY107] Y. Akaishi, T. Yamazaki, *Basic  $\bar{K}$  nuclear cluster,  $K^-pp$ , and its enhanced formation in the  $p + p \rightarrow K^+ + X$  re-*

- 
- action*, Physical Revue C, Vol. 76, Issue 4, 045201 (2007) - [doi:10.1103/PhysRevC.76.045201](https://doi.org/10.1103/PhysRevC.76.045201)
- [AY207] Y. Akaishi, T. Yamazaki, *Super strong nuclear force caused by migrating  $\bar{K}$  mesons - Revival of the Heitler-London-Heisenberg scheme in kaonic nuclear clusters*, Proceedings of the Japan Academy, Series B, Vol. 83, No. 5, pp. 144-150 (2007) - [doi:10.2183/pjab.83.144](https://doi.org/10.2183/pjab.83.144)
- [Ben07] M.L. Benabderrahmane, *Measurement of the  $K^0$  Inclusive Cross in Pion-Induced Reactions at 1.15 GeV/c*, Universität Heidelberg, Dissertation (2007)
- [Ben+07] G. Bendiscioli et al., *Search for signals of bound  $\bar{K}$  nuclear states in antiproton- $^4\text{He}$  annihilations at rest*, Nuclear Physics A, Vol. 789, Issue 1-4, pp. 222-242 (2007) - [10.1016/j.nuclphysa.2007.03.010](https://doi.org/10.1016/j.nuclphysa.2007.03.010)
- [Ber09] M.E. Berger, *SiA ViO Entwicklung eines auf Silizium basierenden Trigger und Tracking Systems*, Technische Universität München, Diplomarbeit (2009)
- [BHS+09] P. Bühler, O. Hartmann, M. Schafhauser, K. Suzuki, J. Zmeskal, *Start counter and target system for the FOPI S349 experiment*, GSI Scientific Report, NQMA-Experiments-05, p. 233 (2009) - [www-alt.gsi.de/informationen/wti/library/scientificreport2009/PAPERS/NQMA-EXPERIMENTS-05.pdf](http://www-alt.gsi.de/informationen/wti/library/scientificreport2009/PAPERS/NQMA-EXPERIMENTS-05.pdf) (accessed on July 11, 2012)
- [BR91] G.E. Brown, M. Rho *Scaling effective Lagrangians in a dense medium*, Physical Revue Letters, Vol. 66, Issue 21, 2720-2723(1991) - [doi:10.1103/PhysRevLett.66.2720](https://doi.org/10.1103/PhysRevLett.66.2720)
- [BR96] G.E. Brown, M. Rho *Chiral restoration in hot and/or dense matter*, Physical Reports, Vol. 269, Issue 6, pp. 333-380 (1996) - [doi:10.1016/0370-1573\(95\)00067-4](https://doi.org/10.1016/0370-1573(95)00067-4)
- [CBM11] B. Friman et al. (Eds.), *The CBM Physics Book*, Lecture Notes in Physics, Vol. 814, pp. 916-920, Springer-Verlag Berlin Heidelberg (2011)
- [Cha01] G. Chanfray *Hadrons in dense and hot matter: implications of chiral symmetry restoration*, Nuclear Physics A, Vol. 685, Issue 1-4, pp. 328-345 (2001) - [doi:10.1016/S0375-9474\(01\)00550-4](https://doi.org/10.1016/S0375-9474(01)00550-4)
- [Cro98] P. Crochet,  *$K^+$  Flow in Heavy Ion Collisions at SIS Energies*, Acta Physica Polonica B, Vol. 29, Issue 11, p 3185 (1998) - [http:](http://)

- [//th-www.if.uj.edu.pl/acta/vol29/abs/v29p3185.htm](http://th-www.if.uj.edu.pl/acta/vol29/abs/v29p3185.htm) (accessed on August 28, 2012)
- [DFN84] D. Drijard, H.G. Fischer, T. Nakada, *Study of event mixing and its application to the extraction of resonance signals*, Nuclear Instruments and Methods in Physics Research, Vol. 225, Issue 2, pp. 367-377 (1984) - [doi:10.1016/0167-5087\(84\)90275-8](https://doi.org/10.1016/0167-5087(84)90275-8)
- [DHW09] A. Dote, T. Hyodo, W. Weise *Variational calculation of the  $ppK^-$  system based on chiral  $SU(3)$  dynamics*, Physical Review C, Vol. 79, Issue 1, 014003 (2009) - [doi:10.1103/PhysRevC.79.014003](https://doi.org/10.1103/PhysRevC.79.014003)
- [Fab09] L. Fabbietti, *Search for  $ppK^-$  with proton induced reactions at GSI*, International Journal of Modern Physics E, Vol. 19, Issue 12 (2010) - [arXiv:0911.0299v1](https://arxiv.org/abs/0911.0299v1)
- [FCo07] FOPI Collaboration, *Experimental Proposal to GSI* (2007) - <https://www.gsi.de/documents/DOC-2008-Apr-59-1.pdf> (accessed on July 5, 2012)
- [FH11] K. Fukushima, T. Hatsuda, *The phase diagram of dense QCD*, Reports on Progress in Physics, Vol. 74, Number 1, 014001 (2011) - [doi:10.1088/0034-4885/74/1/014001](https://doi.org/10.1088/0034-4885/74/1/014001)
- [Foe+07] A. Förster et al. KaoS collaboration, *Production of  $K^+$  and of  $K^-$  mesons in heavy-ion collisions from 0.6A to 2.0A GeV incident energy*, Physical Review C, Vol. 75, Issue 2, 024906 (2007) - [doi:10.1103/PhysRevC.75.024906](https://doi.org/10.1103/PhysRevC.75.024906)
- [FOP] FOPI GSI - <http://www-fopi.gsi.de> (accessed on July 3, 2012)
- [Fri11] B. Friman et al. in The CBM Physics Book, *General Introduction*, Lecture Notes in Physics, Vol. 814, pp. 11-37, Springer-Verlag Berlin Heidelberg (2011) - [doi:10.1007/978-3-642-13293-3\\_2](https://doi.org/10.1007/978-3-642-13293-3_2)
- [FWG] FOPI WIKI GSI - <http://wiki.gsi.de/cgi-bin/view/Fopi> (accessed on July 3, 2012)
- [Gei+02] H. Geissel et al. , *Deeply Bound 1s and 2p Pionic States in  $^{205}\text{Pb}$  and Determination of the s-Wave Part of the Pion-Nucleus Interaction*, Physical Review Letters, Vol. 88, Issue 12, 122301 (2002) - [doi:10.1103/PhysRevLett.88.122301](https://doi.org/10.1103/PhysRevLett.88.122301)
- [GSI] GSI Helmholtzzentrum für Schwerionenforschung - <http://www.gsi.de> (accessed on July 3, 2012)
- [Har03] O.N. Hartmann, *Experimentelle Untersuchungen der asymmetrischen Schwerionenreaktionen  $\text{Ca}+\text{Au}$  und  $\text{Au}+\text{Ca}$  bei 1.5*

- 
- GeV/u Projektilenergie*, Universität Darmstadt, Dissertation (2003)
- [Har12] O.N. Hartmann, *Private communications*, 2012
- [HIM] Hadrons in Medium: Virtual Institute for Dense Hadronic Matter and QCD Phase Transitions initiated and financed by the Helmholtz Association - <http://solid13.tphys.physik.uni-tuebingen.de/faessler/Fuchs/VI/hadro.html> (accessed on July 3, 2012)
- [HJ12] T. Hyodo, D. Jido, *The nature of the  $\Lambda(1405)$  resonance in chiral dynamics*, Progress in Particle and Nuclear Physics, Vol. 67, Issue 1, pp. 55-98 (2012) - [doi:10.1016/j.ppnp.2011.07.002](https://doi.org/10.1016/j.ppnp.2011.07.002)
- [HK94] T. Hatsuda, T. Kunihiro, *QCD phenomenology based on a chiral effective Lagrangian*, Physics Reports, Vol. 247, Issue 5-6, pp. 221-367 (1994) - [doi:10.1016/0370-1573\(94\)90022-1](https://doi.org/10.1016/0370-1573(94)90022-1)
- [HW08] T. Hyodo, W. Weise *Effective  $\overline{K}N$  interaction based on chiral  $SU(3)$  dynamics*, Physical Review C, Vol. 77, Issue 3, 035204 (2008) - [doi:10.1103/PhysRevC.77.035204](https://doi.org/10.1103/PhysRevC.77.035204)
- [IG+00] K. Itahashi, H. Gilg et al., *Deeply bound  $\pi^-$  states in  $^{207}\text{Pb}$  formed in the  $^{208}\text{Pb}(d,^3\text{He})$  reaction*, Physical Review C, Vol. 62, 025201 and 025202 (2000) - [doi:10.1103/PhysRevC.62.025201](https://doi.org/10.1103/PhysRevC.62.025201), [doi:10.1103/PhysRevC.62.025202](https://doi.org/10.1103/PhysRevC.62.025202)
- [IKMW08] A.N. Ivanov, P. Kienle, J. Marton, E. Widmann, *Phenomenological model of the Kaonic Nuclear Cluster  $K^-pp$  in the ground state* (2008) - [arXiv:nucl-th/0512037v2](https://arxiv.org/abs/nucl-th/0512037v2)
- [IS07] Y. Ikeda, T. Sato, *Strange dibaryon and  $KNN$ - $\pi$  Sigma  $N$  coupled channel equation*, Physical Revue C, Vol. 76, Issue 3, 035203 (2007) - [doi:10.1103/PhysRevC.76.035203](https://doi.org/10.1103/PhysRevC.76.035203)
- [Iwa+97] M. Iwasaki et al., *Observation of Kaonic Hydrogen  $K_{\alpha}$  X Rays*, Physical Revue Letters, Vol. 78, Issue 16, 3067-3069 (1997) - [doi:10.1103/PhysRevLett.78.3067](https://doi.org/10.1103/PhysRevLett.78.3067)
- [Kis+11] M. Kis et al., *A Multi-strip Multi-gap RPC Barrel for Time-of-Flight Measurements*, Nuclear Instruments and Methods in Physics Research A 646, pp. 27-34 (2011) - [doi:10.1016/j.nima.2011.02.076](https://doi.org/10.1016/j.nima.2011.02.076)
- [KN86] D.B. Kaplan, A.E. Nelson, *Strange goings on in dense nucleonic matter*, Physics Letters B, Vol. 175, Issue 1, pp. 57-63 pp (1986) - [doi:10.1016/0370-2693\(86\)90331-X](https://doi.org/10.1016/0370-2693(86)90331-X)

- 
- [LK95] G.Q. Li, C.M. Ko, *Kaon flow in heavy-ion collisions*, Nuclear Physics A, Vol. 594, Issue 4, pp. 460-482 (1995) - [doi:10.1016/0375-9474\(95\)00377-D](https://doi.org/10.1016/0375-9474(95)00377-D)
- [Mag+06] V.K. Magas, E. Oset, A. Ramos, H. Toki, *Critical view on the deeply bound  $K^-pp$  system*, Physical Review C, Vol. 74, Issue 2, 025206 (2006) - [10.1103/PhysRevC.74.025206](https://doi.org/10.1103/PhysRevC.74.025206)
- [Mar81] A.D. Martin, *Kaon-nucleon parameters*, Nuclear Physics B, Vol. 179, Issue 1, pp. 33-48 (1981) - [doi:10.1016/0550-3213\(81\)90247-9](https://doi.org/10.1016/0550-3213(81)90247-9)
- [Mer04] M. Merschmeyer, *Production and Flow of Neutral Strange Particles in Ni+Ni Collisions at 1.93 AGeV*, Universität Heidelberg, Dissertation (2004)
- [Mue08] R. Münzer, *SiΛViO Ein Trigger für Λ-Hyperonen*, Technische Universität München, Diplomarbeit (2008)
- [Mue+09] R. Münzer, L. Fabbietti, M. Berger, O. Hartmann, *SiΛViO: A Trigger for Λ-Particles* (2009) - [arXiv:0911.2078v1](https://arxiv.org/abs/0911.2078v1)
- [NJL61] Y. Nambu, G. Jona-Lasinio *Dynamical Model of Elementary Particles Based on an Analogy with Superconductivity*, Physical Review Online Archive, Vol. 122, Issue 1 (1961) - [doi:10.1103/PhysRev.122.345](https://doi.org/10.1103/PhysRev.122.345)
- [Ose+12] E. Oset et al., *A new perspective on the Faddeev equations and the View the  $\bar{K}NN$  system from chiral dynamics and unitarity in coupled channels*, Nuclear Physics A, Vol. 881, pp. 127-140 (2012) - [doi:10.1016/j.nuclphysa.2012.02.005](https://doi.org/10.1016/j.nuclphysa.2012.02.005)
- [OT06] E. Oset, H. Toki, *Critical analysis on deeply bound kaonic states in nuclei*, Physical Review C, Vol. 74, Issue 1, 015207 (2006) - [doi:10.1103/PhysRevC.74.015207](https://doi.org/10.1103/PhysRevC.74.015207)
- [PDG] Particle Data Group - <http://pdg.lbl.gov/> (accessed on August 15, 2012)
- [PGSG99] S. Pal, S. Gao, H. Stöcker, W. Greiner, *Meson mass modification in strange hadronic matter*, Physics Letters B, Vol. 465, Issues 1-4, pp. 282-290 (1999) - [doi:10.1016/S0370-2693\(99\)01044-8](https://doi.org/10.1016/S0370-2693(99)01044-8)
- [Pis11] K. Piscicchia, *Kaon-nuclei interaction studies at low energies (the AMADEUS experiment)*, Nuclear Physics B (Proc. Suppl.), Vol. 210-211, pp. 223-226 (2011) - [doi:10.1016/j.nuclphysbps.2010.12.080](https://doi.org/10.1016/j.nuclphysbps.2010.12.080)



- 
- [Ple12] D.M. Pleiner, *Hunting the  $ppK^-$ : A kinematic refit for the exclusive analysis of the reaction  $pp \rightarrow pK^+\Lambda$* , Technische Universität München, Diplomarbeit (2012)
- [PS95] M.E. Peskin, D.V. Schroeder, *An Introduction to Quantum Field Theory*, pp. 545, Westview Press (1995)
- [RHK11] M.S. Ryu, B. Hong, T.I. Kang *FOPI Detector for Heavy-ion Collision Experiment at SIS/GSI*, Journal of the Korean Physical Society, Vol. 59, No. 23, pp. 1605-1608 (2011) - [doi:10.3938/jkps.59.1605](https://doi.org/10.3938/jkps.59.1605)
- [Ryu09] M.S. Ryu, *Production of the proton and light fragments in  $^{96}_{44}\text{Ru} + ^{96}_{44}\text{Ru}$  collisions at SIS18 energies and the multigap Resistive Plate Chamber*, Korea University, Dissertation (2009)
- [Sak+11] F. Sakuma et al., *Double antikaonic nuclear clusters in antiproton- $^3\text{He}$  annihilation at J-PARC*, Hyperfine Interactions (2011) - [doi:10.1007/s10751-011-0393-6](https://doi.org/10.1007/s10751-011-0393-6)
- [Sch+06] A. Schüttauf et al., *Performance of the Multistrip-MRPCs for FOPI*, Nuclear Physics B (Proc. Suppl.), Vol. 158, pp. 52-55 (2006) - [doi:10.1016/j.nuclphysbps.2006.07.033](https://doi.org/10.1016/j.nuclphysbps.2006.07.033)
- [SDG+94] J. Schaffner, C.B. Dover, A. Gal, C. Greiner, D.J. Millener, H. Stocker, *Multiply Strange Nuclear Systems*, Annals of Physics, Vol 235, Issue 1 pp. 35-76 (1994) - [doi:10.1006/aphy.1994.1090](https://doi.org/10.1006/aphy.1994.1090)
- [Sen04] P. Senger, *Particle production in heavy-ion collisions*, Progress in Particle and Nuclear Physics, Vol. 53, Issue 1, pp. 1-23 (2004) - [doi:10.1016/j.ppnp.2004.02.005](https://doi.org/10.1016/j.ppnp.2004.02.005)
- [SGM07] N.V. Shevchenko, A. Gal, J. Mares, *Faddeev Calculation of a  $K^-pp$  Quasibound State*, Physical Review Letters, Vol. 98, Issue 8, 082301 (2007) - [doi:10.1103/PhysRevLett.98.082301](https://doi.org/10.1103/PhysRevLett.98.082301)
- [Sie10] J.S. Siebenson, *Exclusive analysis of the  $\Lambda(1405)$  resonance in the charged  $\Sigma\pi$  decay channels in proton proton reactions with HADES*, Technische Universität München, Diplomarbeit (2010)
- [SMB97] J. Schaffner-Bielich, I.N. Mishustin, J. Bondorf, *In-medium kaon production at the mean-field level*, Nuclear Physics A, Vol. 625, Issues 1-2, pp. 325-346 (1997) - [doi:10.1016/S0375-9474\(97\)81464-9](https://doi.org/10.1016/S0375-9474(97)81464-9)
- [Suz+04] T. Suzuki et al., *Discovery of a strange tribaryon  $S^0(3115)$  in  $^4\text{He}(\text{stopped } K^-, p)$  reaction*, Physical Letters B, Vol. 597, Issue 3-4, pp. 263-269 (2004) - [doi:10.1016/j.physletb.2004.07.046](https://doi.org/10.1016/j.physletb.2004.07.046)

- [Suz12] K. Suzuki, *Private communications*, 2012
- [SW86] R. Staronski, S. Wycech, *The puzzle of  $K\alpha$  bound state*, Czechoslovak Journal of Physics, Vol. 36, Nr. 8, pp. 903-906 (1986) - [doi:10.1007/BF01797496](https://doi.org/10.1007/BF01797496)
- [TY88] H. Toki, T. Yamazaki *Deeply bound pionic states of heavy nuclei*, Physical Letters B, Vol. 213, Issue 2, pp. 129-133 (1988) - [doi:10.1016/0370-2693\(88\)91012-X](https://doi.org/10.1016/0370-2693(88)91012-X)
- [WBW97] T. Waas, R. Brockmann, W. Weise, *Deeply bound pionic states and the effective pion mass in nuclear systems*, Physics Letters B, Vol. 405, Issue 3-4, pp. 215-218 (1997) - [doi:10.1016/S0370-2693\(97\)00643-6](https://doi.org/10.1016/S0370-2693(97)00643-6)
- [Wei01] W. Weise, *Hadronic excitations and chiral symmetry in nuclear systems*, Nuclear Physics A, Vol. 690, Issue 1-3, pp. 98-109 (2001) - [doi:10.1016/S0375-9474\(01\)00934-4](https://doi.org/10.1016/S0375-9474(01)00934-4)
- [WG09] S. Wycech, A.M. Green *Variational calculations for  $K$ -few-nucleon systems*, Physical Revue C, Vol. 79, Issue 1, 014001 (2009) - [doi:10.1103/PhysRevC.79.014001](https://doi.org/10.1103/PhysRevC.79.014001)
- [WKW96] T. Waas, N. Kaiser, W. Weise, *Effective kaon masses in dense nuclear and neutron matter*, Physics Letters B, Vol. 379, Issue 1-4, pp. 34-38 (1996) - [doi:10.1016/0370-2693\(96\)00472-8](https://doi.org/10.1016/0370-2693(96)00472-8)
- [Wyc86] S. Wycech, *On possibilities of narrow nuclear states of  $K^-$* , Nuclear Physics A, Vol. 450, pp. 399-402 (1986) - [doi:10.1016/0375-9474\(86\)90574-9](https://doi.org/10.1016/0375-9474(86)90574-9)
- [Yam+96] T. Yamazaki et al., *Discovery of deeply bound  $\pi^-$  states in the  $^{208}\text{Pb}(d,^3\text{He})$  reaction*, Zeitschrift für Physik A Hadrons and Nuclei, Vol. 355, Nr. 3, pp. 219-221 (1996) - [doi:10.1007/s002180050101](https://doi.org/10.1007/s002180050101)
- [Yam+98] T. Yamazaki et al., *Effective pion mass in the nuclear medium deduced from deeply bound pionic states in  $^{207}\text{Pb}$* , Physics Letters B, Vol. 418, Issue 3-4, pp. 246-251 (1998) - [doi:10.1016/S0370-2693\(97\)01408-1](https://doi.org/10.1016/S0370-2693(97)01408-1)
- [Yam+10] T. Yamazaki et al. DISTO collaboration, *Indication of a Deeply Bound and Compact  $K^-pp$  State Formed in the  $pp \rightarrow p\Lambda K^+$  Reaction at 2.85 GeV*, Physical Review Letters, Vol. 104, Issue 13, 132502 (2010) - [doi:10.1103/PhysRevLett.104.132502](https://doi.org/10.1103/PhysRevLett.104.132502)
- [Yam+11] T. Yamazaki et al. DISTO collaboration, *Role of the  $\Lambda(1405)$  in the Formation of the  $X = K^-pp$  Deeply Bound*

*States Revealed in the  $pp \rightarrow X + K^+$  Reaction at 2.50 GeV and 2.85 GeV* (2011) - [arXiv:1102.0482v1](#)

- [YDA04] T. Yamazaki, A. Dote, Y. Akaishi, *Invariant-mass spectroscopy for condensed single- and double- $K^-$  nuclear clusters to be formed as residues in relativistic heavy-ion collisions* Physics Letters B, Vol. 587, Issue 3-4, pp. 167-174 (2004) - [doi:10.1016/j.physletb.2004.01.089](#)

## List of Figures

1	Diagram of QCD matter . . . . .	2
2	Effective mass of K mesons . . . . .	5
3	Structure of $pK^-$ and $ppK^-$ . . . . .	9
4	Molecular structure of the $ppK^-$ . . . . .	10
5	Adiabatic potential of $ppK^-$ and schemes of nuclear force . . . . .	11
6	Reaction diagram of $ppK^-$ formation in pp collisions . . . . .	12
7	Cross sections for the formation of $ppK^-$ . . . . .	13
8	Kinematic plots for $K^+$ and $ppK^-$ . . . . .	14
9	Invariant mass of $\Lambda p$ from FINUDA . . . . .	15
10	Missing mass and invariant mass of $\Lambda p$ from DISTO . . . . .	17
11	Reconstruction of the $ppK^-$ . . . . .	19
12	Optimization of the proton beam energy . . . . .	20
13	Schematic view of the FOPI spectrometer . . . . .	22
14	QCD phase diagram . . . . .	23
15	Schematic view of SIS18 . . . . .	24
16	Cross section drawings of the CDC . . . . .	28
17	Supermodules of the MMRPC . . . . .	32
18	Cross sections of the MMRPC . . . . .	33
19	Illustrations of the PLAWA . . . . .	34
20	Illustrations of the ZDC . . . . .	35
21	Layout of the beam line . . . . .	35
22	Scheme of SiAViO . . . . .	38
23	PID via energy loss measurement . . . . .	44
24	CDC mass spectrum . . . . .	45
25	PID via TOF measurement with PLAWA . . . . .	46
26	PID via TOF measurement with MMRPC . . . . .	47
27	Shortest distance to primary vertex . . . . .	51
28	Illustration of the decay of a $\Lambda$ -Hyperon . . . . .	53
29	Secondary vertex reconstruction . . . . .	54
30	Schematic view of the $\Lambda$ -Hyperon reconstruction . . . . .	55
31	Schematic view of vertex cut quantities for $\Lambda$ reconstruction . . . . .	57
32	Distributions of the vertex cut quantities and their thresholds . . . . .	64
33	Illustration of the event mixing method . . . . .	68
34	Determination of the polynomial background function . . . . .	72
35	Invariant mass spectrum of the $\Lambda$ -Hyperon: no vertex cuts applied . . . . .	73
36	Invariant mass spectrum of the $\Lambda$ -Hyperon: vertex cut study . . . . .	79
37	Invariant mass spectrum of the $\Lambda$ -Hyperon: vertex cuts applied . . . . .	80
38	Background corrected invariant mass spectrum of the $\Lambda$ -Hyperon . . . . .	82
39	Different regions in the FOPI spectrometer . . . . .	83
40	Forward background corrected invariant $\Lambda$ mass spectrum . . . . .	86
41	PID of $K^+$ with MMRPC . . . . .	88

---

42	Missing mass spectrum of the $K^+$ meson . . . . .	89
43	Illustration of the track refitting routine . . . . .	91

## List of Tables

1	Properties of the $\Lambda(1405)$ Resonance . . . . .	7
2	Properties of the $ppK^-$ State . . . . .	9
3	Experimental Results on $ppK^-$ . . . . .	16
4	Calculated Cross Sections . . . . .	20
5	FOPI Trigger Conditions . . . . .	39
6	Particle Properties . . . . .	42
7	Properties of the $\Lambda$ -Hyperon . . . . .	52
8	Applied Vertex Cuts . . . . .	58
9	Reduction Effect of Vertex Cuts . . . . .	74
10	Physical Constants . . . . .	102
11	Text Abbreviations . . . . .	103

## A Abbreviations

### A.1 Physical Constants

$c$	$=$	$299\,792\,458$	$[\text{m/s}]$	speed of light
$\text{eV}$	$=$	$1.6022 \cdot 10^{-19}$	$[\text{J}]$	electronvolt
$N_A$	$=$	$6.022 \cdot 10^{23}$	$[\text{1/mol}]$	Avogadro constant
$k$	$=$	$1.3806 \cdot 10^{-23}$	$[\text{J/K}]$	Boltzmann constant
$r_e$	$=$	$2.818 \cdot 10^{-15}$	$[\text{m}]$	class. electron radius
$m_e$	$=$	$0.511$	$[\text{MeV}/c^2]$	electron mass
$e$	$=$	$1.6022 \cdot 10^{-19}$	$[\text{C}]$	elementary charge
$\epsilon_0$	$=$	$8.854 \cdot 10^{-12}$	$[\text{F/m}]$	vacuum permittivity

Table 10: Physical Constants

### A.2 Text Abbreviations

BPM	...	Beam Profile Monitor
BR	...	Branching Ratio
CERN	...	Conseil Européen pour la Recherche Nucléaire
CFL	...	Color-Flavour Locked
ChPT	...	CHiral Perturbation Theory
CDC	...	Central Drift Chamber
cms	...	Centre of Mass System
DAΦNE	...	Double Annular Factory for Nice Experiments
DAQ	...	Data Aquisition
ESR	...	Experimental Storage Ring
EOS	...	Equation of State
FINUDA	...	Fisica Nucleare a DAΦNE
GSI	...	Gesellschaft für SchwerIonenforschung mbH
HADES	...	High Acceptance Di-Electron Spectrometer
HV	...	High Voltage
KaoS	...	KAOn Spectrometer
KEK	...	Koo Energy Ken
KLOE	...	K LOnG Experiment
KNC	...	Kaonic Nuclear Cluster
LEAR	...	Low Energy Antiproton Ring
LH <sub>2</sub>	...	Liquid Hydrogen
LNF	...	Laboratori Nazionali di Frascati
LNS	...	Laboratoire National Saturne

MMRPC	...	Multi-gap Multi-strip Resistive Plate Chamber
PLAWA	...	PLAstic WALL
PMT	...	PhotoMultiplier Tube
QCD	...	Quantum ChromoDynamics
QED	...	Quantum ElectroDynamics
QFT	...	Quantum Field Theory
QGP	...	Quark Gluon Plasma
RPC	...	Resistive Plate Chamber
S/B	...	Signal-to-Background (ratio)
SiAViO	...	SiIcon for $\Lambda$ Vertexing and Identification Online
SIS18	...	SchwerIonenSynchrotron 18 (heavy-ion synchrotron 18)
SM	...	Super Module
TOF	...	Time Of Flight
UNILAC	...	UNIversal Linear ACCelerator
ZDC	...	Zero Degree Counter

Table 11: Abbreviations in use

## B Curriculum Vitae

### Personal Data

Katharina Isepp, BSc  
born on February 8th 1987 in Villach, Austria  
Austrian citizen

### Education

1993 - 1997	Primary School VS4 Völkendorf	Villach
1997 - 2001	Grammar School St. Martin	Villach
2001 - 2006	Secondary Technical and Vocational College (HTL) for Electronic Data Processing and Business Organization (EDVO)	Villach
2006 - 2008	Leopold Franzens University Diploma Degree Programme in Physics	Innsbruck
2008 - 2009	University of Vienna Bachelor Degree Programme in Physics	Vienna
2008 -	University of Economics and Business Administration (WU) Bachelor Degree Programme in Business Law	Vienna
2009	University of Vienna, Institute for Nuclear Physics Bachelor Thesis <i><math>\beta</math>-Radioactivity &amp; Neutrinos</i>	Vienna
2009 - 2012	University of Vienna Master Degree Programme in Physics	Vienna
2010	Austrian Academy of Sciences, Institute of High Energy Physics Summer Student at CERN, Geneva	Vienna
2011 - 2012	Austrian Academy of Sciences, Stefan Meyer Institute for Subatomic Physics Master Thesis <i>Study of Strangeness Production in pp Collisions at FOPI</i>	Vienna
2012	University of Economics and Business Administration (WU), Institute for Austrian and International Tax Law Bachelor Thesis <i>Das Prinzip der Individualbesteuerung im rechtspolitischen Vergleich mit Haushaltsbesteuerung und Familiensplitting</i>	Vienna

### Languages

German	native
--------	--------



---

English	fluent
Italian	conversant
Russian	basic knowledge

**Soft Skills**

---

programming	C, C++, C#, COBOL, FORTRAN, VB, Java
data base	SQL, JDBC, ODBC, Oracle
others	CICS, PAW, ROOT, Latex

## C Acknowledgements

First of all, I want to thank my supervisor *Johann Zmeskal*, who excited my interest in experimental particle physics and who made this master thesis possible. I highly appreciate his support, advice, patience and confidence in me, giving me the opportunity to work in an excellent research group.

In this context, I want to acknowledge *Eberhard Widmann* representative for the Stefan Meyer Institute for Subatomic Physics of the Austrian Academy of Sciences for supporting this thesis. In particular, I want to thank *Olaf Hartmann*, *Paul Bühler*, *Michael Cargnelli* and *Ken Suzuki* for their contribution to my work by granting me their assistance and advice during the last year. Moreover, many thanks to all people from SMI for offering their help whenever needed and for making me enjoy my stay at the institute.

Furthermore, I would like to give sincere thanks to the FOPI collaboration, in particular to *Robert Münzer* and the excellence cluster group in Munich and to *Norbert Hermann* for sharing the FOPI software with me and their assistance with problems in this regard. Special thanks also to *Yvonne Leifels*, who organized the paperwork at GSI for me.

My deepest thanks go to my beloved family and all of its members. Above all, I would like to express my gratitude to my wonderful parents, who supported me throughout my life, granting me so many privileges and guiding me with fondness and wisdom. I also want to thank my younger sisters *Martina* and *Alexandra*, who have accompanied me ever since, always being there for me sympathetically and patiently whenever I need them. Thank you all so much for your support and the countless magic moments and thousands of memories you have provided me with.

Last but not least, I want to acknowledge my close friends for travelling with me through life and world, for participating, teaching, asking and supporting me, for all the enriching discussions we have, the various interests you have sparked in me, the adventures we have mastered together and of course for the cheerful hours we spend. I have learned a lot from you all.